THE USE OF NANOPARTICLES IN THE DIAGNOSIS AND THERAPY OF INFECTIOUS DISEASE IN ANIMALS, 2nd Edition

EDITED BY: Gerson Nakazato, Renata Katsuko Takayama Kobayashi and Santosh Dhakal

PUBLISHED IN: Frontiers in Veterinary Science and Frontiers in Nanotechnology

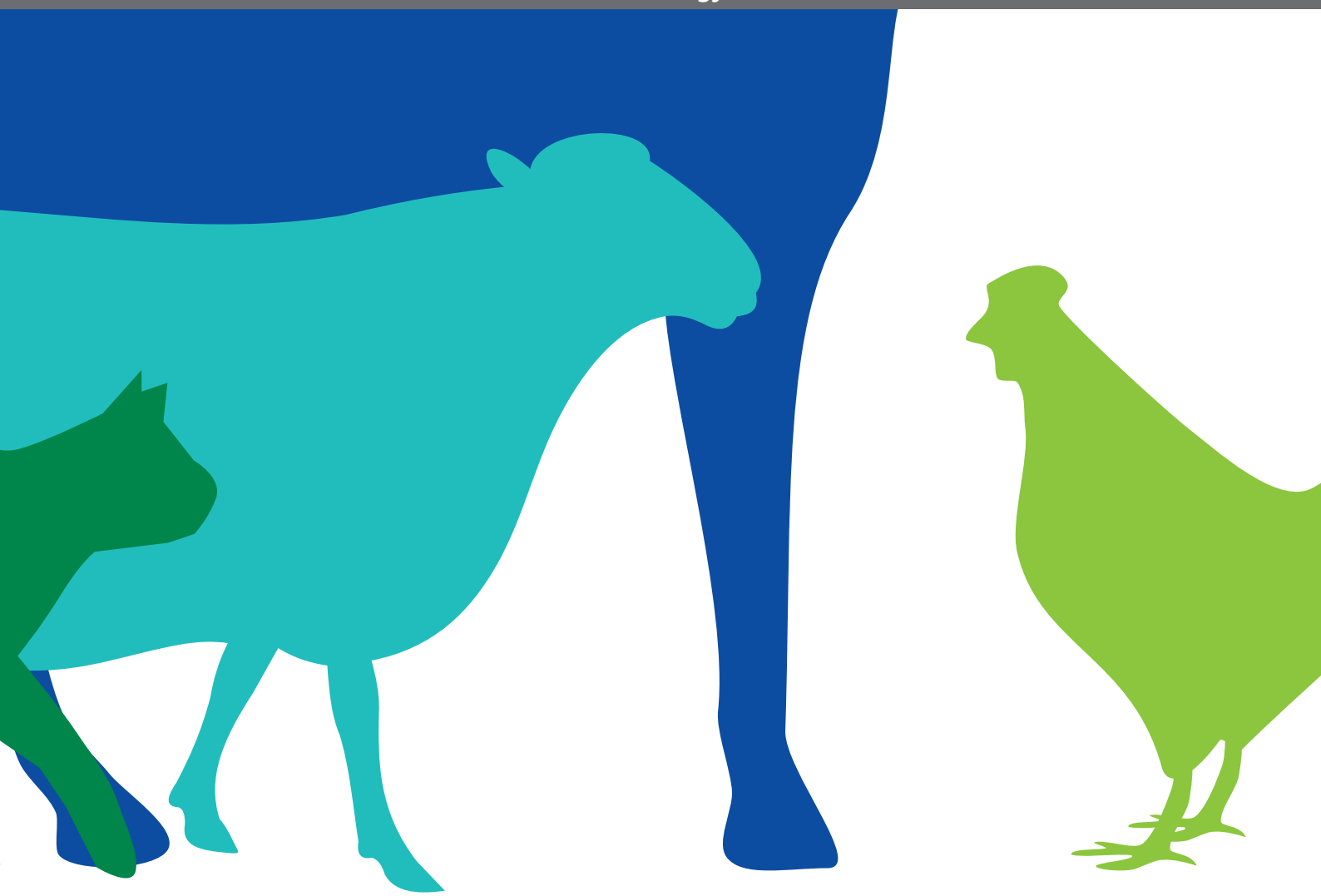

frontiers Research Topics

ISSN 1664-8714
ISBN 978-2-8325-3117-4
DOI 10.3389/978-2-8325-3117-4

About Frontiers

Frontiers is more than just an open-access publisher of scholarly articles: it is a pioneering approach to the world of academia, radically improving the way scholarly research is managed. The grand vision of Frontiers is a world where all people have an equal opportunity to seek, share and generate knowledge. Frontiers provides immediate and permanent online open access to all its publications, but this alone is not enough to realize our grand goals.

Frontiers Journal Series

The Frontiers Journal Series is a multi-tier and interdisciplinary set of open-access, online journals, promising a paradigm shift from the current review, selection and dissemination processes in academic publishing. All Frontiers journals are driven by researchers for researchers; therefore, they constitute a service to the scholarly community. At the same time, the Frontiers Journal Series operates on a revolutionary invention, the tiered publishing system, initially addressing specific communities of scholars, and gradually climbing up to broader public understanding, thus serving the interests of the lay society, too.

Dedication to Quality

Each Frontiers article is a landmark of the highest quality, thanks to genuinely collaborative interactions between authors and review editors, who include some of the world's best academicians. Research must be certified by peers before entering a stream of knowledge that may eventually reach the public - and shape society; therefore, Frontiers only applies the most rigorous and unbiased reviews.
Frontiers revolutionizes research publishing by freely delivering the most outstanding research, evaluated with no bias from both the academic and social point of view. By applying the most advanced information technologies, Frontiers is catapulting scholarly publishing into a new generation.

What are Frontiers Research Topics?

Frontiers Research Topics are very popular trademarks of the Frontiers Journals Series: they are collections of at least ten articles, all centered on a particular subject. With their unique mix of varied contributions from Original Research to Review Articles, Frontiers Research Topics unify the most influential researchers, the latest key findings and historical advances in a hot research area! Find out more on how to host your own Frontiers Research Topic or contribute to one as an author by contacting the Frontiers Editorial Office: frontiersin.org/about/contact

THE USE OF NANOPARTICLES IN THE DIAGNOSIS AND THERAPY OF INFECTIOUS DISEASE IN ANIMALS, 2nd Edition

Topic Editors:
Gerson Nakazato, State University of Londrina, Brazil
Renata Katsuko Takayama Kobayashi, State University of Londrina, Brazil
Santosh Dhakal, Johns Hopkins University, United States

All Topic Editors hold patents related to nanoparticles and declare no other competing interests with regard to the Research Topic subject.

Publisher's note: In this 2nd edition, the following article has been added: Citation: Hans R, Yadav PK, Zaman MB, Poolla R and Thavaselvam D (2023) A rapid direct-differential agglutination assay for *Brucella* detection using antibodies conjugated with functionalized gold nanoparticles. *Front. Nanotechnol*. 5:1132783. doi: 10.3389/fnano.2023.1132783

Citation: Nakazato, G., Kobayashi, R. K. T., Dhakal, S., eds. (2023). The Use of Nanoparticles in the Diagnosis and Therapy of Infectious Disease in Animals, 2nd Edition. Lausanne: Frontiers Media SA. doi: 10.3389/978-2-8325-3117-4

Table of Contents

frontiers in Veterinary Science

EDITORIAL
published: 24 December 2021
doi: 10.3389/fvets.2021.829540

Editorial: The Use of Nanoparticles in the Diagnosis and Therapy of Infectious Disease in Animals

Renata K. T. Kobayashi[1]*, *Santosh Dhakal*[2]* and *Gerson Nakazato*[1]*

[1] Department of Microbiology, Center of Biological Sciences, State University of Londrina, Londrina, Brazil, [2] W. Harry Feinstone Department of Molecular Microbiology and Immunology, The Johns Hopkins Bloomberg School of Public Health, Baltimore, MD, United States

Keywords: nanotechnology, microbial pathogens, resistance, detection, molecular methods

Editorial on the Research Topic

The Use of Nanoparticles in the Diagnosis and Therapy of Infectious Disease in Animals

The infectious diseases are extremely relevant to veterinary medicine since they are responsible for most appointments in the veterinary hospitals and clinics, extensive economic losses in animal production, along with the potential zoonotic risk of many of these etiological agents. Each disease has different sources of infection, transmission routes, entry points and possible susceptible animals, requiring efficient diagnosis and treatments.

It is also essential to reinforce the "One Health" concept, which aims at the inseparability of human, animal, and environmental health. Numerous epidemics and pandemics that originate from livestock, including the influenza virus and coronaviruses, highlight the importance of early diagnosis, continuous monitoring, and efficient prevention of the emerging or re-emerging animal infectious pathogens to minimize their significant impacts on the animal health, food safety and food security, and public health (1).

Nanotechnology has revolutionized the field of infectious disease diagnosis, and the development of therapeutics and preventatives. Their significance in biomedical application is due to their smaller size and unique physicochemical properties which allows for the controlled release of the drugs, targeted drug delivery, and *in vivo* immunomodulation. Nanotechnology has been used in various aspects of veterinary medicine including disease diagnosis, treatment, development of adjuvants and vaccines, drug delivery, and solving problems related to animal nutrition and reproduction (2). Nanotechnology provides more efficient diagnostic tools and therapies, whether in terms of sensitivity, specificity, speed, or cost. Various nanomaterials have been used in veterinary diagnostics and therapeutics including metal nanoparticles, polymeric nanoparticles, nanoemulsions, liposomes, and nanocrystals (2). The use of nanotechnology in veterinary medicine will continue in the future leading to advancements in the diagnosis and therapies of infectious diseases in animals safeguarding both animal and human health.

The aim of this Research Topic was to bring together the use of nanotechnology in the detection of veterinary infectious pathogens (bacteria, viruses, protozoa, and fungi) and in animal infectious disease management (therapies and vaccinations). This Research Topic includes four articles in which three describe diagnostic approaches and one highlights application of nanoparticles as antimicrobial agent for the veterinary diseases. These studies showed the advances of nanotechnology in the veterinary field, mainly for the diagnosis of emerging diseases. There is a large potential of these nanoparticles in the development of new products and processes to detect, prevent and eliminate pathogens from animal sources. In a review, Manhas et al. highlighted latest updates on the nanomaterials-based diagnostic tests to six emerging/re-emerging

OPEN ACCESS

Edited and reviewed by:
Michael Kogut, Agricultural Research Service, United States Department of Agriculture (USDA), United States

***Correspondence:**
Renata K. T. Kobayashi
kobayashirkt@uel.br
Santosh Dhakal
sdhakal3@jhmi.edu
Gerson Nakazato
gnakazato@uel.br

Specialty section:
This article was submitted to Veterinary Infectious Diseases, a section of the journal Frontiers in Veterinary Science

Received: *05 December 2021*
Accepted: *09 December 2021*
Published: *24 December 2021*

Citation:
Kobayashi RKT, Dhakal S and Nakazato G (2021) Editorial: The Use of Nanoparticles in the Diagnosis and Therapy of Infectious Disease in Animals. Front. Vet. Sci. 8:829540. doi: 10.3389/fvets.2021.829540

poultry and livestock diseases namely avian influenza (colloidal particle-conjugated antibodies), post-weaning multisystemic wasting syndrome (antibody-modified gold-platinum and silica dioxide nanospheres), Newcastle disease (iron oxide nanoparticles–magnetic separation), anthrax (biosensor with single-stranded modified-AuNPs probes), brucellosis (oligonucleotide-modified AuNP-based colorimetric assay) and aflatoxicosis (aptasensor with Au nanowires/graphene oxide). They reported that immuno-based and molecular-based functionalization and alterations of various nanomaterials have improved the speed of pathogens and toxins detections with superior sensitivity and specificity. Ge et al. developed blue silica nanoparticles (SiNPs)-based lateral flow immunoassay (LFIA) for rapid detection of human brucellosis with high sensitivity and specificity. For this, *Staphylococcal* protein A (SPA) and lipopolysaccharide of *Brucella* spp. were used in design of SiNPs-based LFIA that could detect antibody target on serum samples. Using brucellosis positive and negative human serum samples, Ge et al. showed 87% and 93.9% positive and negative predictive values to this assay which can be used for on-site diagnosis of the pathogen.

A molecular strategy to express the capsid protein (Cap) of Porcine Circovirus Type 4 (PCV4) based on *Escherichia coli* expression system was approached in the study of Wang et al. The PCV4 virus-like particles (VLPs) were of size ∼20 nm and had high antigenicity. As these nanostructures have unique morphology and immunogenicity they can be used for serological diagnostics and for vaccine development in the future.

Water disinfection is very important for public health and several diseases may come from water sources. Zhang et al. showed that copper/carbon core/shell nanoparticles (CCCSNs) and a commercial CCCSNs filter product were efficient against *Saprolegnia parasitica* which is one of the most prevalent oomycete diseases in aquaculture and important pathogen of finfish. Interestingly, these nanoparticles serve as an alternative for formalin in water treatment, corroborating for prevention and control of *S. parasitica*.

Studies included in this Research Topic demonstrated that nanotechnology needs more exploration in the field of veterinary medicine, mainly in production animals, because the results of these four articles showed a great potential to generate new products using nanoparticles for the diagnosis, treatment and prevention of veterinary infectious diseases. It is noteworthy that early detection or prevention of animal diseases not only protects animal health and ensure animal welfare but also provides food security and protects human health. Thus, nanotechnology should be explored fully for the development of diagnostic tools, therapeutics, and vaccines to protect animal health and hence the public health.

AUTHOR CONTRIBUTIONS

All authors listed have made a substantial, direct, and intellectual contribution to the work and approved it for publication.

FUNDING

This work was supported in part by the National Council for Scientific and Technological Development (CNPq)–processes 433656/2018-2 Call MCTIC/CNPq 28/2018 and 313305/2019-6 to RK and CNPq–process 315435/2018-6 to GN.

ACKNOWLEDGMENTS

We would like to thank the Marcelly C. Gonçalves for the English language edition. The editorial guidance and the suggestions of Editorial Team of Frontiers in Veterinary Science for handling this Research Topic were highly appreciated.

REFERENCES

1. Mcelwain TF, Thumbi SM. Animal pathogens and their impact on animal health, the economy, food security, food safety and public health. *Rev Sci Tech.* (2017) 36:423–33. doi: 10.20506/rst.36.2.2663
2. Youssef FS, El-Banna HA, Elzorba HY, Galal HM. Application of some nanoparticles in the field of veterinary medicine. *Int J Vet Sci Med.* (2019) 7:78–93. doi: 10.1080/23144599.2019.1691379

Conflict of Interest: The authors declare that the research was conducted in the absence of any commercial or financial relationships that could be construed as a potential conflict of interest.

frontiers in Veterinary Science

MINI REVIEW
published: 07 June 2021
doi: 10.3389/fvets.2021.673718

Enhanced Detection of Major Pathogens and Toxins in Poultry and Livestock With Zoonotic Risks Using Nanomaterials-Based Diagnostics

*Priya K. Manhas, Irwin A. Quintela and Vivian C. H. Wu**

Produce Safety and Microbiology Research Unit, U.S. Department of Agriculture, Agricultural Research Service, Western Regional Research Center, Albany, CA, United States

Nanotechnology has gained prominence over the recent years in multiple research and application fields, including infectious diseases in healthcare, agriculture, and veterinary science. It remains an attractive and viable option for preventing, diagnosing, and treating diseases in animals and humans. The apparent efficiency of nanomaterials is due to their unique physicochemical properties and biocompatibility. With the persistence of pathogens and toxins in the poultry and livestock industries, rapid diagnostic tools are of utmost importance. Though there are many promising nanomaterials-based diagnostic tests specific to animal disease-causing agents, many have not achieved balanced sensitivity, specificity, reproducibility, and cost-effectiveness. This mini-review explores several types of nanomaterials, which provided enhancement on the sensitivity and specificity of recently reported diagnostic tools related to animal diseases. Recommendations are also provided to facilitate more targeted animal populations into the development of future diagnostic tools specifically for emerging and re-emerging animal diseases posing zoonotic risks.

Keywords: nanomaterials, gold nanoparticles, diagnostic tools, animal diseases, zoonotic pathogens

OPEN ACCESS

Edited by:
Gerson Nakazato, State University of Londrina, Brazil

Reviewed by:
Santosh Dhakal, Johns Hopkins University, United States
Vivek A. Kuttappan, Novus International, Brazil

****Correspondence:***
Vivian C. H. Wu
vivian.wu@usda.gov

Specialty section:
This article was submitted to Veterinary Infectious Diseases, a section of the journal Frontiers in Veterinary Science

Received: *28 February 2021*
Accepted: *11 May 2021*
Published: *07 June 2021*

Citation:
Manhas PK, Quintela IA and Wu VCH (2021) Enhanced Detection of Major Pathogens and Toxins in Poultry and Livestock With Zoonotic Risks Using Nanomaterials-Based Diagnostics. Front. Vet. Sci. 8:673718. doi: 10.3389/fvets.2021.673718

INTRODUCTION

As the world's population steadily increases, sustainable and safe agriculture remains very critical. Global trade, climate change, and modified farm practices create new opportunities for the transmission of transboundary animal diseases (1). This dynamic has resulted in foreign and endemic infectious disease outbreaks, which negatively impacted agriculture, the economy, and public health (2).

The combined production value of poultry and livestock industries in the United States amounts to almost $ 91 billion (3), but poultry and livestock disease outbreaks pose a significant challenge. A vital example of a common but fatal poultry disease is avian influenza. Highly pathogenic avian influenza (HPAI) A (H5N1) causes high fatality rates in poultry; first detected in 1996 (China) from geese, and then in humans in 1997 (Hong Kong) during a poultry outbreak. Since then, it has been under surveillance in 50 countries across four continents and remained endemic in six countries. Around 50 million birds (chickens and turkeys), which accounted for 8% of turkey meat and 12% of table-egg laying chickens in the U.S., died and/or were destroyed between 2014 and 2015 to control the spread of HPAI (4). In November 2020, 19,000 birds suspected of H5N8 infection were culled in

Korea (5). From 2003 to 2020, 862 cases of human infection with H5N1 were reported globally, with 455 deaths (6). The emergence of Severe Acute Respiratory Syndrome Coronavirus 2 (SARS-CoV-2), which causes COVID-19, has infected 114 million people globally, with 2.5 million deaths as of February 2021 (7). SARS-CoV-2 and other highly genetically diversified bat-associated coronavirus strains can infect varying mammalian hosts, including bats, carnivores, pangolins, and primates (8). It is important to efficiently monitor and control these emerging and re-emerging pathogens to prevent the occurrence of outbreaks between humans and animals, that is, livestock populations.

Nanomaterials have gained prominence in diagnostics due to their combined strength and ductile properties (9). Nanoparticles such as gold nanoparticles (AuNPs) exhibit unique properties and functions on the nanodimensional scale (10, 11) and are readily visualized due to intense colors and formation of stable conjugates for highly-sensitive and specific diagnostic applications (12). This minireview aims to provide a comprehensive assessment by discussing the six emerging/re-emerging and prevalent diseases affecting poultry and livestock while focusing on both the functionalization and modifications of the integrated nanomaterials in the published diagnostic methods, balancing an optimum sensitivity and sensitivity.

FUNCTIONALIZATION OF NANOMATERIALS

The inert nature of nanomaterials limits their applications; hence, it requires functionalization to allow integration into the diagnostic platforms (13). Surface functionalization and encapsulation may include small molecule ligands, polymers, and biomolecules (14). The bottom-up approach wherein nanomaterials are synthesized prior to their intended use along with their organic binders has remained popular (15). Functionalization of nanomaterials can be achieved in various approaches; however, this mini-review focuses only on those intended for immuno-based methods and molecular-based diagnostics.

IMMUNO-BASED METHODS

Immuno-based methods utilizing nanoparticles take advantage of the antibody-antigen relationships. These diagnostic methods use antibodies as either capture/detection elements or the assay's primary targets. Antibodies conjugated into nanoparticles have proven to be excellent biorecognition elements due to stability, biocompatibility, and its sensitivity to the target antigens even at lower concentrations (16). As targets, the presence of certain antibodies in animal sera, blood, and urine can also be strong indicators of pathogen exposure and infection (17). Nanomaterials are functionalized with antigens to target these antibodies at various stages of infections (18–20). The following emerging and re-emerging veterinary infectious diseases are often diagnosed by utilizing nanomaterials in either antigen-detecting or antibody-detecting diagnostic assays.

Avian Influenza

Avian influenza continuously assails both avian species and humans and has become a threat to health and the economy (21). Diagnostic kits for avian influenza are usually based on immunochromatography that utilizes antiviral nucleoprotein antibodies and colloidal particle-conjugated antibodies (22).

A fluorescent immunochromatographic test strip incorporated with monoclonal antibody (MAb)-modified europium nanoparticles specific to hemagglutinin with a detection limit of 31 ng/ml was previously reported (23). Recently, a colloidal Au-based immunochromatographic strip test with two MAbs for H7N9 avian influenza viral antigen detection with a detection limit of $10^{2.55}$ 50% tissue culture infective dose which is equivalent to two hemagglutinin units of H7N9 (1:32 dilution) has been reported (24). Compared with PCR, this immunochromatographic strip test has a 71.4% sensitivity and 98.6% specificity (24). Similarly, an antibody-based method utilizing magnetic silica nanoparticles with a resonance light scattering system had a sensitivity range of 0.5–50 ng/ml with no cross-reactivity reaction reported (25). And finally, an immune-based electrochemical method utilizing silver nanoparticles (AgNPs) specific to H7N9, chitosan, and graphene on a gold electrode coated with AuNPs/graphene had a sensitivity of 1.6 pg/ml within 1 h while remaining highly-selective against other avian influenza strains (**Figure 1A**) (26). The current USDA National Veterinary Services Laboratories (NVSL) standard operating procedures for detecting avian influenza from oropharyngeal/cloacal, and fecal swab samples primarily involve real-time reverse transcriptase PCR (RT-PCR). With the integration of nanomaterials into portable diagnostic methods, pen-side testing has become a viable option without comprising sensitivity and specificity.

Postweaning Multisystemic Wasting Syndrome

Postweaning multisystemic wasting syndrome (PMWS) is a viral infection caused by porcine circovirus type 2 (PCV2), causing wasting and pale skin, respiratory distress, and icterus in the nursery and growing pigs accompanied by a high mortality rate (30). There is no known cure for PMWS, and infected pigs have an increased rate of mortality (31). Though it is not considered as a zoonotic disease yet, PCV2 can potentially proliferate in human cells *in vitro* (32). Licensed PCV2 vaccines (Suvaxyn PC2 and Ingelvac CircoFLEX) that effectively prevent PCV2 viremia are currently available in the U.S.

Monoclonal antibodies (MAbs)-conjugated nanomaterials for PCV2 detection have been previously reported. A PCV2-specific MAb-AuNPs in a chemiluminescence immunoassay has resulted in a limit of detection (LOD) of 1.73×10^3 copies/ml, which was further enhanced to 2.67×10^2 copies/ml by hydroxylamine amplified AuNPs (III) (**Figure 1B**) (27). This assay, however, had a moderate incidence rate of cross-reactivity around 18.8% (27). A similar LOD (8×10^2 copies/ml) was achieved when MAb-modified multi-branched AuNPs were used against PCV2 cap protein in surface-enhanced Raman scattering (SERS) (33). Conventional ELISA has also been modified with nanomaterials

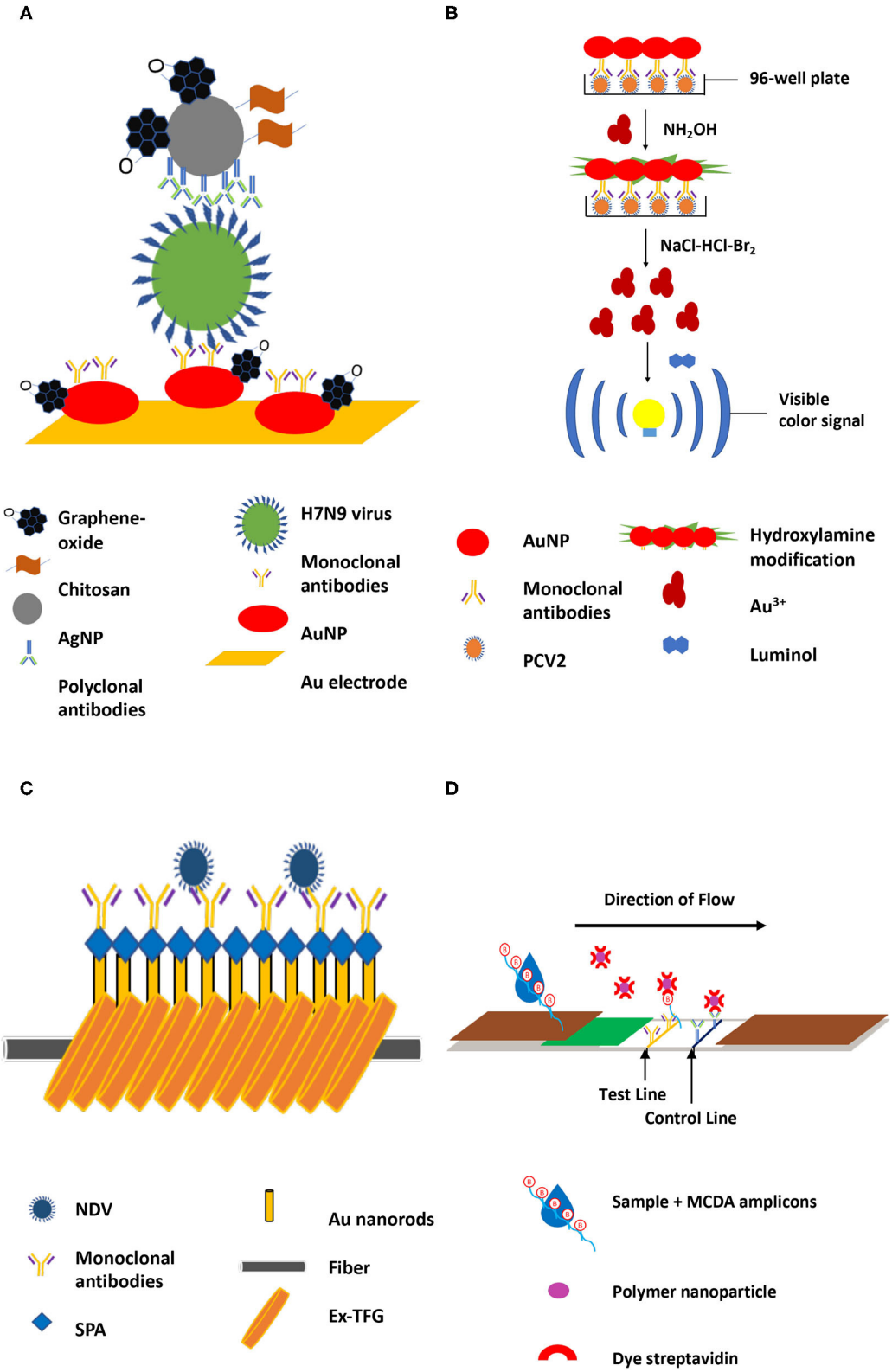

FIGURE 1 | Representative animal disease diagnostic methods incorporated with various nanomaterials. **(A).** Silver nanoparticles in immune-based electrochemical method targeting H7N9 virus (26). **(B).** Chemiluminescence immunoassay with AuNPs targeting PCV2 (27) **(C).** Detection of Newcastle disease through targeting ND antibodies using excessively tilted fiber grating (Ex-TFG) coated with gold nanospheres (28). **(D).** Polymer nanoparticle-based LFB for detecting brucellosis (29).

in an attempt to improve its sensitivity without increasing its cost (17, 34, 35). The horseradish peroxidase component of an enzyme-free "ELISA" has been replaced with antibody-modified gold-platinum and silica dioxide nanospheres (35). The nanospheres complex allowed a colorimetric change from red to purple with the presence of PCV2 without cross-reactivity, which resulted in a 200-fold improvement in sensitivity compared as compared to the traditional ELISA. The gold standard for the diagnosis of the disease is RT-PCR, while virus isolation, electron microscopy, and serum virus neutralization assays are also utilized; field testing is currently available. The development of nanomaterials-based assays has allowed rapid detection of PCV2 without the need for complicated and costly equipment.

Newcastle Disease

Newcastle disease (ND) is a viral disease causing respiratory distress, lesions, cessation of egg productions, and nervous manifestations in poultry and wild avian species (36–39). Newcastle disease (ND) has been prevalent in Asia, Africa, North, and South America; the onset of infection can affect a flock within an average of 5 days post aerosol exposure. Unfortunately, ND virulent virus carries a zoonotic risk of transitory conjunctivitis to laboratory workers and other staff, that is, vaccination teams; thus, safety guidelines and protocols need to be strictly implemented and followed (40). Diagnosis often relies on viral isolation and subsequent conventional characterization, which can take 2–12 days post-exposure (41).

Similar to avian influenza, ND can also be detected and diagnosed by using immunochromatographic assays. Recently, a quantitative antigen-based Au-immunochromatographic technique incorporated with viral protein antigens/AuNPs (haemagglutinin-neuraminidase) was developed, which allowed the detection of ND viral antibodies with a sensitivity of 2^2 titers without any cross-reactivity (42).

Fluoroimmunoassays have been also reported for ND virus detection. This method primarily relies on fluorescent signals but often lacks sensitivity. However, when magnetic separation is added as a concentration step of target analytes, sensitivity can drastically improve. Cadmium telluride quantum dots modified with NDV antibodies and mercaptosuccinic acid coupled with iron oxide nanoparticles were able to detect as low as 1.5 ng/ml of antigens without compromising specificity (43). Furthermore, an immunosensor with tilted fiber grating (Ex-TFG) coated with staphylococcal protein A-Au nanospheres was able to successfully detect NDV antibodies within 25 min (28). This method had a detection limit of 25 pg/ml, a 100-fold more sensitive than the previously reported fluoroimmunoassay (**Figure 1C**) (28). Furthermore, the addition of Au nanospheres has allowed a 5–10 times improvement in sensitivity compared to the Ex-TFG alone (28). Commercial ND viral diagnostic tests (i.e., IDEXX Newcastle Disease Virus Antibody Tests) are currently available such as ELISA systems that allow detection and quantification of antibodies to ND viruses. Nanomaterials will continuously improve the diagnosis and rapid testing technologies of ND viruses for effective monitoring and mitigation steps.

MOLECULAR-BASED METHODS

Nanomaterials have been modified with synthetic nucleic acid probes (i.e., aptamers and oligonucleotides) to serve as recognition elements. Molecular-based recognition elements offer significant advantages over antibodies. Antibodies have low stability at high temperatures, high production costs and variation with each subsequent batch, and a need for a constant supply of mammalian cell culture (44). In contrast, aptamers are non-immunogenic and are highly stable at various conditions maintaining their high binding affinity with the target analytes (45). The use of aptamers significantly lowers manufacturing costs compared to antibody-based techniques, as aptamers do not require complicated procedures and infrastructures such as animal care facilities (45). The following emerging veterinary infectious diseases can be detected by utilizing molecular-based diagnostic methods enhanced with nanomaterials.

Anthrax

Anthrax is a serious infectious bacterial disease caused by *Bacillus anthracis*, which is fatal to ruminants and humans alike, and often spreads quickly through contaminated feed and water (46). In a study that examined the prevalence of *B. anthracis* spores, 30% of sheep and 27.5% of goats were positive for the presence of spores that were attached to the body of animals (47). These spores can cause a zoonotic infection in humans with a 25–60% fatality rate (48).

There are many molecular-based diagnostic techniques used to detect *B. anthracis*. One such technique used a quartz crystal microbalance (QCM) biosensor with single-stranded modified-AuNPs probes specific to *Ba813* and *pag* of *B. anthracis* and had a sensitivity of 3.5×10^2 CFU/ml (49). In another study, a colorimetric assay that utilized asymmetric PCR amplicons/AuNPs complexes was able to detect *B. anthracis* at 10 pg/ml detection limit with no cross-reactivity (50). Likewise, a multi-walled carbon nanotube (MWCNTs)-based fluorescence aptasensor was reported to detect the recombinant protective antigen domain 4 (rPAD4) of *B. anthracis* within 10 min (51). The immobilized aptamer was labeled with Gel Green, and a sensitivity of 20 ng/ml and 62.5 ng/ml purified and unpurified rPAD4 protein, respectively, was reported (51). When coupled together, nanomaterials and aptamers can reduce cost as well as the turn-around time while increasing the sensitivity of the assay (50, 51). Current diagnostic tests include bacterial culture, PCR as well as ELISA for antibody detection in reference laboratories. Rapid detection using nanomaterials-based technologies will enhance the diagnosis of anthrax and assist the livestock industry in controlling the risks that it poses to animal health and the human population.

Brucellosis

Brucellosis is a bacterial infectious disease caused by *Brucella* spp., which is endemic to ruminants causing influenza-like symptoms in both cattle and humans. It can spread quickly through cattle and humans by contaminated milk and contact with animal feces (52). *Brucella* spp. are identified by direct culture from infected tissues in selective media or direct stained

smears. For serological assays, serum tube agglutination test (SAT) and milk ring test (anti-brucella antibodies) are performed.

Molecular-based methods tend to leverage the specific hybridization events between nanomaterials-based probes and target pathogens or their nucleic acids. An oligonucleotide-modified AuNP-based colorimetric assay was able to detect *Brucella* spp within 30 min by targeting the BCSP31 outer membrane protein and achieved a LOD of 10^3 CFU/ml in bovine (urine and semen samples) and 10^4 CFU/mL in milk with no cross-reactivity (53). Another target gene region, *IS711*, was detected using the same method with improved sensitivity of 1.09 pg/μl using unamplified *Brucella* genomic DNA (54, 55) without cross-reactivity observed. A multiple cross displacement amplification and lateral flow assay utilizing polymer nanoparticles modified with oligonucleotide probe targeting the *BSCP31* gene was able to improve the sensitivity to 10 fg (**Figure 1D**) (29).

Aflatoxicosis

Aflatoxicosis is a blanket term used to describe a wide variety of symptoms indicative of poisoning caused by the metabolism of aflatoxins which are potent mycotoxins that can be present in animal feeds, grains, nuts, and animal products (56). Produced from the *Aspergillus* spp., aflatoxins come in a variety of metabolites, including aflatoxin B_1, B_2, G_1, and G_2 (57). Aflatoxin B_1 (AFB_1) is considered the most toxic metabolite since it is a potent carcinogen with hepatotoxic consequences in poultry, livestock, and human consumers of infected animal products (58). Many countries have strict limits of acceptable amounts of AFB_1 in food. Specifically, the European Union sets 2 μg/kg of AFB_1 in food while in the U.S., the maximum permitted level of AFB_1 combined with B_2, G_1, and G_2 is 20 μg/kg; 0.5 μg/kg in milk; and 100–300 μg/kg range for animal feeds (59, 60). Current detection and surveillance methods include thin-layer chromatography, high-performance liquid chromatography (HPLC), mass spectroscopy, and ELISA, among others. Nanomaterials are continuously introduced and integrated into various detection applications to improve sensitivity and reduce cost, as it is very crucial to maintain the level of aflatoxins within the allowed limits.

An aptasensor with Au nanowires/graphene oxide and aptamer was developed for AFB_1 detection based on the differences in differential pulse voltammetry peak current (58). The method achieved a sensitivity of 1.4 pM or 0.62 ng/ml which was comparable to the gold standard of high-performance liquid chromatography (HPLC) and a shorter turn-around time of 90 min. Another study developed a molecular-based method utilizing mesoporous silica nanoparticles modified with a complex of amino groups, aptamers, and Rh6G through SERS and has an improved LOD of 0.13 ng/ml (60), which was more sensitive than other fluorescence methods.

FUTURE RECOMMENDATIONS

Nanomaterials have greatly improved the capabilities of numerous diagnostic tools, especially those designed to detect animal disease-causing pathogens and toxins. Many diagnostic tools can be operated on-site for pen-side testing or in the laboratory for initial screening of samples or rapid confirmation of some emerging and re-emerging animal diseases posing zoonotic risks. Though most diagnostic tools have improved their sensitivity in the past decade, some recognition materials are still suffering from cross-reactivity and production costs. The current immune-based diagnostic assays often fall short in sensitivity, specificity, and cost, but newer technologies, such as aptamers and other molecular biology tools can offer solutions. Nanomaterials can be functionalized in several different ways; however, this mini review only covers immune-based and molecular-based methods. This mini-review opens the door to a comprehensive risk and cost analysis when designing nanomaterials-based diagnostic tools for other novel pathogens.

CONCLUSION

This minireview discusses the emerging and prevalent diseases affecting poultry and livestock and puts emphasis on both the functionalization and modifications of the integrated nanomaterials in the published diagnostic methods to provide researchers and the livestock industry with alternative solutions and approaches in the diagnosis of veterinary infectious diseases. Nanomaterials including AuNPs, AgNPs, silica nanoparticles, iron oxide nanoparticles, europium nanoparticles, cadmium telluride quantum dots, and polymer nanoparticles have become valuable in the detection of pathogens and toxins causing diseases in poultry and livestock due to their versatility and biocompatibility. Functionalization and modifications of the integrated nanomaterials in the published and reported diagnostic methods have allowed rapid detection of pathogens and toxins with superior sensitivity and specificity. However, the chosen recognition elements significantly contribute to achieving the ultimate range of detection limits; therefore, it is important to consider the advantages and disadvantages of each capture and detection element in the diagnostic systems.

AUTHOR CONTRIBUTIONS

PM and IQ conducted the literature review and wrote the manuscript. IQ and VW revised the manuscript, added important scientific content, and refined the interpretation of the results. VW was involved in conceptualization, funding acquisition, review and editing of the manuscript, supervision, and project administration. All the authors reviewed the final version of the manuscript and agreed to its submission.

FUNDING

This work was supported by the United States Department of Agriculture NIFA AFRI grant (award number 2015-69003-32075) and the USDA-ARS CRIS projects 2030-32000-010-00D.

REFERENCES

1. Beltran-Alcrudo D, Falco JR, Raizman E, Dietze K. Transboundary spread of pig diseases: the role of international trade and travel. *BMC Vet Res.* (2019) 15:64. doi: 10.1186/s12917-019-1800-5
2. Massó Sagüés E, Fernández Carrión E, Sánchez-Vizcaíno JM. Risk for Europe based on the health situation of North Africa and the Arabian Peninsula. *Front Vet Sci.* (2019) 6:293. doi: 10.3389/fvets.2019.00293
3. USDA-NASS. (2017). *Overview of Livestock US, Poultry, and Aquaculture Production in 2017*. USDA. Available online at: https://www.aphis.usda.gov/animal_health/nahms/downloads/Demographics2017.pdf (accessed May 8, 2020).
4. Ramos S, MacLachlan M, Melton A. *Impacts of the 2014–2015 Highly Pathogenic Avian Influenza Outbreak on the Poultry, U. S Sector*. Washington, DC: Economic Research Service (2017).
5. OIE. Highly pathogenic avian influenza, Korea (Rep. of). 2020. Available online at:https://www.oie.int/wahis_2/public/wahid.php/Reviewreport/Review?page_refer=MapFullEventReportandreportid=36807 (accessed 20, February 2021).
6. WHO. *Avian Influenza Weekly Update Number 770*. (2020). Available online at: https://www.who.int/docs/default-source/wpro---documents/emergency/surveillance/avian-influenza/ai-20201204.pdf?sfvrsn=223ca73f_75 (accessed February 25, 2021).
7. Dong E, Du H, Gardner L. An interactive web-based dashboard to track COVID-19 in real time. *Lancet Infec Dis.* (2020) 20:533–4. doi: 10.1016/S1473-3099(20)30120-1
8. Jo WK, De Oliveira-Filho EF, Rasche A, Greenwood AD, Osterrieder K, Drexler JF. Potential zoonotic sources of SARS-CoV-2 infections. *Transbound Emerg Dis.* (2020) 00:1–11. doi: 10.1111/tbed.13872
9. Valiev R. Nanomaterial advantage. *Nature.* (2002) 419:887–9. doi: 10.1038/419887a
10. Sau TK, Pal A, Jana N, Wang Z, Pal T. Size controlled synthesis of gold nanoparticles using photochemically prepared seed particles. *J Nanopart Res.* (2001) 3:257–61. doi: 10.1023/A:1017567225071
11. Agasti SS, Rana S, Park M-H, Kim CK, You C-C, Rotello VM. Nanoparticles for detection and diagnosis. *Adv Drug Deliv Rev.* (2010) 62:316–28. doi: 10.1016/j.addr.2009.11.004
12. Draz MS, Shafiee H. Applications of gold nanoparticles in virus detection. *Theranostics.* (2018) 8:1985–2017. doi: 10.7150/thno.23856
13. Makvandi P, Iftekhar S, Pizzetti F, Zarepour A, Zare EN, Ashrafizadeh M, et al. Functionalization of polymers and nanomaterials for water treatment, food packaging, textile and biomedical applications: A review. *Environ Chem Lett.* (2020) 19:1–29. doi: 10.1007/s10311-020-01089-4
14. Mout R, Moyano DF, Rana S, Rotello VM. Surface functionalization of nanoparticles for nanomedicine. *Chem Soc Rev.* (2012) 41:2539–44. doi: 10.1039/c2cs15294k
15. Jung H, Park J, Yoo ES, Han G-S, Jung HS, Ko MJ, et al. Functionalization of nanomaterials by non-thermal large area atmospheric pressure plasmas: application to flexible dye-sensitized solar cells. *Nanoscale.* (2013) 5:7825–30. doi: 10.1039/c3nr01889j
16. Vrublevskaya VV, Afanasyev VN, Grinevich AA, Skarga YY, Gladyshev PP, Ibragimova SA, et al. A sensitive and specific lateral flow assay for rapid detection of antibodies against glycoprotein B of Aujeszky's disease virus. *J Vir Methods.* (2017) 249:175–80. doi: 10.1016/j.jviromet.2017.09.012
17. Wu L, Yin W, Tang K, Shao K, Li Q, Wang P, et al. Highly sensitive enzyme-free immunosorbent assay for porcine circovirus type 2 antibody using Au-Pt/SiO2 nanocomposites as labels. *Biosens Bioelectron.* (2016) 82:177–84. doi: 10.1016/j.bios.2016.04.001
18. Li H, Ding XH, Peng ZH, Deng L, Wang D, Chen H, et al. Aptamer selection for the detection of Escherichia coli K88. *Can J Microbiol.* (2011) 57:453–9. doi: 10.1139/w11-030
19. Wu S, Duan N, Zhu C, Ma X, Wang M, Wang Z. Magnetic nanobead-based immunoassay for the simultaneous detection of aflatoxin B1 and ochratoxin A using upconversion nanoparticles as multicolor labels. *Biosens Bioelectron.* (2011) 30:35–42. doi: 10.1016/j.bios.2011.08.023
20. Sayed RH, Abousenna MS, Mohamoud D, Saad MA. Development of a lateral flow kit for detection of IgG and IgM antibodies against rift valley fever virus in sheep. *Indian J Vet Sci Biotech.* (2019) 15:63–8. doi: 10.21887/ijvsbt.15.2.17
21. Allen T, Murray KA, Zambrana-Torrelio C, Morse SS, Rondinini C, Di Marco M, et al. Global hotspots and correlates of emerging zoonotic diseases. *Nat Commun.* (2017) 8:1–10. doi: 10.1038/s41467-017-00923-8
22. Matsubara T, Michiko U, Takashi Y, Yasuaki E, Tomo D, Takaaki N, et al. Avian influenza virus detection by optimized peptide termination on a boron-doped diamond electrode. *ACS Sens.* (2020) 5:431–9. doi: 10.1021/acssensors.9b02126
23. Yeo S-J, Bao DT, Seo G-E, Bui CT, Anh NTV, Tien TTT, et al. Improvement of a rapid diagnostic application of monoclonal antibodies against avian influenza H7 subtype virus using Europium nanoparticles. *Sci Rep.* (2017) 7:1–11. doi: 10.1038/s41598-017-08328-9
24. Yang F, Xiao Y, Chen B, Wang L, Liu F, Yao H, et al. Development of a colloidal gold-based immunochromatographic strip test using two monoclonal antibodies to detect H7N9 avian influenza virus. *Virus Genes.* (2020) 56:1–5. doi: 10.1007/s11262-020-01742-8
25. Zou X, Huang H, Gao Y, Su X. Detection of avian influenza virus based on magnetic silica nanoparticles resonance light scattering system. *Analyst.* (2012) 137:648–53. doi: 10.1039/C1AN16041A
26. Huang J, Xie Z, Xie Z, Luo S, Xie L, Huang L, et al. Silver nanoparticles coated graphene electrochemical sensor for the ultrasensitive analysis of avian influenza virus H7. *Anal Chim Acta.* (2016) 913:121–7. doi: 10.1016/j.aca.2016.01.050
27. Zhang H, Li W, Sheng Z, Han H, He Q. Ultrasensitive detection of porcine circovirus type 2 using gold (III) enhanced chemiluminescence immunoassay. *Analyst.* (2010) 135:1680–5. doi: 10.1039/c0an00025f
28. Luo B, Xu Y, Wu S, Zhao M, Jiang P, Shi S, et al. A novel immunosensor based on excessively tilted fiber grating coated with gold nanospheres improves the detection limit of Newcastle disease virus. *Biosens Bioelectron.* (2018) 100:169–75. doi: 10.1016/j.bios.2017.08.064
29. Li S, Liu Y, Wang Y, Wang M, Liu C, Wang Y. Rapid detection of *Brucella* spp. and elimination of carryover using multiple cross displacement amplification coupled with nanoparticles-based lateral flow biosensor. *Front Cell Infect Mi.* (2019) 9:78. doi: 10.3389/fcimb.2019.00078
30. Segales J, Domingo M. Postweaning mulstisystemic wasting syndrome (PMWS) in pigs. A review. *Vet Quart.* (2002) 24:109–24. doi: 10.1080/01652176.2002.9695132
31. Baekbo P, Kristensen CS, Larsen LE. Porcine circovirus diseases: a review of PMWS. *Transbound Emerg Dis.* (2012) 59:60–7. doi: 10.1111/j.1865-1682.2011.01288.x
32. Liu X, Ouyang T, Ouyang H, Liu X, Niu G, Huo W, et al. Human cells are permissive for the productive infection of porcine circovirus type 2 in vitro. *Sci. Rep.* (2019) 9:1–8. doi: 10.1038/s41598-019-42210-0
33. Luo Z, Li W, Lu D, Chen K, He Q, Han H, et al. A SERS-based immunoassay for porcine circovirus type 2 using multi-branched gold nanoparticles. *Microchim Acta.* (2013) 180:1501–7. doi: 10.1007/s00604-013-1032-5
34. Wu W, Zhao S, Mao Y, Fang Z, Lu X, Zeng L. A sensitive lateral flow biosensor for Escherichia coli O157:H7 detection based on aptamer mediated strand displacement amplification. *Anal Chim Acta.* (2015) 861:62–8. doi: 10.1016/j.aca.2014.12.041
35. Wu L, Zhang M, Zhu L, Li J, Li Z, Xie W. Nanozyme-linked immunosorbent assay for porcine circovirus type 2 antibody using HAuCl4/H2O2 coloring system. *Microchem J.* (2020) 157:105079. doi: 10.1016/j.microc.2020.105079
36. Seal BS, King DJ, Sellers HS. The avian response to Newcastle disease virus. *Dev Comp Immunol.* (2000) 24:257–68. doi: 10.1016/S0145-305X(99)00077-4
37. Alexander D, Saif Y, Barnes H, Glisson J, Fadly A, Mcdougald L, et al. *Diseases of Poultry*. 12th ed. Ames, IA. (2003). p. 75–98.
38. Ganar K, Das M, Sinha S, Kumar S. Newcastle disease virus: current status and our understanding. *Virus Res.* (2014) 184:71–81. doi: 10.1016/j.virusres.2014.02.016
39. Hongzhuan Z, Ying T, Xia S, Jinsong G, Zhenhua Z, Beiyu J, et al. Preparation of the inactivated Newcastle disease vaccine by plasma activated water and evaluation of its protection efficacy. *Appl Microbiol Biot.* (2020) 104:107–17. doi: 10.1007/s00253-019-10106-8
40. Miller PJ, Koch G. Newcastle disease. *Dis Poultry.* (2013) 13:89–138.
41. Senne Da.D. Newcastle disease. In: Saif YM, Fadly AM, Glisson JR, McDougald LR, Nolanand LK, Swayne DE, editors. *Diseases of Poultry*. 12th ed. Ames, IA: Iowa State University Press (2008). p. 75–100.

42. Yang F, Li Y, Jin X, Xu Q, Cheng F, Wang X. Immunosensor-based rapid quantitative detection of Newcastle disease virus antibodies using innovative gold immunochromatographic assay. *J Appl Microbiol.* (2020) 129:1751–7. doi: 10.1111/jam.14688
43. Wang G, Xie P, Xiao C, Yuan P, Su X. Magnetic fluorescent composite nanoparticles for the fluoroimmunoassays of newcastle disease virus and avian virus arthritis virus. *J Fluoresc.* (2010) 20:499–506. doi: 10.1007/s10895-009-0573-9
44. Frohnmeyer E, Tuschel N, Sitz T, Hermann C, Dahl GT, Schulz F, et al. Aptamer lateral flow assays for rapid and sensitive detection of cholera toxin. *Analyst.* (2019) 144:1840–9. doi: 10.1039/C8AN01616J
45. Song K-M, Lee S, Ban C. Aptamers and their biological applications. *Sensors.* (2012) 12:612–31. doi: 10.3390/s120100612
46. Hugh-Jones M, De Vos V. Anthrax and wildlife. *Rev Sci Tech Oie.* (2002) 21:359–84. doi: 10.20506/rst.21.2.1336
47. Rajput M, Kamboh AA, Dewani P, Umrani AP, Rind R. Occurrence of Anthrax spores in small ruminants hair/wool in district Tharparkar, Sindh. *J Anim Health Prod.* (2017) 5:5–9. doi: 10.14737/journal.jahp/2017/5.1.5.9
48. Fasanella A, Galante D, Garofolo G, Jones MH. Anthrax undervalued zoonosis. *Vet Microbio.* (2010) 140:318–31. doi: 10.1016/j.vetmic.2009.08.016
49. Hao R-Z, Song H-B, Zuo G-M, Yang RF, Wei H-P, Wang D-B, et al. DNA probe functionalized QCM biosensor based on gold nanoparticle amplification for Bacillus anthracis detection. *Biosens Bioelectron.* (2011) 26:3398–404. doi: 10.1016/j.bios.2011.01.010
50. Deng H, Zhang X, Kumar A, Zou G, Zhang X, Liang, et al. Long genomic DNA amplicons adsorption onto unmodified gold nanoparticles for colorimetric detection of Bacillus anthracis. *Chem Comm.* (2013) 49:51–3. doi: 10.1039/C2CC37037A
51. Karimi F, Dabbagh S. Gel green fluorescence ssDNA aptasensor based on carbon nanotubes for detection of anthrax protective antigen. *Int J Biol Macromol.* (2019) 140:842–50. doi: 10.1016/j.ijbiomac.2019.08.219
52. Seleem MN, Boyle SM, Sriranganathan N. Brucellosis: a re-emerging zoonosis. *Vet Microbiol.* (2010) 140:392–8. doi: 10.1016/j.vetmic.2009.06.021
53. Pal D, Boby N, Kumar S, Kaur G, Ali SA, Reboud J, et al. Visual detection of Brucella in bovine biological samples using DNA-activated gold nanoparticles. *PLoS ONE.* (2017) 12:e0180919. doi: 10.1371/journal.pone.0180919
54. Sattarahmady N, Tondro G, Gholchin M, Heli H. Gold nanoparticles biosensor of Brucella spp. genomic DNA: Visual and spectrophotometric detections. *Biochem Eng J.* (2015) 97:1–7. doi: 10.1016/j.bej.2015.01.010
55. Li X, Zhu P, Liu C, Pang H. One step synthesis of boron-doped carbon nitride derived from 4-pyridylboronic acid as biosensing platforms for assessment of food safety. *Chem Commun.* (2019) 55:9160–9163. doi: 10.1039/C9CC03787J
56. Wang Y, Zhao G, Li X, Liu L, Cao W, Wei Q. Electrochemiluminescent competitive immunosensor based on polyethyleneimine capped SiO2 nanomaterials as labels to release Ru (bpy) 32+ fixed in 3D Cu/Ni oxalate for the detection of aflatoxin B1. *Biosens Bioelectron.* (2018) 101:290–6. doi: 10.1016/j.bios.2017.10.042
57. Kumar P, Mahato DK, Kamle M, Mohanta TK, Kang SG. Aflatoxins: a global concern for food safety, human health and their management. *Front Microbiol.* (2017) 7:2170. doi: 10.3389/fmicb.2016.02170
58. Nodoushan SM, Nasirizadeh N, Kachuei R, Fooladi AaI. Electrochemical detection of aflatoxin B1: an aptasensor prepared using graphene oxide and gold nanowires. *Anal Methods.* (2019) 11:6033–42. doi: 10.1039/C9AY01673B
59. US FDA. *Guidance for Industry: Action Levels for Poisonous or Deleterious Substances in Human Food and Animal Feed.* (2000). US FDA, Washington, DC. Available online at: http://www.fda.gov/Food/GuidanceComplianceRegulatoryInformation/GuidanceDocuments/ChemicalContaminantsandPesticides/ucm077969.htm (accessed February 26, 2021).
60. Tan H, Ma L, Guo T, Zhou H, Chen L, Zhang Y, et al. A novel fluorescence aptasensor based on mesoporous silica nanoparticles for selective and sensitive detection of aflatoxin B1. *Anal Chim Acta.* (2019) 1068:87–95. doi: 10.1016/j.aca.2019.04.014

Conflict of Interest: The authors declare that the research was conducted in the absence of any commercial or financial relationships that could be construed as a potential conflict of interest.

frontiers in Veterinary Science

ORIGINAL RESEARCH
published: 23 July 2021
doi: 10.3389/fvets.2021.689085

Copper/Carbon Core/Shell Nanoparticles: A Potential Material to Control the Fish Pathogen *Saprolegnia parasitica*

*Jv Zhang[1], Juncai Chen[2], Qianjun Huang[1], Brett MacKinnon[1], Omid Nekouei[1], Hong Liu[3], Peng Jia[3,4], Jinjin Wang[3], Na Li[3], Liqing Huang[1], Ying Yang[1], Pok Ng[1] and Sophie St-Hilaire[1]**

[1] Department of Infectious Diseases and Public Health, Jockey Club College of Veterinary Medicine and Life Sciences, City University of Hong Kong, Hong Kong, China, [2] State Key Laboratory of Aquatic Animal Health at the Animal and Plant Inspection and Quarantine Technical Centre, General Administration of Customs, Shenzhen, China, [3] Animal and Plant Inspection and Quarantine Technical Center, Shenzhen Customs District, Shenzhen, China, [4] Shenzhen Technology University, Shenzhen, China

Copper-based fungicides have a long history of usage in agriculture and aquaculture. With the rapid development of metal-based nanoparticles, copper-based nanoparticles have attracted attention as a potential material for prevention and control of *Saprolegnia parasitica*. The present study investigated the effectiveness of copper/carbon core/shell nanoparticles (CCCSNs) and a commercial CCCSNs filter product (COPPERWARE®) against *S. parasitica* in a recirculating system. Results showed that the growth of agar plugs with mycelium was significantly suppressed after exposure to both CCCSNs powder and COPPERWARE® filters. Even the lowest concentration of CCCSNs used in our study (i.e., 100 mg/mL) exhibited significant inhibitory effects on *S. parasitica*. The smallest quantity of the filter product COPPERWARE® (3.75 × 3.7 × 1.2 cm, 2.58 g) used in our aquarium study also demonstrated significant inhibition compared with the control group. However, we observed leaching of copper into the water especially when larger quantities of COPPERWARE® were used. Water turbidity issues were also observed in tanks with the filter material. Besides these issues, which should be further investigated if the product is to be used on aquatic species sensitive to copper, CCCSNs has promising potential for water disinfection.

Keywords: *Saprolegnia parasitica*, metal-based nanoparticles, CCCSNs, filter, water disinfection

OPEN ACCESS

Edited by:
Renata Katsuko Takayama Kobayashi, State University of Londrina, Brazil

Reviewed by:
Vaibhav Srivastava, Royal Institute of Technology, Sweden
Jingfeng Sun, Tianjin Agricultural University, China

***Correspondence:**
Sophie St-Hilaire
ssthilai@cityu.edu.hk

Specialty section:
This article was submitted to Veterinary Infectious Diseases, a section of the journal Frontiers in Veterinary Science

Received: *31 March 2021*
Accepted: *21 June 2021*
Published: *23 July 2021*

Citation:
Zhang J, Chen J, Huang Q, MacKinnon B, Nekouei O, Liu H, Jia P, Wang J, Li N, Huang L, Yang Y, Ng P and St-Hilaire S (2021) Copper/Carbon Core/Shell Nanoparticles: A Potential Material to Control the Fish Pathogen Saprolegnia parasitica. Front. Vet. Sci. 8:689085. doi: 10.3389/fvets.2021.689085

INTRODUCTION

Saprolegniasis is one of the most prevalent oomycete diseases in aquaculture (1), and among the Saprolegnia species, *Saprolegnia parasitica* is an important pathogen of finfish (2). The historical treatment for saprolegniasis was malachite green; however, this substance is now banned for use in food fish in many countries due to its teratogenic and mutagenic properties (3). Formalin is now the most commonly used treatment for this pathogen (4), but it also has potential carcinogenic and allergenic properties (5). Formalin treatments are forbidden in some countries (6) and more jurisdictions are expected to follow (7). Several other treatments such as salt (8), bronopol (9), and ozone (10) have been reported to be somewhat effective against *Saprolegnia* spp. However, their use is limited due to either adverse impacts on the environment or the aquatic animals,

or limited efficacy. For example, although prolonged salt immersion is effective to inhibit *S. parasitica*, this treatment is impractical in large freshwater systems (11). Bronopol is effective against saprolegniosis (7), but tolerance to this product has been reported (12). Powerful oxidants such as ozone and hydrogen peroxide can reduce *Saprolegnia* spp., but these may also damage the gills of fish (13, 14). More recently potential inhibitors of *S. parasitica* such as triclosan and azelaic acid have been identified, however, their practical application needs further investigation (15). Despite numerous attempts to find safer, more effective, and environmentally friendly alternatives to malachite green, the solution to controlling saprolegniasis is still elusive (1, 4).

Metal-based nanoparticles with particle sizes <100 nm are being explored as an alternative approach to control infectious diseases caused by pathogenic bacteria (16, 17) and fungi (18, 19). These novel materials have distinct physical and chemical properties (20), different from their bulk counterparts or molecular compounds, that enhance bacterial binding, disruption of cell membranes, inhibition of enzyme activity and DNA synthesis (21, 22). Their promising results have raised interest in evaluating metal-based nanoparticles in the field of aquaculture to reduce pathogens in the water (23–28).

Copper-based nanoparticles are of particular interest in aquaculture because copper-based chemicals have long been used to control algal growth (29, 30), parasites, and saprolegniasis (31–33). For example, traditional copper sulfate was reported to prevent winter kill from occurring in over 90% of the fish before the water mold infection was visible on the fish (34). Copper-based nanoparticles have an increase in surface area to volume ratio, which provides them with a large biological active surface and may improve the efficacy of copper (35). These compounds are starting to be recognized as having a wide range of antifungal and antibacterial properties that could be used in agriculture (36), and in the biomedical field (37–39).

Copper-based nanoparticles have been reported to display better inhibition of fungus relative to other nanoparticles (40). However, the use of copper-based nanoparticles in aquaculture, has focused on the control of aquatic bacteria (41, 42), with limited information on their use for controlling oomycete pathogens such as *S. parasitica*. Copper is cost-effective relative to other metals such as silver, and therefore may be more suitable for low-cost large-scale water disinfection; filters made from these materials may be adapted relatively inexpensively to existing filter systems to reduce fungus-like agents in aquaculture settings.

Copper/carbon core/shell nanoparticles (CCCSNs) are a type of copper-based nanoparticles coated with a thin protective carbon shell (27). This coating is suppose to reduce the amount of copper ions released into the environment. Maintaining copper in a bound state is important in aquaculture as some species of fish, and shrimp do not tolerate exposure to high levels of copper (43, 44). In addition, metallic nanoparticles without a protective coating often have a high propensity to oxidize or undergo other chemical reactions (45). It has been speculated that the core-shell structure of CCCSNs may prevent copper from dissolving into the environment and protect it against chemical reactions, which could provide an environmentally friendly and longer lasting approach to control *S. parasitica* and other microorganisms in water.

The aims of this study were to: (1) investigate the efficiency of CCCSNs against *S. parasitica*; (2) evaluate a commercial CCCSNs filter product (COPPERWARE®) in reducing *S. parasitica* in a recirculating aquarium system; and (3) evaluate the effect of the COPPERWARE® on water quality parameters (copper concentration, turbidity, pH, and dissolved oxygen).

MATERIALS AND METHODS

Purification of *Saprolegnia parasitica*

A *Saprolegnia parasitica* isolate stored at −80°C at the State Key Laboratory of Aquatic Animal Health at the Animal and Plant Inspection and Quarantine Technical Centre, in Shenzhen Customs District, General Administration of Customs, P. R. China was streaked on solid potato dextrose agar (PDA) medium (Land Bridge Co., Ltd., Beijing, China) for 3 days at 25°C. Subsequently, an agar plug was cut from the PDA medium and used in our experiments.

CCCSNs Powder on the Growth of Mycelium

The anti-oomycete activity of CCCSNs (Suzhou Guanjie Technology Co., Ltd., China) was examined by evaluating the growth of *S. parasitica* on PDA with different concentrations of CCCSNs (1, 5, 10, 50, 100, 500, 1,000, 1,500, 2,000 mg/L). In brief, CCCSNs were added to PDA while it was in liquid form and sonicated (100 W, 40 kHz) for 30 min under 60°C to increase the dispersion of the nanoparticles (46). The mixture was poured into petri plates. There were three replicates for each concentration including the negative control, which had no CCCSNs. An 8 mm diameter agar plug with mycelium growth was placed in the center of each plate. Cultures were incubated at 25°C and the growth of the hyphae was measured after 24, 48, 72, and 144 h. The colony diameter of the growing mycelium was determined by averaging two measurements taken at 90° from each other. We compared the growth of the mycelium plugs at different concentrations of CCCSNs over time as explained in section Statistical Analyses.

CCCSNs Filter (COPPERWARE®) Filtration Experiments

After we confirmed the minimum effective concentration of CCCSNs on the mycelium growth of *S. parasitica*, a commercial filter containing CCCSNs branded as COPPERWARE® (Suzhou Guanjie Technology Co., Ltd., China) was included in aquarium filters to assess the water-disinfection properties of the filter product. We conducted two independent experiments (experiment 1 and experiment 2) to assess the anti-oomycete property of different quantities of COPPERWARE® as described in **Table 1**. During these studies, we also measured changes in water quality (pH, dissolved oxygen, turbidity, ammonia, nitrite, nitrate, copper) over time. Lastly, at the end of experiment 2, we assessed whether *S. parasitica* had the ability to rejuvenate when transferred to an environment without CCCSNs.

Experiment 1

In experiment 1, we compared two quantities of COPPERWARE® (see **Table 1** for quantities) on the growth of *S. parasitica* for a duration of 72 h. In brief, nine aquariums (three with the high quantity of COPPERWARE®, labeled with L-copperware; three with a medium quantity of COPPERWARE®, labeled with M-copperware; and three control tanks, labeled with No-copperware) with a volume of 5 L were filled with 4.98 mL of deionized water. An 8 mm PDA agar plug colonized with *S. parasitica* and 22 mL of potato dextrose broth were added to each aquarium. Continuous circulation through the filtration system (SZ-230A, Jeneca, China) was administered during the experiment. At the end of the experiment (72 h), agar plugs from each tank were removed and the colony diameters were measured by averaging two measurements taken at 90° from each other. We compared the growth of the agar plug between treatments over time (refer to section Statistical Analyses). Microscopy (AXio Imager M1, ZEISS, Germany) was used to inspect the morphology of *S. parasitica* at the end of the trial.

TABLE 1 | Description of the parameters used in the COPPERWARE® filtration experiments (experiment 1 and experiment 2).

Experiment	Duration	Fungus size	Different sizes of COPPERWARE®[a]
Experiment 1	72 h	8 mm	L-copperware: 7.5 × 3.7 × 2.4 cm, 9.46 g M-copperware: 7.5 × 3.7 × 1.2 cm, 4.96 g No-copperware: filter without CCCSNs
Experiment 2	144 h	5 mm	M-copperware: 7.5 × 3.7 × 1.2 cm, 4.96 g S-copperware: 3.75 × 3.7 × 1.2 cm, 2.58 g No-copperware: filter without CCCSNs

[a] *L, large; M, medium; S, small; No, no CCCSNs in the filter.*

Experiment 2

In experiment 2, we compared two different sizes of COPPERWARE® filter material. In this experiment three tanks were set up with a medium quantity of COPPERWARE® labeled M-copperware and three tanks had a small quantity

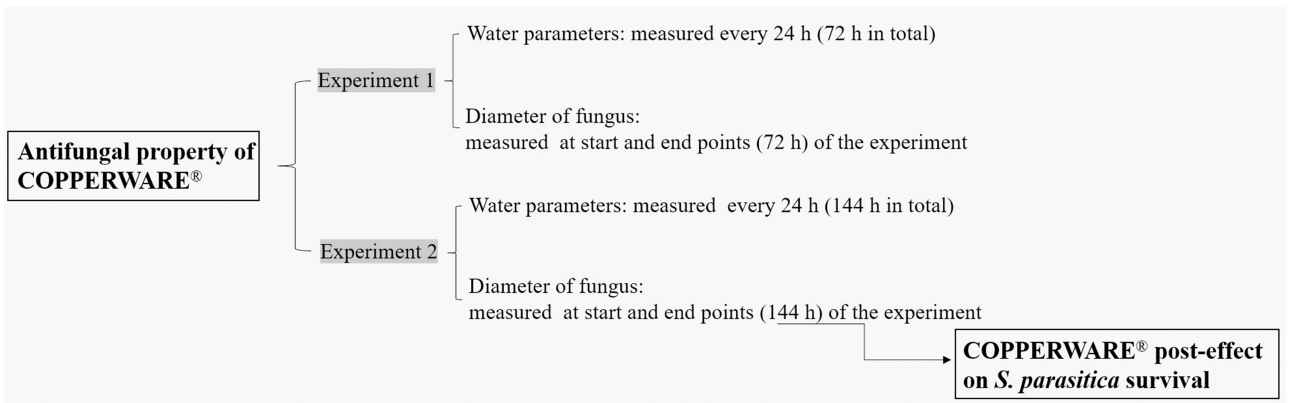

FIGURE 1 | The flow chart of the CCCSNs filter (COPPERWARE®) filtration experiments.

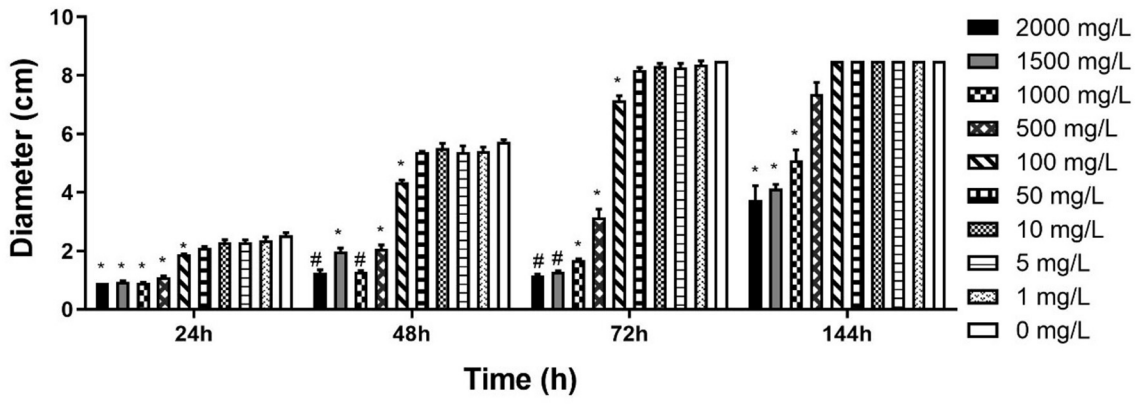

FIGURE 2 | The diameter of *S. parasitica* at different timepoints after treating with different concentrations CCCSNs. *: $0.001 < p < 0.05$, #: $p < 0.001$. Error bars are ± SD, $n = 3$.

of COPPERWARE® labeled S-copperware. We also had three tanks with the filter material, but no CCCSNs for comparison. An 5 mm agar plug size was added to the tanks and monitored for a duration of 144 h. The anti-oomycete efficiency of the material was assessed in a similar manner as described in experiment 1.

Post-effect of COPPERWARE® on *S. parasitica* Survival

To determine whether *S. parasitica* was killed or simply inhibited by COPPERWARE®, agar plugs from tanks in experiment 2 were removed at the end of the study and transferred to a new PDA medium without CCCSNs (**Figure 1**). The initial diameter of the *S. parasitica* was identified as the diameter measured at the end of experiment 2 (144 h). Agar plugs were incubated at 25°C for 72 h and measured every 24 h. The growth of the plugs post exposure to COPPERWARE® was compared over time (refer to section Statistical Analyses).

Water Quality

Dissolved oxygen and pH were measured in the tanks at 24 h intervals using probes (YSI ProODO, Xylnm, USA) during the filtration experiments (experiment 1 and experiment 2). To determine water turbidity, optical densities (OD_{600}) were measured every 24 h with a spectrophotometer (Biophotometer, Eppendorf, Germany). We assessed the levels of copper (ionized and bound), ammonia, nitrite, and nitrate in the water at the end of the experiments using HACH test kits (HACH Inc. Loveland, Colorado). We compared the water quality parameters across treatment groups over time (refer to section Statistical Analyses).

Statistical Analyses

To compare the potential effects of treatments on the growth of the agar plugs over time (repeated measurements) we used mixed-effects linear regression models controlling for time. Data from each experiment were analyzed separately. The level of significance was set at 0.05. All statistical analyses were performed in GraphPad Prism software (Version 8.0.1, GraphPad Software, San Diego, USA). In brief, we compared the growth of mycelium plugs (diameter in cm) between treatment groups (10 groups for CCCSNs powder experiment, three groups for filtration experiment 1 and 2, and the post-effect evaluation) over time (5 time points for CCCSNs powder experiment; 2 time points for filtration experiments 1 and 2; and 4 time points for the post-effect evaluation). The main effects and the interaction terms between treatments and time points were included in the models as fixed effects, and the individual plates or tanks were included as random effects to account for the repeated measurements within each of the plates or tanks (depending on the experiment) over time.

Water quality parameters were also compared between the treatment groups in a similar manner using mixed-effects linear regression models. Tukey's HSD test was used following the regression models in the case of multiple comparisons.

RESULTS

CCCSNs on the Growth of Mycelium

CCCSNs inhibited the growth of *S. parasitica*, and this effect appeared to be dose-dependent (**Figure 2** and **Supplementary Figure 1**). Compared with the control group, *S. parasitica* mycelia was significantly reduced in the presence of CCCSNs at concentrations of 2,000, 1,500, and 1,000 mg/L. All three of these concentrations of CCCSNs significantly inhibited the growth of *S. parasitica* at all experimental time points ($p < 0.05$). The lower concentrations of CCCSNs (i.e., 500 and 100 mg/L) only significantly inhibited the growth for the first 3 days (**Figure 2**).

COPPERWARE® Filtration Experiments

COPPERWARE® inhibited the growth of *S. parasitica* in aquarium water regardless of the quantity of material used in our filters (**Figure 3** and **Supplementary Figure 2**). At the end of the exposure, the size of agar plugs in the treatment groups was significantly smaller than those of the control group in experiments 1 and 2 ($p < 0.001$) (**Figure 3**).

Microscopic examination of *S. parasitica* following exposure to COPPERWARE® revealed morphological changes in the

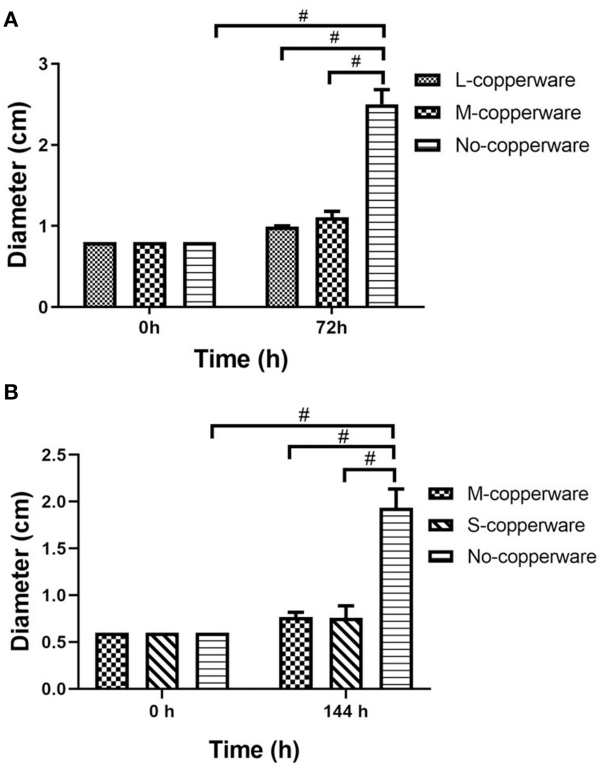

FIGURE 3 | Diameter of *S. parasitica* after water treatment with different quantities of COPPERWARE® filters (L-copperware: 7.5 × 3.7 × 2.4 cm, 9.46 g; M-copperware: 7.5 × 3.7 × 1.2 cm, 4.96 g; S-copperware: 3.75 × 3.7 × 1.2 cm, 2.58 g) and commercial filter with no CCCSNs (No-copperware) in **(A)** experiment 1 and **(B)** experiment 2. #: $p < 0.001$. Error bars are ± SD, $n = 3$.

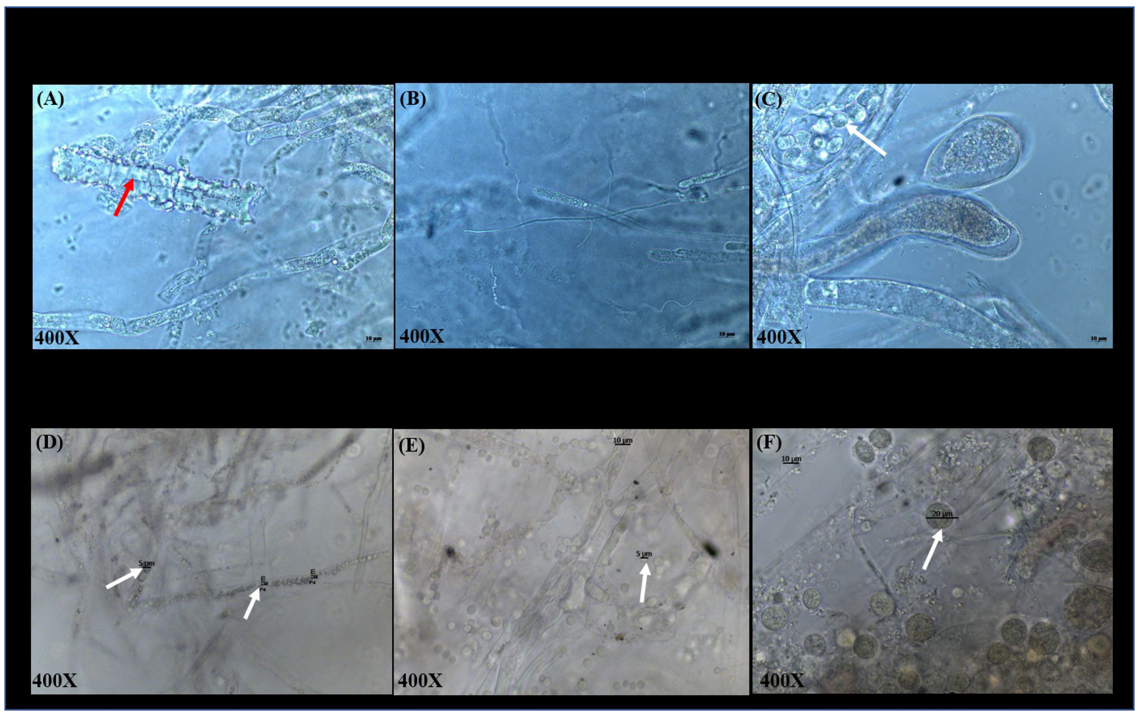

FIGURE 4 | Microscopic observations of *S. parasitica* after treating tanks with different quantities of COPPERWARE® (L-copperware: 7.5 × 3.7 × 2.4 cm, 9.46 g; M-copperware: 7.5 × 3.7 × 1.2 cm, 4.96 g; S-copperware: 3.75 × 3.7 × 1.2 cm, 2.58 g) and commercial filter with no CCCSNs (No-copperware) in experiment 1 at 72 h **(A–C)** and experiment 2 at 144 h **(D–F)**. red arrow: damaged hyphae; White arrow: spores. The spore size in **(D)**: 2–5 μm; The spore size in **(E)**: around 5 μm; The spore size in **(F)**: around 20 μm.

hyphae (**Figure 4**). In experiment 1, *S. parasitica* treated with COPPERWARE® in both the L-copperware and M-copperware groups displayed some damaged hyphae compared to the non-treated group. The size of spores in the COPPERWARE® treated and untreated groups may have also been affected. We observed that treated *S. parasitica* commonly had spores with diameters ranging between 2 and 5 μm and untreated *S. parasitica* had spores ∼10-fold larger in diameter at 20 μm (**Figure 4**).

Post-exposure Effect of COPPERWARE® on *S. parasitica* Survival

Once the treatment (exposure to COPPERWARE®) was halted, the mycelium growth remained minimal for the first 24 and 48 h compared to the non-treated control group ($p < 0.05$). However, after 72 h, the mycelium plugs appeared to increase in size. Only one treated group (S-copperware) still had a statistically smaller agar plug relative to the control systems by the end of the study (**Figure 5** and **Supplementary Figure 3**).

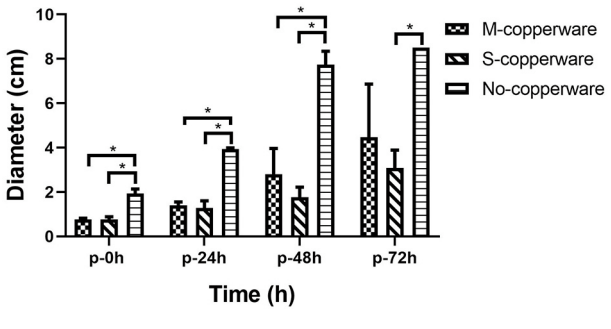

FIGURE 5 | Post-effect of different quantities of COPPERWARE® (M-copperware: 7.5 × 3.7 × 1.2 cm, 4.96 g; S-copperware: 3.75 × 3.7 × 1.2 cm, 2.58 g; No-copperware: control group with no CCCSNs in the filter) on the development of *S. parasitica*. *: $0.001 < p < 0.05$. *p*: post effect after the removal of the COPPERWARE®. Error bars are ± SD, $n = 3$.

Water Quality

Copper was detected in the COPPERWARE® treated groups, and the range of copper concentration based on the HACH test was higher for tanks treated with larger quantities of the product (**Table 2**). The concentration of copper in the water was as high as the detection limit of our test kits (3 mg/L) in the treatment group with the largest quantity of COPPERWARE® (L-copperware: 7.5 × 3.7 × 2.4 cm, 9.46 g). Concentrations of dissolved oxygen, ammonia, nitrite, and nitrate were all within the normal range for all treatment groups (**Supplementary Figure 4** and **Supplementary Table 1**). However, at the end of experiment 1, the pH in the L-copperware treated group was significantly lower than the control ($p < 0.05$) (**Supplementary Figure 4**).

The turbidity of water changed over time in the treatment tanks. After 72 h, 96 h and 120 h of exposure

TABLE 2 | Copper concentration after water treatment with different sizes of COPPERWARE® filters at the end of experiments 1 and 2.

Experiment	Treatment[a]	Copper (mg/L)
Experiment 1 (72 h)	L-copperware	≥3
	M-copperware	1–3
	No-copperware	0
Experiment 2 (144 h)	M-copperware	1–3
	S-copperware	0.5–1
	No-copperware	0

[a] *L-copperware: 7.5 × 3.7 × 2.4 cm, 9.46 g; M-copperware: 7.5 × 3.7 × 1.2 cm, 4.96 g; S-copperware: 3.75 × 3.7 × 1.2 cm, 2.58 g; and No-copperware: commercial filter with no CCCSNs.*

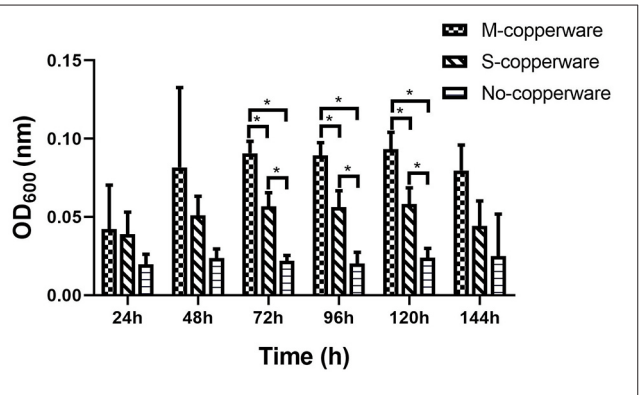

FIGURE 6 | Turbidity of water in experiment 2 assessed via spectrophotometer. M- copperware: 7.5 × 3.7 × 1.2 cm, 4.96 g; S-copperware: 3.75 × 3.7 × 1.2 cm, 2.58 g; No-copperware: control group with no CCCSNs in the filter. *: $0.001 < p < 0.05$. Error bars are ± SD, $n = 3$.

to COPPERWARE®, OD_{600} measurements water in the treated groups were significantly higher compared to the control ($p < 0.05$) (**Figure 6**). This increase in turbidity was particularly obvious in tanks treated with the medium quantity of product (i.e., M-copperware 7.5 × 3.7 × 1.2 cm, 4.96 g) (**Supplementary Figure 5**). The OD_{600} measurements of tanks treated with M-copperware were significantly higher than measurements in control tanks, as well as tanks treated with the smallest quantity of COPPERWARE® (labeled S-copperware with 3.75 × 3.7 × 1.2 cm, 2.58 g) ($p < 0.05$) (**Figure 6**) between 72 and 120 h. Although the water turbidity was still higher in the treated tanks than the control tanks by 144 h post-exposure, this difference was no longer statistically significant (**Figure 6**).

DISCUSSION

Based on the results of this study, it appears that CCCSNs and its commercial filter product (COPPERWARE®) may inhibit the growth of *S. parasitica*. The dose-dependent suppression of the growth of this organism (i.e., minimal growth in the agar plug size) in our experiments (**Figures 2**, **3**) was also supported by morphological evidence of damage to the hyphae and spores (**Figure 4**); however, the effect of CCCSNs on the growth did not persist more than a few days once we removed the filter material from the aquarium (**Figure 5**). This suggests continuous exposure or intermittent exposure to the CCCSNs may be required to maintain *S. parasitica* at a minimal level in aquatic environments.

The dose-dependent disinfection activity of copper nanoparticles has also been reported by others with fungal species (47, 48). Removal of pathogenic *Fusarium* species affecting plants has been demonstrated with copper nanoparticles (36). The antifungal properties of copper nanoparticles were reported to be better than other metal-based nanoparticles (Ag, Zn, and Au nanoparticles), as well as the commercial fungicide containing $Cu(OH)_2$ (49).

Copper nanoparticles have a large surface-to-volume ratio which may enhanced antimicrobial efficiency (40). The mechanism of action of nanoparticles on microbes is not well-established, but the disinfection properties may be through a direct metal-microbial contact mechanism, which is enhanced by the large surface area to the volume of the nanoparticles (50–52). It is also possible in our study that free copper ions were released and played a role in the inhibition of *S. parasitica* growth, as we measured copper in the water after the treatment. This has been reported to be one of the microbial killing mechanisms of metal-based nanoparticles (53, 54). Direct contact with copper ions causes a decline in the membrane integrity of microbes, leading to a subsequent leakage of cell contents and eventually cell death (51, 55). Copper ions can also penetrate the cell, leading to lipid peroxidation, protein oxidation and DNA damage (17, 56, 57).

We observed a dose-dependent increase in turbidity during experiment 2 (**Figure 6**), which could potentially have been related to a stress response sporulation event. Although we could not verify this phenomenon, Kasprowicz et al. (58) reported an increase in the release of spores from *Fusarium culmorum* associated with exposure to silver nanoparticles. Spores are better adapted to survive harsh environmental conditions with their thick cell walls compared to the vegetative cell walls (59). Spores are resistant to many types of environmental stresses such as starvation (60) and heavy-metal exposure (61). It is important to note that the quantity of *S. parasitica* used in this laboratory experiment was high relative to the volume of water. It is possible that under natural levels of the pathogen, water turbidity would not be noticeably affected even in the event of sporulation.

Interestingly, if sporulation was the reason for the turbidity it did not lead to better germination or mycelial growth, suggesting that successful inhibition on *S. parasitica* in aquatic systems can be achieved in the presence of CCCSNs. The precise concentration of CCCSNs required for inhibition of *S. parasitica* growth in larger aquaculture systems remains to be determined, but this study could be used as a starting point to assess the economic value of incorporating this material into filtration systems. The duration of activity of CCCSNs in a system also needs to be established, and this may be of critical importance because once we removed the COPPERWARE® we eventually observed renewed growth of the oomycete. The fact that *S. parasitica* was able to grow once we removed the agar plugs from the COPPERWARE®-challenged water was unfortunate,

but not unexpected given the resilience of *Saprolegnia* spp. spores to environmental insults (62). Microscopic evaluation of the oomycete pathogens after exposure to CCCSNs showed that the spores remained intact and within the hyphae even though they were smaller in size than the controls (**Figure 4**). The persistence of spores in hyphae may have enabled the rejuvenation of *S. parasitica* when transferred from COPPERWARE®-challenged tanks to a copper-free environment (**Figure 5** and **Supplementary Figure 3**). Zinc oxide nanoparticles have also been shown to be fungistatic rather than fungicidal at certain concentrations against *F. graminearum* (63).

The continuous use of COPPERWARE® in the filtration systems at the highest concentration (L-copperware) in our study resulted in high levels of total copper in the water (i.e., above the test detection limit of 3 mg/L). Although the test kit we used measured both copper ions and bound copper, it was concerning to have this level of copper leaching from the filter material. Fortunately, this quantity of COPPERWARE® was not necessary for disinfecting water; we still observed disinfection when we used lower levels of material in our aquaria. However, even using the smallest quantity of COPPERWARE® (S-copperware) we were able to detect low levels of total copper (0.5–1 mg/L). This level of material was within the safe range of drinking water (64), but could still be toxic to some aquatic animals. For example, the 48-h LC50 values of copper sulfate for *Macrobrachium lamarrei* and *Macrobrachium dayanum* were 0.361 and 0.988 mg/L, respectively (65), while the 48-h LC50 for fed neonates of *Daphnia magna* was 18.5 μg/L (66). However, for species like tilapia (*Oreochromis niloticus*), and catfish (*Clarias gariepinus*), the 96-h LC50 values are approximately 58.8 and 70.1 mg/L, respectively (67), which is higher than what we detected in this study using the lowest concentration of COPPERWARE®.

It is not possible to evaluate the toxicity of COPPERWARE® by the measured estimated copper concentration in this study as it may not have all been free copper ions. If materials constructed from CCCSNs are to be explored for use in aquaculture, further research is needed to reduce or prevent copper released from nanoparticles to avoid copper toxicity. This advice has also been advocated by other researchers (47). The other water quality parameters monitored in this study were not negatively impacted by the use of COPPERWARE®.

The potential leaching of copper from the commercial CCCSN material tested in this study may be reduced by improving the coating of the nanoparticles on the filtration material. Given this issues is rectified, our study indicates that CCCSNs could be quite effective at controlling *S. parasitica* and is worth further investigation. Further research and animal safety assessments are required before this technology can be scaled up to large aquaculture systems, but the initial findings of this study are promising if the CCCSN can remain attached to the filter material more effectively.

DATA AVAILABILITY STATEMENT

The original contributions presented in the study are included in the article/**Supplementary Material**, further inquiries can be directed to the corresponding author/s.

AUTHOR CONTRIBUTIONS

JZ and SS-H came up with the idea of the study. JC and QH assisted with data acquisition. HL, PJ, and JW provided the stored *S. parasitica* and essential equipment for experimenting, as well as guidance in the laboratory for the culture of the pathogen. NL assisted with the analysis of *S. parasitica* morphology. BM, LH, YY, and PN were involved in manuscript revising. ON contributed to the statistical analysis. JZ conducted most of the studies and wrote the manuscript with the assistance and comments from JC, QH, BM, ON, HL, PJ, JW, NL, LH, YY, PN, and SS-H. All authors contributed to the article and approved the submitted version.

FUNDING

This work was carried out with financial support from UK Government – Department of Health and Social Care (DHSC), Global AMR Innovation Fund (GAMRIF) and the International Development Research Centre (IDRC), Ottawa, Canada (grant #109050-001). The views expressed herein do not necessarily represent those of IDRC or its Board of Governors.

ACKNOWLEDGMENTS

We would like to thank Animal and Plant Inspection and Quarantine Technical Center, Shenzhen Customs District, Shenzhen, China for the experimental site. Much appreciation for the funding support from the IDRC.

SUPPLEMENTARY MATERIAL

The Supplementary Material for this article can be found online at: https://www.frontiersin.org/articles/10.3389/fvets.2021.689085/full#supplementary-material

REFERENCES

1. Ali SE, Thoen E, Evensen O, Wiik-Nielsen J, Gamil AA, Skaar I. Mitochondrial dysfunction is involved in the toxic activity of boric acid against Saprolegnia. *PLoS ONE*. (2014) 9:e110343. doi: 10.1371/journal.pone.0110343
2. Shin S, Kulatunga DCM, Dananjaya SHS, Nikapitiya C, Lee J, De Zoysa M. *Saprolegnia parasitica* isolated from rainbow trout in Korea: characterization, anti-Saprolegnia activity and host pathogen interaction in zebrafish disease model. *Mycobiology*. (2017) 45:297–311. doi: 10.5941/MYCO.2017.45.4.297
3. Culp SJ, Mellick PW, Trotter RW, Greenlees KJ, Kodell RL, Beland FA. Carcinogenicity of malachite green chloride and leucomalachite green in B6C3F1 mice and F344 rats. *Food Chem Toxicol.* (2006) 44:1204–12. doi: 10.1016/j.fct.2006.01.016
4. Gieseker CM, Serfling SG, Reimschuessel R. Formalin treatment to reduce mortality associated with *Saprolegnia parasitica* in

rainbow trout, *Oncorhynchus mykiss*. *Aquaculture.* (2006) 253:120–9. doi: 10.1016/j.aquaculture.2005.07.039
5. Tedesco P, Fioravanti ML, Galuppi R. In vitro activity of chemicals and commercial products against *Saprolegnia parasitica* and Saprolegnia delica strains. *J Fish Dis.* (2019) 42:237–48. doi: 10.1111/jfd.12923
6. Magaraggia M, Faccenda F, Gandolfi A, Jori G. Treatment of microbiologically polluted aquaculture waters by a novel photochemical technique of potentially low environmental impact. *J Environ Monit.* (2006) 8:923–31. doi: 10.1039/b606975d
7. Ali SE, Thoen E, Evensen O, Skaar I. Boric acid inhibits germination and colonization of Saprolegnia spores *in vitro* and *in vivo*. *PLoS ONE.* (2014) 9:e91878. doi: 10.1371/journal.pone.0091878
8. Mifsud C, Rowland SJ. Use of salt to control ichthyophthiriosis and prevent saprolegniosis in silver perch, Bidyanus bidyanus. *Aquac Res.* (2008) 39:1175–80. doi: 10.1111/j.1365-2109.2008.01981.x
9. Branson E. Efficacy of bronopol against infection of rainbow trout (Oncorhynchus mykiss) with the fungus Saprolegnia species. *Vet Record.* (2002) 151:539–41. doi: 10.1136/vr.151.18.539
10. Forneris G, Bellardi S, Palmegiano G, Saroglia M, Sicuro B, Gasco L, et al. The use of ozone in trout hatchery to reduce saprolegniasis incidence. *Aquaculture.* (2003) 221:157–66. doi: 10.1016/S0044-8486(02)00518-5
11. Noga EJ. PART II: PROBLEM LIST, Chapter 8, problem 34: typical water mold infection. In: *Fish Disease: Diagnosis and Treatment.* Ames, IA: Wiley-Blackwell (2010). p. 161–2.
12. Rezinciuc S, Sandoval-Sierra JV, Dieguez-Uribeondo J. Molecular identification of a bronopol tolerant strain of *Saprolegnia australis* causing egg and fry mortality in farmed brown trout, Salmo trutta. *Fungal Biol.* (2014) 118:591–600. doi: 10.1016/j.funbio.2013.11.011
13. Fukunaga K, Suzuki T, Takama K. Effect of ozone exposure on the compositions of gill and erythrocyte membrane lipids and proteins of Japanese charr (Salvelinus leucomaenis). *Comp Biochem Physiol Part B.* (1991) 100:481–7. doi: 10.1016/0305-0491(91)90208-U
14. Mustafa S, Al-Rudainy A, Al-Faragi J. Assessment of hydrogen peroxide on histopathology and survival rate in common carp, Cyprinus carpio l. infected with saprolegniasis. *Iraqi J Agric Sci.* (2019) 50:697–704.
15. Kumar S, Mandal RS, Bulone V, Srivastava V. Identification of growth inhibitors of the fish pathogen Saprolegnia parasitica using *in silico* subtractive proteomics, computational modeling, biochemical validation. *Front Microbiol.* (2020) 11:571093. doi: 10.3389/fmicb.2020.571093
16. Hajipour MJ, Fromm KM, Ashkarran AA, de Aberasturi DJ, de Larramendi IR, Rojo T, et al. Erratum: antibacterial properties of nanoparticles:[Trends in Biotechnology 30 (2012), 499–511]. *Trends Biotechnol.* (2013) 31:61–2. doi: 10.1016/j.tibtech.2012.10.007
17. Suresh AK, Pelletier DA, Doktycz MJ. Relating nanomaterial properties and microbial toxicity. *Nanoscale.* (2013) 5:463–74. doi: 10.1039/C2NR32447D
18. Chwalibog A, Sawosz E, Hotowy A, Szeliga J, Mitura S, Mitura K, et al. Visualization of interaction between inorganic nanoparticles and bacteria or fungi. *Int J Nanomed.* (2010) 5:1085. doi: 10.2147/IJN.S13532
19. Stampoulis D, Sinha SK, White JC. Assay-dependent phytotoxicity of nanoparticles to plants. *Environ Sci Technol.* (2009) 43:9473–9. doi: 10.1021/es901695c
20. Shaalan M, Saleh M, El-Mahdy M, El-Matbouli M. Recent progress in applications of nanoparticles in fish medicine: a review. *Nanomed Nanotechnol Biol Med.* (2016) 12:701–10. doi: 10.1016/j.nano.2015.11.005
21. Herman A, Herman AP. Nanoparticles as antimicrobial agents: their toxicity and mechanisms of action. *J Nanosci Nanotechnol.* (2014) 14:946–57. doi: 10.1166/jnn.2014.9054
22. Huh AJ, Kwon YJ. "Nanoantibiotics:" a new paradigm for treating infectious diseases using nanomaterials in the antibiotics resistant era. *J Control Release.* (2011) 156:128–45. doi: 10.1016/j.jconrel.2011.07.002
23. Dankovich TA, Smith JA. Incorporation of copper nanoparticles into paper for point-of-use water purification. *Water Res.* (2014) 63:245–51. doi: 10.1016/j.watres.2014.06.022
24. De Gusseme B, Sintubin L, Baert L, Thibo E, Hennebel T, Vermeulen G, et al. Biogenic silver for disinfection of water contaminated with viruses. *Appl Environ Microbiol.* (2010) 76:1082–7. doi: 10.1128/AEM.02433-09
25. Elsaka SE, Hamouda IM, Swain MV. Titanium dioxide nanoparticles addition to a conventional glass-ionomer restorative: influence on physical and antibacterial properties. *J Dent.* (2011) 39:589–98. doi: 10.1016/j.jdent.2011.05.006
26. Suman TY, Ravindranath RRS, Elumalai D, Kaleena PK, Ramkumar R, Perumal P, et al. Larvicidal activity of titanium dioxide nanoparticles synthesized using Morinda citrifolia root extract against Anopheles stephensi, Aedes aegypti and Culex quinquefasciatus and its other effect on non-target fish. *Asian Pac J Trop Dis.* (2015) 5:224–30. doi: 10.1016/S2222-1808(14)60658-7
27. Wu Q, Lei Y, Lian K, Qi Y. Copper/carbon core shell nanoparticles as additive for natural fiber/wood plastic blends. *BioResources.* (2012) 7:3213–22.
28. Zhang L, Pornpattananangku D, Hu CM, Huang CM. Development of nanoparticles for antimicrobial drug delivery. *Curr Med Chem.* (2010) 17:585–94. doi: 10.2174/092986710790416290
29. Masuda K, Boyd CE. Comparative evaluation of the solubility and algal toxicity of copper sulfate and chelated copper. *Aquaculture.* (1993) 117:287–302. doi: 10.1016/0044-8486(93)90326-T
30. Song L, Marsh T, Voice T, Long D. Loss of seasonal variability in a lake resulting from copper sulfate algaecide treatment. *Phys Chem Earth.* (2011) 36:430–5. doi: 10.1016/j.pce.2010.04.016
31. Marking L, Rach J, Schreier T. American fisheries society evaluation of antifungal agents for fish culture. *Progr Fish Culturist.* (1994) 56:225–31. doi: 10.1577/1548-8640(1994)056<0225:AFSEOA>2.3.CO;2
32. Straus DL, Mitchell AJ, Carter RR, Steeby JA. Hatch rate of channel catfish Ictalurus punctatus (Rafinesque 1818) eggs treated with 100 mg L– 1 copper sulphate pentahydrate. *Aquac Res.* (2012) 43:14–8. doi: 10.1111/j.1365-2109.2010.02791.x
33. Sun Q, Hu K, Yang XL. The efficacy of copper sulfate in controlling infection of Saprolegnia parasitica. *J World Aquac Soc.* (2014) 45:220–5. doi: 10.1111/jwas.12113
34. Bly J, Quiniou S, Lawson L, Clem L. Therapeutic and prophylactic measures for winter saprolegniosis in channel catfish. *Dis Aquat Org.* (1996) 24:25–33. doi: 10.3354/dao024025
35. Giannousi K, Avramidis I, Dendrinou-Samara C. Synthesis, characterization and evaluation of copper based nanoparticles as agrochemicals against Phytophthora infestans. *RSC Adv.* (2013) 3:21743–52. doi: 10.1039/c3ra42118j
36. Viet PV, Nguyen HT, Cao TM, Hieu LV. *Fusarium* antifungal activities of copper nanoparticles synthesized by a chemical reduction method. *J Nanomater.* (2016) 2016:1957612. doi: 10.1155/2016/1957612
37. Borkow G, Gabbay J, Zatcoff RC. Could chronic wounds not heal due to too low local copper levels? *Med Hypotheses.* (2008) 70:610–3. doi: 10.1016/j.mehy.2007.06.006
38. Civardi C, Schubert M, Fey A, Wick P, Schwarze FW. Micronized copper wood preservatives: efficacy of ion, nano, and bulk copper against the brown rot fungus Rhodonia placenta. *PLoS ONE.* (2015) 10:e0142578. doi: 10.1371/journal.pone.0142578
39. O'gorman J, Humphreys H. Application of copper to prevent and control infection. Where are we now? *J Hosp Infect.* (2012) 81:217–23. doi: 10.1016/j.jhin.2012.05.009
40. Servin A, Elmer W, Mukherjee A, De la Torre-Roche R, Hamdi H, White JC, et al. A review of the use of engineered nanomaterials to suppress plant disease and enhance crop yield. *J Nanopart Res.* (2015) 17:1–21. doi: 10.1007/s11051-015-2907-7
41. Chari N, Felix L, Davoodbasha M, Ali AS, Nooruddin T. In vitro and in vivo antibiofilm effect of copper nanoparticles against aquaculture pathogens. *Biocatal Agric Biotechnol.* (2017) 10:336–41. doi: 10.1016/j.bcab.2017.04.013
42. Ghuglot R, Titus W, Agnihotri AS, Krishnakumar V, Krishnamoorthy G, Marimuthu N. Stable copper nanoparticles as potential antibacterial agent against aquaculture pathogens and human fibroblast cell viability. *Biocatal Agric Biotechnol.* (2021) 32:101932. doi: 10.1016/j.bcab.2021.101932
43. Kwok KW, Auffan M, Badireddy AR, Nelson CM, Wiesner MR, Chilkoti A, et al. Uptake of silver nanoparticles and toxicity to early life stages of Japanese medaka (*Oryzias latipes*): effect of coating materials. *Aquat Toxicol.* (2012) 120–1:59–66. doi: 10.1016/j.aquatox.2012.04.012
44. Nemati T, Johari SA, Sarkheil M. Will the antimicrobial properties of ZnONPs turn it into a more suitable option than AgNPs for water filtration? Comparative study in the removal of fish pathogen, Aeromonas hydrophila from the culture of juvenile common carp (*Cyprinus carpio*). *Environ Sci Pollut Res.* (2019) 26:30907–20. doi: 10.1007/s11356-019-06178-8

45. Lian K, Wu Q. *Carbon-Encased Metal Nanoparticles and Sponges, Methods of Synthesis, and Methods of Use (Google Patents)*. United States patent US20090098033A1 (2009).
46. Pradhan A, Seena S, Pascoal C, Cassio F. Copper oxide nanoparticles can induce toxicity to the freshwater shredder *Allogamus ligonifer*. *Chemosphere*. (2012) 89:1142–50. doi: 10.1016/j.chemosphere.2012.06.001
47. Cioffi N, Torsi L, Ditaranto N, Sabbatini L, Zambonin PG, Tantillo G, et al. Antifungal activity of polymer-based copper nanocomposite coatings. *Appl Phys Lett*. (2004) 85:2417–9. doi: 10.1063/1.1794381
48. Kanhed P, Birla S, Gaikwad S, Gade A, Seabra AB, Rubilar O, et al. In vitro antifungal efficacy of copper nanoparticles against selected crop pathogenic fungi. *Mater Lett*. (2014) 115:13–7. doi: 10.1016/j.matlet.2013.10.011
49. Malandrakis AA, Kavroulakis N, Chrysikopoulos CV. Use of copper, silver and zinc nanoparticles against foliar and soil-borne plant pathogens. *Sci Total Environ*. (2019) 670:292–9. doi: 10.1016/j.scitotenv.2019.03.210
50. Chen CL, Maki JS, Rittschof D, Teo SLM. Early marine bacterial biofilm on a copper-based antifouling paint. *Int Biodeterior Biodegradation*. (2013) 83:71–6. doi: 10.1016/j.ibiod.2013.04.012
51. Grass G, Rensing C, Solioz M. Metallic copper as an antimicrobial surface. *Appl Environ Microbiol*. (2011) 77:1541–7. doi: 10.1128/AEM.02766-10
52. Weaver L, Michels HT, Keevil CW. Potential for preventing spread of fungi in air-conditioning systems constructed using copper instead of aluminium. *Lett Appl Microbiol*. (2010) 50:18–23. doi: 10.1111/j.1472-765X.2009.02753.x
53. Slavin YN, Asnis J, Hafeli UO, Bach H. Metal nanoparticles: understanding the mechanisms behind antibacterial activity. *J Nanobiotechnol*. (2017) 15:65. doi: 10.1186/s12951-017-0308-z
54. Tamayo LA, Zapata PA, Vejar ND, Azocar MI, Gulppi MA, Zhou X, et al. Release of silver and copper nanoparticles from polyethylene nanocomposites and their penetration into Listeria monocytogenes. *Mater Sci Eng Mater Biol Appl*. (2014) 40:24–31. doi: 10.1016/j.msec.2014.03.037
55. Mathews S, Hans M, Mucklich F, Solioz M. Contact killing of bacteria on copper is suppressed if bacterial-metal contact is prevented and is induced on iron by copper ions. *Appl Environ Microbiol*. (2013) 79:2605–11. doi: 10.1128/AEM.03608-12
56. Chillappagari S, Seubert A, Trip H, Kuipers OP, Marahiel MA, Miethke M. Copper stress affects iron homeostasis by destabilizing iron-sulfur cluster formation in *Bacillus subtilis*. *J Bacteriol*. (2010) 192:2512–24. doi: 10.1128/JB.00058-10
57. Dupont CL, Grass G, Rensing C. Copper toxicity and the origin of bacterial resistance—new insights and applications. *Metallomics*. (2011) 3:1109–18. doi: 10.1039/c1mt00107h
58. Kasprowicz MJ, Kozioł M, Gorczyca A. The effect of silver nanoparticles on phytopathogenic spores of *Fusarium culmorum*. *Can J Microbiol*. (2010) 56:247–53. doi: 10.1139/w10-012
59. Coluccio AE, Rodriguez RK, Kernan MJ, Neiman AM. The yeast spore wall enables spores to survive passage through the digestive tract of Drosophila. *PLoS ONE*. (2008) 3:e2873. doi: 10.1371/journal.pone.0002873
60. Evelyn, Silva FVM. Differences in the resistance of microbial spores to thermosonication, high pressure thermal processing and thermal treatment alone. *J Food Eng*. (2018) 222:292–97. doi: 10.1016/j.jfoodeng.2017.11.037
61. Baldrian P. Effect of heavy metals on saprotrophic soil fungi. In: *Soil Heavy Metals*. Berlin; Heidelberg: Springer (2010). p. 263–79.
62. Dijksterhuis J. Fungal spores: Highly variable and stress-resistant vehicles for distribution and spoilage. *Food Microbiol*. (2019) 81:2–11. doi: 10.1016/j.fm.2018.11.006
63. Dimkpa CO, McLean JE, Britt DW, Anderson AJ. Antifungal activity of ZnO nanoparticles and their interactive effect with a biocontrol bacterium on growth antagonism of the plant pathogen *Fusarium graminearum*. *Biometals*. (2013) 26:913–24. doi: 10.1007/s10534-013-9667-6
64. Pontius FW. Defining a safe level for copper in drinking water. *J Am Water Works Assoc*. (1998) 90:18–102. doi: 10.1002/j.1551-8833.1998.tb08465.x
65. Lodhi H, Khan M, Verma R, Sharma U. Acute toxicity of copper sulphate to fresh water prawns. *J Environ Biol*. (2006) 27:585–8.
66. Dave G. Effects of copper on growth, reproduction, survival and haemoglobin in Daphnia magna. *Comp Biochem Physiol Part C Comp Pharmacol*. (1984) 78:439–43. doi: 10.1016/0742-8413(84)90112-9
67. Ezeonyejiaku CD, Obiakor MO, Ezenwelu C. Toxicity of copper sulphate and behavioral locomotor response of tilapia (*Oreochromis niloticus*) and. *Online J Anim Feed Res*. (2011) 1:130–4.

Conflict of Interest: The authors declare that the research was conducted in the absence of any commercial or financial relationships that could be construed as a potential conflict of interest.

Publisher's Note: All claims expressed in this article are solely those of the authors and do not necessarily represent those of their affiliated organizations, or those of the publisher, the editors and the reviewers. Any product that may be evaluated in this article, or claim that may be made by its manufacturer, is not guaranteed or endorsed by the publisher.

frontiers in Veterinary Science

BRIEF RESEARCH REPORT
published: 24 August 2021
doi: 10.3389/fvets.2021.695466

Structure, Antigenic Properties, and Highly Efficient Assembly of PCV4 Capsid Protein

*Dongliang Wang†, Jinhui Mai†, Bo Lei, Yingjie Zhang, Yi Yang and Naidong Wang**

Hunan Provincial Key Laboratory of Protein Engineering in Animal Vaccines, Laboratory of Functional Proteomics, Research Center of Reverse Vaccinology, College of Veterinary Medicine, Hunan Agricultural University, Changsha, China

Porcine circovirus type 4 (PCV4), a recently reported circovirus, was first identified in pigs with clinical signs similar to porcine dermatitis nephropathy syndrome (PDNS), in Hunan province, China, in 2019. More knowledge regarding the assembly of capsid protein (Cap) into virus-like particles (VLPs), their structure and antigenic properties, are needed to provide new knowledge for diagnosis and further characterization of PCV4. In this study, high-level expression of PCV4 Cap was achieved in *Escherichia coli* with purified Cap self-assembling into VLPs (∼20 nm) *in vitro*. Furthermore, these VLPs were internalized *in vitro* by PK15 and 3D4/21 cell lines. Significant structural differences between PCV4 and PCV2 capsids were demonstrated among loops (loop BC, CD, DE, EF, and GH), based on comparisons of 3D structures. In addition, five potential B cell epitopes identified *in silico* were mostly located in surface-exposed loops of PCV4 capsid. Cross-reaction between PCV4 and PCV2 or PCV3 conferred by humoral immune responses was deemed unlikely on the basis of ELISA and Western blotting for assessment of VLPs and using PCV4 or PCV2 VLPs. In conclusion, these studies provided new knowledge regarding PCV4 capsid surface patterns. It is noteworthy that the PCV4 VLPs prepared in our study have much potential for development of serological diagnostics for PCV4 and to further characterize this virus.

Keywords: PCV4, Cap, VLPs, vaccine, serological diagnosis

OPEN ACCESS

Edited by:
Gerson Nakazato, State University of Londrina, Brazil

Reviewed by:
Kegong Tian, National Research Center for Veterinary Medicine, China
Faten A. Okda, St. Jude Children's Research Hospital, United States
Yong Huang, Northwest A and F University, China

***Correspondence:**
Naidong Wang
naidongwang@hunau.edu.cn

†These authors have contributed equally to this work

Specialty section:
This article was submitted to Veterinary Infectious Diseases, a section of the journal Frontiers in Veterinary Science

Received: *15 April 2021*
Accepted: *28 July 2021*
Published: *24 August 2021*

Citation:
Wang D, Mai J, Lei B, Zhang Y, Yang Y and Wang N (2021) Structure, Antigenic Properties, and Highly Efficient Assembly of PCV4 Capsid Protein. Front. Vet. Sci. 8:695466. doi: 10.3389/fvets.2021.695466

INTRODUCTION

Porcine circoviruses (PCVs) are small, spherical, non-enveloped viruses composed of circular, single-stranded genomic DNA within an icosahedral capsid. These viruses belong to the genus *Circovirus* in the family Circoviridae. PCVs have high genetic variability, with four known genotypes: PCV1, PCV2, PCV3, and a novel PCV4 genotype. Although PCV1 is considered non-pathogenic, PCV2 is the causal agent of PCV2-associated diseases (PCVADs). PCV3, first identified in 2016 by metagenomic sequencing (1), is associated with porcine dermatitis nephropathy syndrome (PDNS), cardiac disease, reproductive failure, respiratory disease, etc. (1–3).

In 2019, a newly emerging PCV4 genotype was first identified in serum samples from pigs with respiratory and enteric signs as well as PDNS, in Hunan, China (4). PCV4 is suspected to be associated with these clinical signs, which also occur in pigs infected with PCV2 or PCV3 (1). Subsequently, PCV4 infections causing clinical signs in swine were reported in Henan, Shanxi, Jiangsu, Anhui, and Guangxi provinces, China (5–8), with PCV4-positive rates ranging from 5.1% (13/257) to 25.4% (16/63). Recently, PCV4 has also been detected on swine farms in Korea (9). As

distribution, epidemiology, and pathogenicity (or putative disease association) of PCV4 have not been elucidated, there is an urgent need to characterize this virus.

The genome of PCV4 is ∼1.7 kb long and contains two major open reading frames (ORFs). Whereas, ORF1 encodes replication protein (Rep) involved in virus replication, ORF2 encodes the capsid protein (Cap), the sole structural protein of this virus, capable of inducing neutralizing antibodies and representing a major target for vaccine design and serological diagnosis. In the absence of an efficient method of culturing PCV4, virus-like particles (VLPs) derived from genetic and protein engineering are considered a powerful model to investigate capsid assembly, tissue tropism, and pathogenesis and, in particular, develop effective serological diagnostics for PCV4 (to clarify its incidence). In this study, structure and antigenic properties of PCV4 Cap were analyzed, and expressed PCV4 Cap protein self-assembled into VLPs in an *Escherichia coli* expression system *in vitro*. These results should promote development of effective serological diagnostics for PCV4 and increase understanding of this virus.

METHODS

PCV4 Cap Protein Expression and Purification

A full-length PCV4 *cap* gene was codon optimized and synthesized by the GenScript Company (Nanjing, China) based on the PCV4-AHG-2019 genome sequence (GenBank accession number: MK986820). This gene was cloned into *Nde*I and *BamH*I restriction sites of the pET28a expression vector and the recombinant plasmid confirmed by DNA sequencing. To express recombinant protein, this plasmid was transformed into *E. coli* BL21 (DE3) competent cells (Biomed, Beijing, China) according to the instructions of the manufacturer. Subsequently, a single colony was selected and grown in LB medium (containing 50 μg/ml kanamycin) to an OD_{600} value reaching 0.6–0.8 before a final concentration of 0.5 mM IPTG was added to induce protein expression. After being induced, cells were grown at 25°C for 10 h, harvested, and soluble protein was purified by Ni-NTA affinity chromatography, as described (10). An *E. coli* BL21(DE3) cell pellet was placed into lysis buffer (100 mM $NaH_2PO_4{\cdot}2H_2O$, 50 mM imidazole, 10 mM Tris-HCl, 300 mM NaCl, and 100 mM KCl, pH 8.5) with 0.5 % Triton X-100, and 5 mM β-mercaptoethanol. Then, cells were disrupted by sonication (35% amplitude for 20 min), after which the homogenate was cleared by centrifugation (15,000 × g for 30 min). The supernatant was loaded on a prepacked HisTrap™ HP column (GE Healthcare Life Sciences, New York, NY, USA) according to the instructions of the manufacturer. The column was washed with wash buffer (50 mM $NaH_2PO_4{\cdot}2H_2O$, 50 mM imidazole, and 300 mM NaCl, pH 8.0), and PCV4 Cap was eluted with elution buffer (50 mM $NaH_2PO_4{\cdot}2H_2O$, 200 mM imidazole, and 300 mM NaCl, pH 8.0). Purified proteins were analyzed with SDS-PAGE and Western blot using mouse anti-6 × His tag antibody (1:3,000; Solarbio, Beijing, China) or mouse anti-PCV4 Cap serum (1:1,000).

PCV4 VLPs Assembly and Transmission Electron Microscopy

Purified PCV4 Cap was dialyzed against phosphate-buffered saline (PBS) buffer (pH 7.4) for 48 h. The PCV4 VLPs were absorbed into carbon-coated copper grids for 10 min, stained with 1% phosphotungstic acid for 5 min, and imaged using TEM (CM100, Philips Electron Optics, Switzerland).

Preparation of Anti-PCV4 and PCV2 Cap Serum

PCV2 VLPs were prepared as described (10). Female BALB/c mice ($n = 4$/group, 6 weeks old) were used to prepare anti-PCV4 and PCV2 Cap sera. Each mouse was initially immunized with 20 μg of PCV4 or PCV2 VLPs mixed with Freund's complete adjuvant (final volume, 0.2 ml). Booster immunizations using the same amount of VLPs mixed with Freund's incomplete adjuvant were done twice at 2-week intervals (weeks 2 and 4). Blood samples were collected 6 weeks after primary immunization, and sera were collected and stored at −20°C.

Immunofluorescence Staining of PCV4 VLPs

Two porcine cell lines (PK15 and 3D4/21) were used to detect cell entry of PCV4 VLPs. Cells cultured in 48-well plates were incubated with 2 μg of PCV4 VLPs in each well, with DMEM, in lieu of VLPs, added to cells as a control. After incubation for 1 h, cells were washed three times with PBST (containing 0.1% Tween 20). Subsequently, cell entry of PCV4 VLPs was detected with an indirect immunofluorescence assay (IFA), as described (11). Anti-PCV4 Cap mouse serum (1:1,000) was used as the primary antibody, and immunostained slides were examined with fluorescence microscopy (Olympus BX-51, Tokyo, Japan).

Enzyme-Linked Immunosorbent Assay

Sera of mice immunized with PCV2 and PCV4 VLPs were assessed using our established indirect ELISA, as described (10). Secondary antibody was horseradish peroxidase (HRP)-labeled goat anti-mouse IgG (Thermo Fisher Scientific, Shanghai, China). Optical densities were read at 450 nm.

Bioinformatics Analyses

All PCVs Cap sequences in the NCBI GenBank database (http://www.ncbi.nlm.nih.gov/) were retrieved. Amino acid sequences were aligned using the ESPript 3.0 online tool (http://espript.ibcp.fr/ESPript/ESPript/). The 3D structure homology modeling was reconstructed based on PCV2 Cap protein structure (Protein Data Bank (PDB) ID: 3R0R) in SWISS-MODEL (https://swissmodel.expasy.org/) and displayed with Pymol 1.8.0.3. Linear B cell epitopes of PCV4 Cap protein were predicted by BepiPred 2.0 online tool (http://www.iedb.org/) with a default threshold of 0.5. Antigenicity was evaluated with the Vaxijen v2.0 server online tool (http://www.ddg-pharmfac.net/vaxijen/VaxiJen/VaxiJen.html).

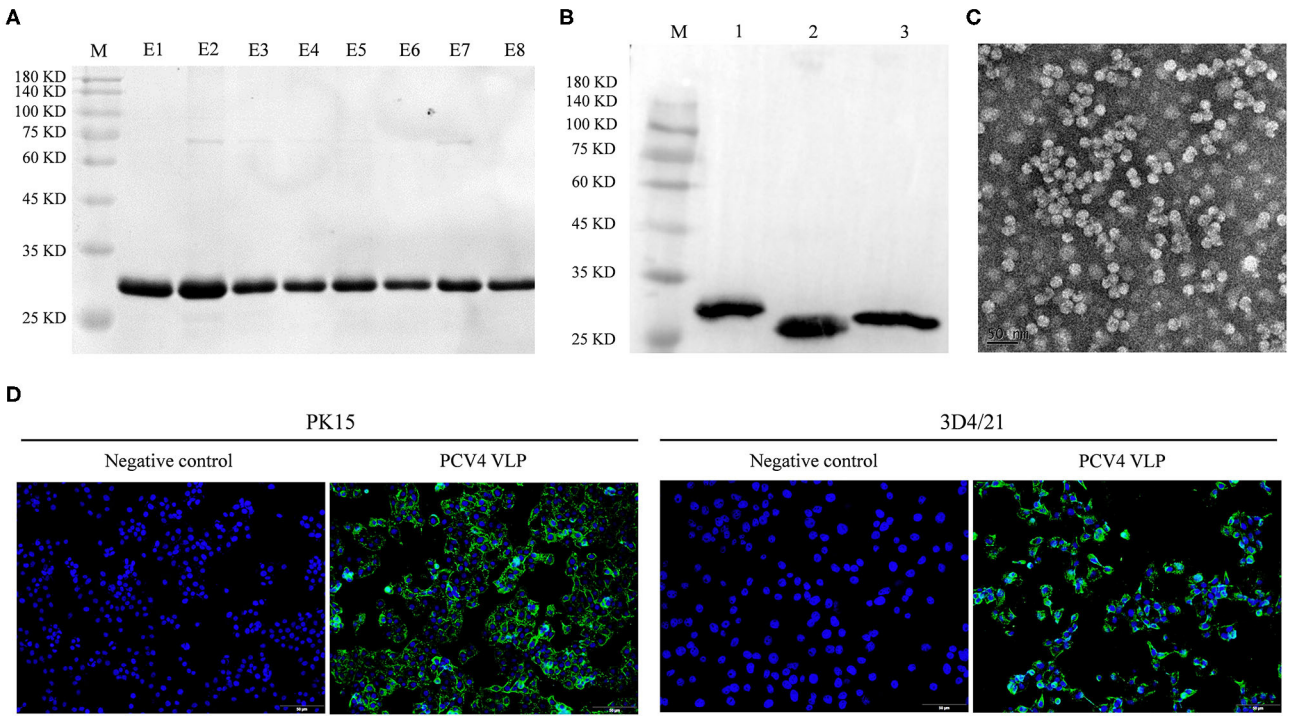

FIGURE 1 | (A) Coomassie blue-stained SDS-PAGE of purified PCV4 Cap protein (lane M: protein marker; lanes E1–E8: purified PCV4 Cap protein). **(B)** Western blots of PCV Cap proteins using mouse anti-6 × His tag antibody (lane M: protein marker; lane 1: PCV4 Cap; lane 2: PCV3 Cap; and lane 3: PCV2 Cap). **(C)** Formation of PCV4 VLPs observed with TEM. **(D)** Entry of PCV4 VLPs into PK15 and 3D4/21 cell lines was confirmed by fluorescence microscopy. Green fluorescence represents PCV4 Cap in cells, whereas cell nuclei (blue) were stained by DAPI.

RESULTS

Expression and Purification of Recombinant PCV4 Cap

The full length of the optimized *cap* gene was cloned into a pET28a expressed vector with a 6 × His tag fused at the NH_2 terminus of the PCV4 Cap protein to aid purification. The PCV4 Cap was successfully expressed in bacteria. Furthermore, the soluble Cap was purified with Ni-NTA affinity chromatography. The purified Cap, analyzed by SDS-PAGE, had an apparent molecular weight of ∼28 kDa (**Figure 1A**) and was recognized by anti-His tag antibody in a Western blot (**Figure 1B**).

PCV4 VLPs Self-Assembly From the Cap *in vitro*

Purified PCV4 Cap protein was dialyzed against PBS buffer (pH 7.4) to facilitate *in vitro* assembly of VLPs. Spherical morphology (diameter, ∼20 nm) was observed under TEM, confirming formation of PCV4 VLPs (**Figure 1C**). Therefore, the Cap self-assembled into VLPs *in vitro*.

Entry of PCV4 VLPs Into Cells

Two porcine cell lines (PK15 and 3D4/21) were used to test internalization of PCV4 VLPs into cells *in vitro*. Based on IFA, PCV4 VLPs entered both PK15 and 3D4/21 cells (**Figure 1D**).

Analysis of PCV4 Capsid Structure and Predicted Immune Epitopes

The PCV Cap has a canonical jelly roll fold; however, Cap sequence variations among various circovirus isolates have minimal effect on the jelly roll structure. Similar to PCV2 Cap structures, a viral jelly roll structure was also observed in the PCV4 Cap (**Figure 2A**), based on homology modeling using a crystal structure of PCV2 Cap as a template. Based on Cap sequence alignment, most variable residues between PCV2 and PCV4 Caps were located within the surface-exposed loops, especially the icosahedral five-fold axes composed of loops BC, DE, and HI (**Figures 2A**, **3A**). Compared to the PCV2 Cap, loops BC, CD, DE, EF, and GH were distinctly different between PCV2 and PCV4 (**Figure 2B**).

In the PCV4 Cap, five potential linear B cell epitopes with high antigenicity were predicted by BepiPred 2.0 based on default threshold, as indicated with various colors in the three-dimensional (3D) structure (**Figure 2C**). Notably, these five potential epitopes were all located in loops and mapped to the most exposed surface regions of the PCV4 capsid (**Figures 2D**, **3A**). In-depth sequence analysis revealed the five B-cell epitopes

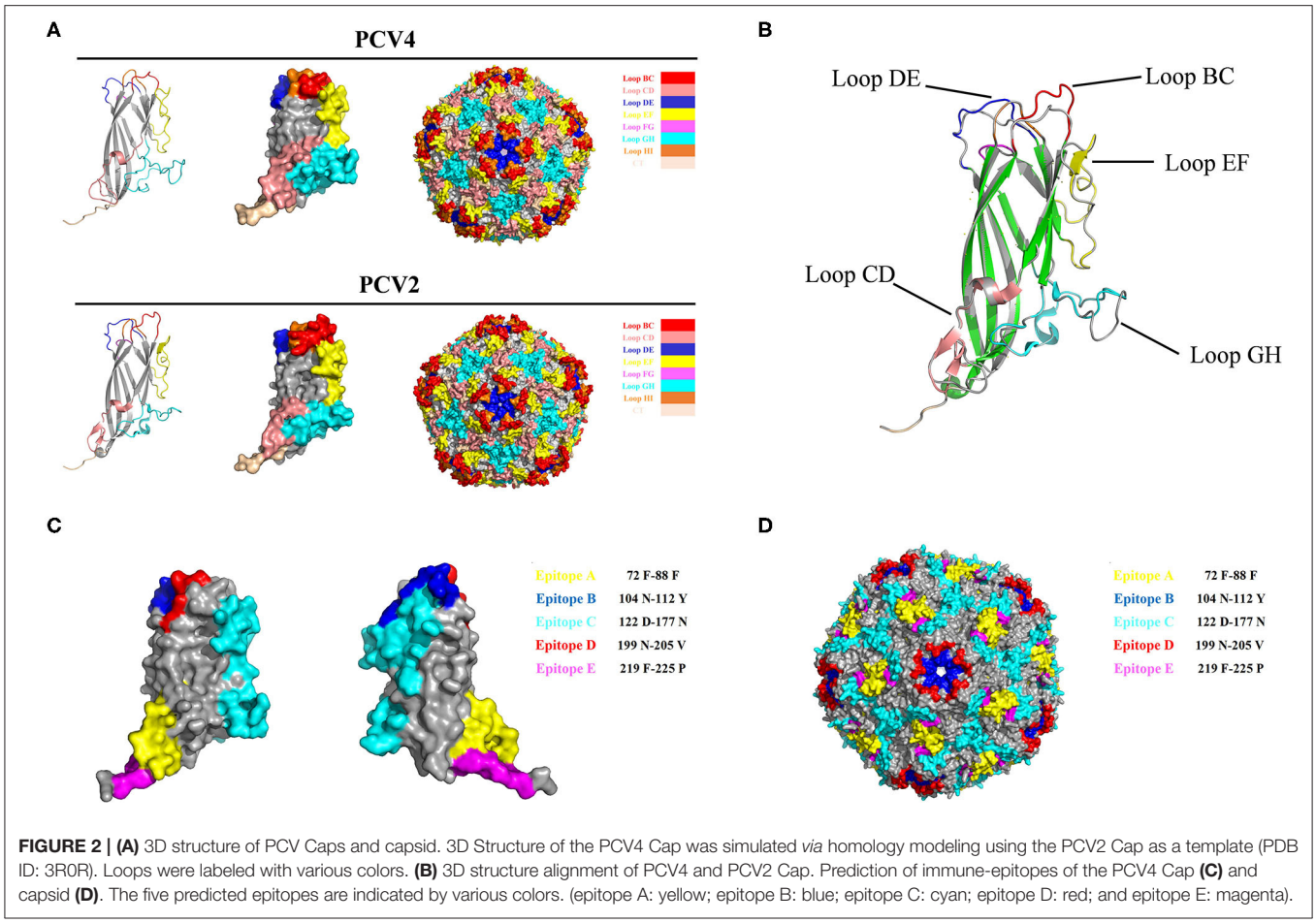

FIGURE 2 | (A) 3D structure of PCV Caps and capsid. 3D Structure of the PCV4 Cap was simulated *via* homology modeling using the PCV2 Cap as a template (PDB ID: 3R0R). Loops were labeled with various colors. **(B)** 3D structure alignment of PCV4 and PCV2 Cap. Prediction of immune-epitopes of the PCV4 Cap **(C)** and capsid **(D)**. The five predicted epitopes are indicated by various colors. (epitope A: yellow; epitope B: blue; epitope C: cyan; epitope D: red; and epitope E: magenta).

of the PCV4 Cap shared less residue identity with either PCV2 or PCV3 Cap (**Figure 3**).

Cross-Reactions Between PCV4 and PCV2 or PCV3 Cap

PCV2 VLPs with a diameter of ∼20 nm were successfully obtained (**Supplementary Figure 1**). Cross-reactions of anti-PCV4 or anti-PCV2 IgG from mouse serum collected 6 weeks after the primary immunization with PCV4 or PCV2 VLPs, respectively, were determined by ELISA. Sera from PCV4-immunized mice did not react with PCV2 VLP, and *vice versa*, whereas sera from PCV2-immunized mice did not react with PCV4 VLP (**Figures 4A,B**; **Supplementary Table 1**). Therefore, PCV4 immunization induced genotype-specific antibody profiles in mice. Anti-PCV4 IgG had limited cross-reaction with PCV2; furthermore, antibodies elicited by the PCV2 Cap did not react with PCV4.

Next, anti-PCV4 Cap serum was used for detecting cross-reactions with PCV2 or PCV3 Cap by Western blot, with anti-His tag antibody used as a positive control. The three PCV Caps positively reacted with anti-His tag antibody (**Figure 1B**). However, anti-PCV4 Cap serum recognized only the PCV4 Cap, but neither PCV2 nor PCV3 Cap (**Figure 4C**). In addition, anti-PCV2 Cap serum only reacted with PCV2 Cap, but neither PCV3 nor PCV4 Caps (**Figure 4D**). This lack of cross-reactions was attributed to the low residue identity among these Caps.

DISCUSSION

PCV4, a newly emerging porcine circovirus, has been identified in pigs with severe clinical disease, including PDNS-like clinical signs, diarrhea, and respiratory disease (4, 8). However, there is very limited information about its epidemiology, origin, evolution, pathogenesis, and transmission in swine herds. Notably, PCV4 has been detected as coinfections with PCV2, PCV3, or both (6–8). As PCV4 may be a serious risk for swine health, a better understanding of PCV4 pathogenesis, its epidemiology, and serological surveys to determine its prevalence is urgently needed.

VLPs are morphologically and immunogenically similar to their native viruses; furthermore, because of their ability to induce strong immune responses, they are widely used for novel vaccine design and serological diagnosis (12). Cap is the major structural protein of PCVs, and 60 Cap monomers self-assembled into VLPs *in vitro* (13, 14). The N-terminal nuclear location signal (NLS) domain of the Cap is abundant in arginine residues and contains several rare codons that limit gene expression

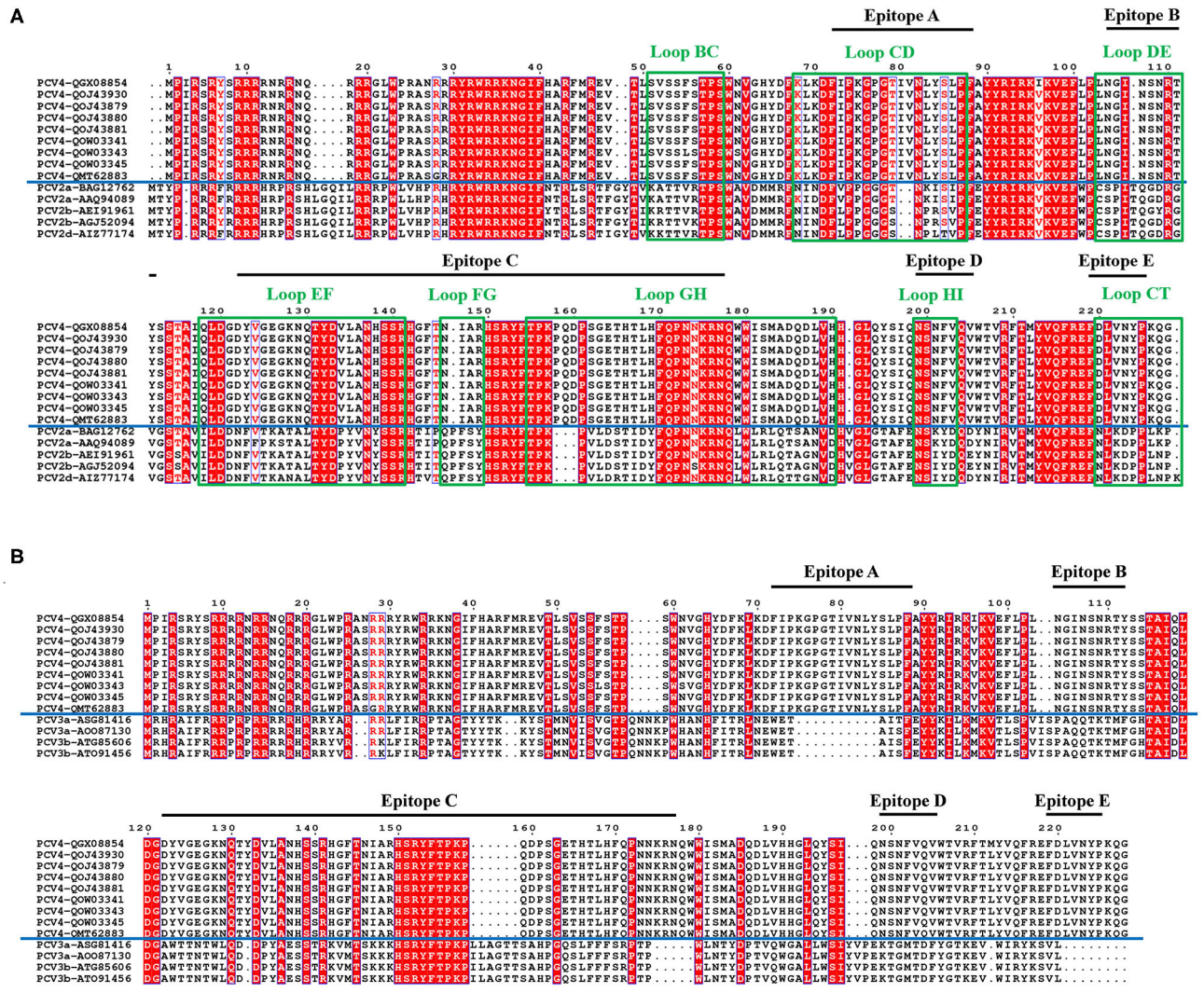

FIGURE 3 | Sequence alignment of PCV Caps. Comparative amino acid sequence alignments between PCV4 and PCV2 Cap **(A)** or PCV4 and PCV3 Cap **(B)**. All loops labeled with green rectangles and black lines represent predicted PCV4 potential linear B cell epitopes.

in *E. coli*. In this study, a full-length PCV4 Cap protein via codon optimization was highly expressed in an inexpensive *E. coli* expression system. Purified Cap self-assembled into VLPs (∼20 nm) *in vitro* with high yields. To characterize entry of PCV4 VLPs into cells, two porcine cell lines were used. As expected, PCV4 VLPs were capable of entering PK15 and 3D4/21 cells. Furthermore, PCV4 VLP-specific mouse serum recognized the PCV4 Cap prepared from the expression system. Therefore, PCV4 VLPs produced in *E. coli* were antigenic and well suited for future serological diagnostics and vaccine development.

We further analyzed the surface structure of PCV4 VLPs (capsid) and made comparisons to PCV2. Sequence alignment, together with 3D structure simulation, indicated substantial variation between PCV2 and PCV4 capsids in surface-exposed loop regions and surface patterns formed by various loops, although their whole structures were similar. In particular, the surface of the icosahedral five-fold axes constituted by loops BC, DE, and HI differed, as residues of these loopanalyzed the surface structures were highly divergent between PCV2 and PCV4 Caps (**Figure 3A**). In the PCV2 capsid, the structure of the five-fold axes was involved in conformational epitope formation. PCV2 neutralizing antibody bound to the residues around the surface of the five-fold symmetry axes, and this antibody recognized two adjacent capsid proteins as conformational epitopes (15). Diversity of the five-fold axes provided insights into antigenic differences between PCV2 and PCV4. Furthermore, these results highlighted differential structural and antigenic properties of PCV2 and PCV4 capsid proteins.

Interestingly, PCV4 Cap had high identity (70%) with the Cap of mink circovirus (4). However, it had low identities (∼45 and 25%) with PCV2 and PCV3 Caps, respectively, whereas cross-reaction with PCV2 or PCV3 is unknown. To explore whether PCV4 cross-reacts with PCV2 or PCV3, anti-PCV4 Cap serum in BALB/c mice elicited by immunization with the PCV4 VLPs was

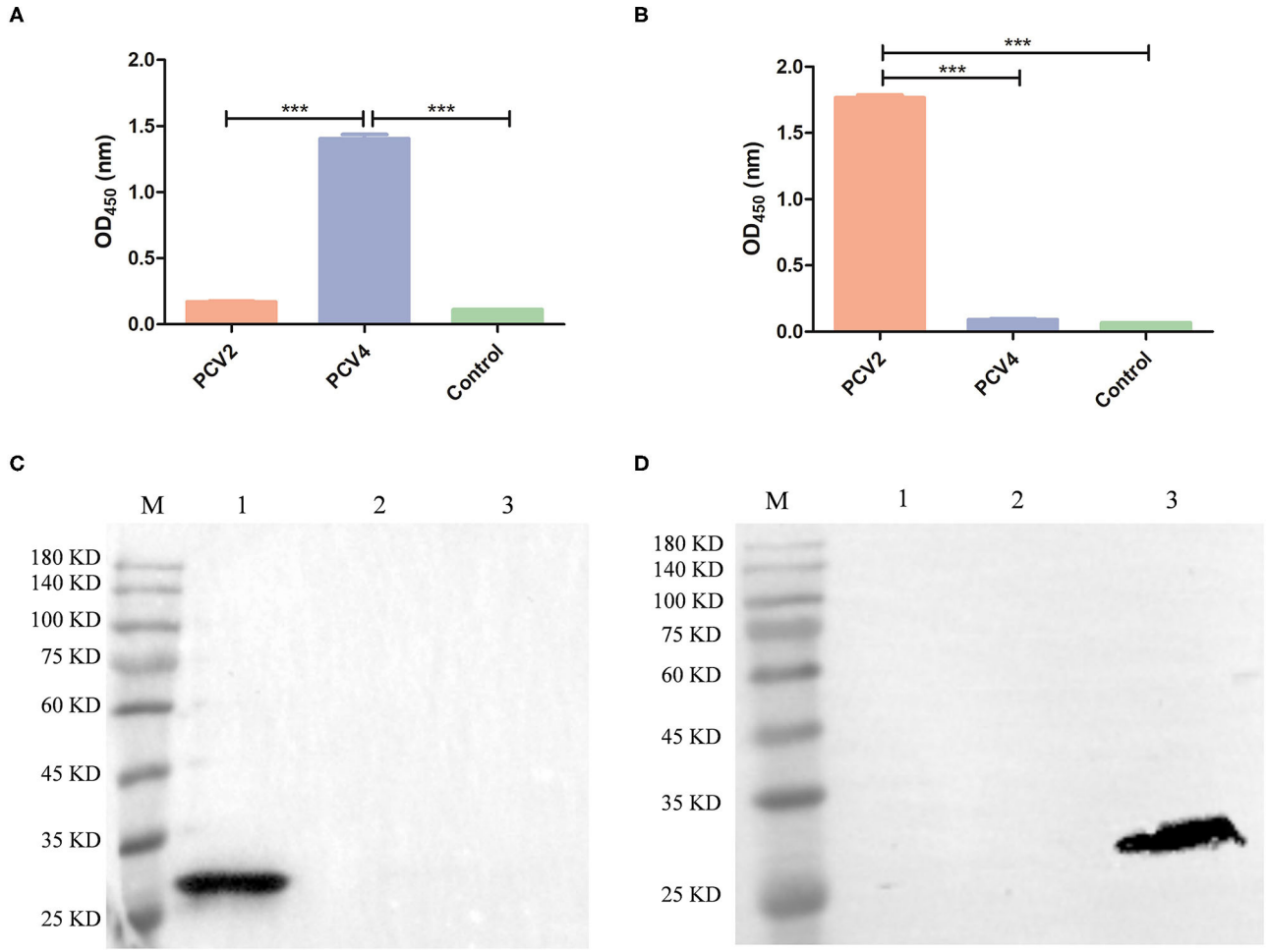

FIGURE 4 | Cross-reaction between PCV4 and PCV2 by ELISA and Western blots. The reactivity of PCV4 VLP-immunized **(A)** or PCV2 VLP-immunized **(B)** mouse serum ($n = 4$) with PCV4 or PCV2 by ELISA. Reactivity of sera from PCV4 or PCV2 VLP-immunized mice, collected 6 weeks after initial immunization. Immunized mice ($n = 2$) received PBS as a control. Optical densities were read at 450 nm. ***$p < 0.001$. **(C,D)** Western blots of PCV Cap proteins using anti-PCV4 Cap serum or anti-PCV2 Cap serum, respectively (lane M: protein marker; lane 1: PCV4 Cap; lane 2: PCV3 Cap; and lane 3: PCV2 Cap).

used to detect cross-reaction with PCV2 or PCV3 Caps. Based on Western blot, only PCV4 Cap was recognized by anti-PCV4 Cap serum. Apparently, only PCV4 VLPs induced genotype-specific antibodies in mice. Moreover, the predicted PCV4 immune epitopes had very low identity to PCV2 or PCV3 Cap, which can further explain the absence of cross-reactions to the two Caps. Thus, cross-reaction between these Caps is unlikely, consistent with the result of the Western blot (**Figure 4C**). In parallel, anti-PCV2 Cap serum (produced by immunization with PCV2 VLPs) was used in Western blots to detect cross-reactions with PCV3 or PCV4 Cap; as expected, only the PCV2 Cap was specifically recognized by the anti-PCV2 Cap serum. Furthermore, using ELISA, we confirmed there was limited cross-reaction between PCV4 and PCV2. Therefore, we inferred that elicited antibody responses were unlikely to cross-protect between PCV4 and either PCV2 or PCV3.

CONCLUSION

We successfully expressed the PCV4 Cap and confirmed it was capable of self-assembling into VLPs *in vitro* with a diameter of ~20 nm. To our knowledge, this is the first report of PCV4 VLPs prepared from an *E. coli* expression system. The PCV4 VLPs produced in the present study had high antigenicity, with much potential for future serological diagnostics. Importantly, cross-reactions between PCV4 and either PCV2 or PCV3 were unlikely. Finally, these PCV4 VLPs are expected to be a valuable tool to study PCV4.

DATA AVAILABILITY STATEMENT

The raw data supporting the conclusions of this article will be made available by the authors, without undue reservation.

ETHICS STATEMENT

The animal study was reviewed and approved by the Animal Ethics Committee of Hunan Agricultural University, Hunan, China.

AUTHOR CONTRIBUTIONS

NW and DW conceived and designed the experiments. DW and JM performed the generation, characterization of the PCV4 VLPs, designed, and carried out the immunoassays and bioinformatics analysis. BL and YZ prepared anti-PCV4 and PCV2 Cap serum from mouse. DW, YY, and NW wrote and revised the manuscript. All authors read and approved the final manuscript.

FUNDING

This research was funded by Hunan Provincial Natural Science Foundation of China, Grant Number 2018JJ2177; double first-class construction project of Hunan Agricultural University, Grant Number SYL2019048; and Post-graduate Research and Innovation Project of Hunan Province, Grant Number CX2018B394.

SUPPLEMENTARY MATERIAL

The Supplementary Material for this article can be found online at: https://www.frontiersin.org/articles/10.3389/fvets.2021.695466/full#supplementary-material

REFERENCES

1. Palinski R, Piñeyro P, Shang P, Yuan F, Guo R, Fang Y, et al. A novel porcine circovirus distantly related to known circoviruses is associated with porcine dermatitis and nephropathy syndrome and reproductive failure. *J Virol*. (2017) 91:e01879–16. doi: 10.1128/JVI.01879-16
2. Phan TG, Giannitti F, Rossow S, Marthaler D, Knutson TP, Li L, et al. Detection of a novel circovirus PCV3 in pigs with cardiac and multi-systemic inflammation. *Virol J*. (2016) 13:184. doi: 10.1186/s12985-016-0642-z
3. Jiang H, Wang D, Wang J, Zhu S, She R, Ren X, et al. Induction of porcine dermatitis and nephropathy syndrome in piglets by infection with porcine circovirus type 3. *J Virol*. (2019) 93:e02045–18. doi: 10.1128/JVI.02045-18
4. Zhang HH, Hu WQ, Li JY, Liu TN, Zhou JY, Opriessnig T, et al. Novel circovirus species identified in farmed pigs designated as Porcine circovirus 4, Hunan province, China. *Transbound Emerg Dis*. (2020) 67:1057–61. doi: 10.1111/tbed.13446
5. Tian RB, Zhao Y, Cui JT, Zheng HH, Xu T, Hou CY, et al. Molecular detection and phylogenetic analysis of Porcine circovirus 4 in Henan and Shanxi Provinces of China. *Transbound Emerg Dis*. (2021) 68:276–82. doi: 10.1111/tbed.13714
6. Zhang D, Bai C, Ge K, Li Y, Gao W, Jiang S, et al. Establishment of an SYBR Green-based real-time PCR assay for porcine circovirus type 4 detection. *J Virol Methods*. (2020) 285:113963. doi: 10.1016/j.jviromet.2020.113963
7. Chen N, Xiao Y, Li X, Li S, Xie N, Yan X, et al. Development and application of a quadruplex real-time PCR assay for differential detection of porcine circoviruses (PCV1 to PCV4) in Jiangsu province of China from 2016 to 2020. *Transbound Emerg Dis*. (2021) 68:1615–24. doi: 10.1111/tbed.13833
8. Sun W, Du Q, Han Z, Bi J, Lan T, Wang W, Zheng M. Detection and genetic characterization of porcine circovirus 4 (PCV4) in Guangxi, China. *Gene*. (2021) 773:145384. doi: 10.1016/j.gene.2020.145384
9. Nguyen VG, Do HQ, Huynh TM, Park YH, Park BK, Chung HC. Molecular based detection, genetic characterization and phylogenetic analysis of porcine circovirus 4 from Korean domestic swine farms. *Transbound Emerg Dis*. (2021). doi: 10.1111/tbed.14017. [Epub ahead of print].
10. Zhang Y, Wang Z, Zhan Y, Gong Q, Yu W, Deng Z, et al. Generation of E. coli-derived virus-like particles of porcine circovirus type 2 and their use in an indirect IgG enzyme-linked immunosorbent assay. *Arch Virol*. (2016) 161:1485–91. doi: 10.1007/s00705-016-2816-9
11. Wang D, Zhang S, Zou Y, Yu W, Jiang Y, Zhan Y, et al. Structure-based design of porcine circovirus type 2 chimeric VLPs (cVLPs) displays foreign peptides on the capsid surface. *Front Cell Infect Microbiol*. (2018) 8:232. doi: 10.3389/fcimb.2018.00232
12. Yan D, Wei YQ, Guo HC, Sun SQ. The application of virus-like particles as vaccines and biological vehicles. *Appl Microbiol Biotechnol*. (2015) 99:10415–32. doi: 10.1007/s00253-015-7000-8
13. Khayat R, Brunn N, Speir JA, Hardham JM, Ankenbauer RG, Schneemann A, et al. The 2.3-angstrom structure of porcine circovirus 2. *J Virol*. (2011) 85:7856–62. doi: 10.1128/JVI.00737-11
14. Wang N, Zhan Y, Wang A, Zhang L, Khayat R, Yang Y. *In silico* analysis of surface structure variation of PCV2 capsid resulting from loop mutations of its capsid protein (Cap). *J Gen Virol*. (2016) 97:3331–44. doi: 10.1099/jgv.0.000634
15. Huang L, Sun Z, Xia D, Wei Y, Sun E, Liu C, et al. Neutralization mechanism of a monoclonal antibody targeting a porcine circovirus type 2 cap protein conformational epitope. *J Virol*. (2020) 94:e01836–19. doi: 10.1128/JVI.01836-19

Conflict of Interest: The authors declare that the research was conducted in the absence of any commercial or financial relationships that could be construed as a potential conflict of interest.

Publisher's Note: All claims expressed in this article are solely those of the authors and do not necessarily represent those of their affiliated organizations, or those of the publisher, the editors and the reviewers. Any product that may be evaluated in this article, or claim that may be made by its manufacturer, is not guaranteed or endorsed by the publisher.

frontiers in Veterinary Science

ORIGINAL RESEARCH
published: 03 December 2021
doi: 10.3389/fvets.2021.771341

Lateral Flow Immunoassay for Visible Detection of Human Brucellosis Based on Blue Silica Nanoparticles

Lirui Ge[1,2], *Dan Wang*[1,2], *Fengnan Lian*[1,2], *Jinbin Zhao*[1,2], *Yue Wang*[1,2], *Yuyi Zhao*[1,2], *Lanting Zhang*[1], *Juan Wang*[1], *Xiuling Song*[1], *Jinhua Li*[1]* and *Kun Xu*[1,2]*

[1] School of Public Health, Jilin University, Changchun, China, [2] Public Health Detection Engineering Research Center of Jilin Province, Changchun, China

OPEN ACCESS

Edited by:
Renata Katsuko Takayama Kobayashi, State University of Londrina, Brazil

Reviewed by:
Francesca Paola Nocera, Università degli Studi di Napoli Federico II, Italy
Aman Ullah Khan, University of Veterinary and Animal Sciences, Pakistan

***Correspondence:**
Kun Xu
xukun@jlu.edu.cn
Jinhua Li
jinhua1@jlu.edu.cn

Specialty section:
This article was submitted to Veterinary Infectious Diseases, a section of the journal Frontiers in Veterinary Science

Received: 06 September 2021
Accepted: 27 October 2021
Published: 03 December 2021

Citation:
Ge L, Wang D, Lian F, Zhao J, Wang Y, Zhao Y, Zhang L, Wang J, Song X, Li J and Xu K (2021) Lateral Flow Immunoassay for Visible Detection of Human Brucellosis Based on Blue Silica Nanoparticles. Front. Vet. Sci. 8:771341. doi: 10.3389/fvets.2021.771341

Brucellosis is a highly contagious zoonosis chronic infectious disease with a strong latent capability to endanger human health and economic development *via* direct or indirect ways. However, the existing methods for brucellosis diagnosis are time-consuming and expensive as they require a tedious experimental procedure and a sophisticated experimental device and performance. To overcome these defects, it is truly necessary to establish a real-time, on-site, and rapid detection method for human brucellosis. Here, a lateral flow immunoassay (LFIA) with a rapid, sensitive, and alternative diagnostic procedure for human brucellosis with a high degree of accuracy was developed based on blue silica nanoparticles (SiNPs), *Staphylococcal* protein A (SPA), and surface Lipopolysaccharide of *Brucella* spp. (LPS), which can be applied for rapid and feasible detection of human brucellosis. To our knowledge, this is the first report that uses blue SiNPs as a signal probe of LFIA for the rapid diagnosis of human brucellosis. The precursor of blue SiNPs@SPA such as colorless SiNPs and blue SiNPs was synthesized at first and then coupled with SPA onto the surface of blue SiNPs by covalent bond to prepare blue SiNPs@SPA as a capture signal to catch the antibody in the brucellosis-positive serum. When SPA was combined with the antibodies in the brucellosis-positive serum, it was captured by LPS on the test line, forming an antigen–antibody sandwich structure, resulting in the T line turning blue. Finally, the results showed that it is acceptable to use blue SiNPs as visible labels of LFIA, and standard brucellosis serum (containing *Brucella* spp. antibody at 1,000 IU/ml) could be detected at a dilution of 10^{-5} and the detection limit of this method was 0.01 IU/ml. Moreover, it also demonstrated good specificity and accuracy for the detection of real human serum samples. Above all, the blue SiNPs-based LFIA that we developed provides a rapid, highly accurate, and inexpensive on-site diagnosis of human brucellosis, and shows great promise in clinical diagnostics for other diseases.

Keywords: blue SiNPs, LFIA, human brucellosis, antigen-antibody sandwich structure, *Brucella* spp.

INTRODUCTION

A lateral flow immunoassay (LFIA) is a fast, simple, and economic method that is widely used in the field of rapid detection of various analytes. The labels used for LFIA include a series of particles, such as quantum dots (1, 2), latex beads (3), colloidal gold, and magnetic particles (4). Among the above particles, colloidal gold was the most commonly used label for LFIA, which was widely applied in bacteria detection and drug testing. However, the performance of colloidal gold depends on the amounts of molecules gathered. Thus, it is susceptible to optical interference, which always exhibits relatively low sensitivity and inaccurate qualitative or semi-quantitative results (5). Meanwhile, the performance of colloidal gold is often affected by temperature, pH, and salt concentration. Moreover, the use of colloidal gold in multiple tests is also limited as colloidal gold always displays a single color (6). Quantum dots and dye-doped nanoparticles are representative fluorescent nanoparticle probes that have attracted increasing research attention (5, 7, 8). Dye-doped nanoparticles vary in diameter from 2 to 200 nm, containing a large quantity of dye molecules embedded in a polymer or silica matrix, which can emit more intense fluorescence signals than organic fluorophores (5, 9). However, the detection of fluorescent dye-doped nanoparticles requires specific equipment for the detection of the fluorescence signal, and the stability of the fluorescent signal still needs further verification. Of note, silica nanoparticles (SiNPs) are widely used in several fields, such as in disease labeling, biosensing, and drug delivery (10). However, most previously used SiNPs are white or colorless, which are not suitable for signal conversion and signal amplification (11). It is known that organic dyes possess good stability and rich color, which would not fade even under harsh conditions. Due to their chemical reactivity, many organic dyes are very suitable for dyeing, such as dyeing colorless SiNPs into colored SiNPs. Besides, the surface of SiNPs is easy to modify, which can be used in catalysis, molecular detection, biological detection, and imaging by doping functional materials (12, 13). Therefore, colored SiNPs not only possess a bright color but also possess four advanced characteristics: a strong covalent interaction between dye and SiNPs, high hydrophilicity and good water dispersion, excellent stability, and easy surface modification (5, 14). These high-quality characteristics indicate that colored SiNPs are good optical nano-labels to amplify the response signal in immunochromatographic strips (15–17).

Brucella spp. is a type of intracellular parasitic and facultative anaerobic Gram-negative short bacilli. According to the different susceptible hosts, *Brucella* spp. can be divided into six classical types, namely, *Brucella abortus*, *Brucella melitensis*, *Brucella ovis*, *Brucella canis*, *Brucella neotomae*, and *Brucella suis* (18). At the beginning of the twenty-first century, several novel species were identified, such as *Brucella pinnipedialis* (isolated from seals) and *Brucella ceti* (isolated from dolphins and whales) (19), as well as *Brucella microti*, which was isolated and identified from wild rats for the first time. Then, a new strain of *B. microti* was isolated from red foxes and soil in 2008 (20), *Brucella inopinata* was isolated from a breast-transplanted patient in 2010 (21), and another new strain of *Brucella* was isolated from frogs in 2012 (22). The discovery of these new *Brucella* spp. reveals that the natural host range of *Brucella* spp. has gradually expanded to non-human primates and amphibians. Among the abovementioned strains, *B. abortus*, *B. melitensis*, *B. neotomae*, and *B. suis* are human pathogenic bacteria, and *B. melitensis* has the strongest pathogenicity. According to the statistics of *B. melitensis* strains isolated from 29 provinces in China from 1950 to 1991, the proportion of *B. melitensis* strain type 1 and type 3 was 53.8 and 33.2%, respectively. However, since 1991, the proportion of type 3 strain has increased to 80% (23). Brucellosis, the disease caused by *Brucella* spp., can be transmitted from infected animals to humans, which brings particular threat to the people engaged in animal husbandry in some rural areas. The data from the World Health Organization demonstrate that brucellosis has affected more than 170 countries or regions in the world, and more than 400,000 new cases were reported every year (24). The main clinical manifestations of brucellosis include wave fever, night sweats, joint pain, abortion, infertility, and easy recurrence. The course of brucellosis varies from 1 month to more than a few years. Therefore, patients with brucellosis will face great economic burden and mental problems if they cannot be diagnosed or treated in time. On the contrary, most patients with brucellosis will recover within 3–6 months if brucellosis can be diagnosed in time. At present, the detection technology for brucellosis, such as bacterial culture and PCR, usually requires a relatively long time, high cost, expensive equipment, and complex operating procedures. However, brucellosis commonly occurs in farms and rural areas with poor facilities. The existing diagnosis technologies for brucellosis require professional testing personnel and equipment, which are not suitable for rural areas. Therefore, it is of great significance to establish a simple, rapid, and inexpensive diagnosis method for brucellosis for early diagnosis and timely treatment.

As little work using blue SiNPs as a reporter of LFIA to detect human brucellosis has been reported, here, an LFIA with a rapid, sensitive, and alternative diagnostic procedure for human brucellosis with a high degree of accuracy was developed based on blue SiNPs, *Staphylococcal* protein A (SPA), and surface lipopolysaccharide of *Brucella* spp. (LPS). At first, the precursor of blue SiNPs such as C.I. Reactive Blue 21 and colorless SiNPs was synthesized, and then C.I. Reactive Blue 21 was introduced onto the surface of colorless SiNPs in a given of amount of coupling substance to prepare blue SiNPs, followed by a layer of silica shell, which was formed by TEOS hydrolysis that was wrapped outside of SiNPs to avoid dye leakage. Afterwards, the amino group, which aims to combine with SPA by covalent bonding, was introduced to the surface of core-shell blue SiNPs *via* 3-aminopropyl triethoxysilane (APTES). After that, glutaraldehyde was used to activate the amino groups on the surface of blue SiNPs, and then SPA was added into above solution to obtain the blue SiNPs@SPA. The blue SiNPs@SPA as capture signal to catch the antibody in the brucellosis-positive serum. When SPA was combined with the antibodies in the brucellosis-positive serum, it was captured by LPS on the test line, forming an antigen–antibody sandwich structure, resulting in the T line turning blue. On this basis, the feasibility of this detection in human serum was also verified. We also discussed the feasibility of this work in human serum, and the results showed that it is acceptable to use blue SiNPs as visible labels

of LFIA to diagnose human brucellosis in standard brucellosis serum and real human serum samples. Above all, a fast, one-step strategy and high-specificity method based on blue SiNPs for the diagnosis of human brucellosis has been developed, which can be applied in developing countries and rural areas.

MATERIALS AND METHODS

Materials and Reagents

SPA and goat anti-mouse IgG were provided by Beijing Bioss Biotechnology Co., Ltd. and (3-Aminopropyl) triethoxysilane (APTES) was provided by Shanghai Aladdin Bio-Chem Technology Co., LTD. Glutaraldehyde was obtained from Sigma-Aldrich (Shanghai, China); bovine serum albumin (BSA) and tetraethyl orthosilicate (TEOS) were obtained from Shanghai Macklin Biochemical Co., Ltd. Anhydrous ethanol was obtained from Tianjin Xinbote Chemistry Co., Ltd. (Tianjin, China). Twenty five percent ammonia was purchased from Xilong Science Co., Ltd. Reagents used in indirect ELISA were purchased from Shanghai Jianglai Biotechnology Co., Ltd; phosphate buffered saline (PBS) buffers (pH 7.4) were obtained from Sangon Biotechnology Co., Ltd. (Shanghai, China). The glass fiber, releasing pad, nitrocellulose membrane, absorbing pad, and polyvinyl chloride sheet were obtained from Shanghai Jinbiao Biotechnology Co., Ltd. (Shanghai, China).

Preparation of Core-Shell Blue SiNPs

Colorless SiNPs were synthesized by the Stöber method with a slight modification. A Stöber system containing 30 ml of anhydrous ethanol, 4 ml of water, and 5 ml of ammonia water was hydrolyzed for 30 min at 60°C. Then, 5 ml of TEOS was added slowly within 30 min, and the reaction continued for another 2 h. The final colorless SiNPs were isolated by centrifugation (7,000 rpm, 5 min) and finally freeze-dried by a Lyophilizer.

Dye-coated SiNPs were prepared by following a previous report with a slight modification (25). Briefly, 100 mg of colorless SiNPs was dissolved in 15 ml of water. After that, 20 μl of APTES and 100 μl (100 mg/ml) of C.I. Reactive Blue 21 aqueous solution were mixed with 15 ml of water, which contained 0.1 g SiNPs and was left to react for 2.5 h. Then, the precipitate was centrifugally collected and washed with ethanol and water.

A Stöber system that contained 10 ml of ethanol, 815 μl of H_2O, 0.2 ml of TEOS, and 0.1 ml of $NH_3 \cdot H_2O$ was hydrolyzed for 20 min, and then 5 ml of the above blue SiNPs was poured into the above solution and reacted for 12 h. After the reaction, the core-shell blue SiNPs were centrifuged and dispersed in pure water.

Preparation of Amino-Modified Core-Shell Blue SiNPs

One hundred milligrams of core-shell blue SiNPs was dissolved in 20 ml of ethanol under ultrasonic conditions at room temperature for 30 min. After that, the above prepared core-shell blue SiNPs were transferred into a three-necked flask containing 80 ml of ethanol, and 100 μl of APTES was added and refluxed at 60°C for 7 h. The resulting amino-modified blue SiNPs were washed four times with water.

Preparation of SPA-Coated Core-Shell Blue SiNPs

The SPA was combined with core-shell blue SiNPs through covalent crosslinking with a slight modification (26); 2.5 ml of glutaraldehyde and 9 ml of PBS (pH 7.4) were added into the above amino-modified core-shell blue SiNPs and then stirred for 2 h at room temperature to obtain glutaraldehyde-activated blue SiNPs. After that, 1 ml (1 mg/ml) of SPA was added into the above solution with 5 ml of PBS (pH 7.4) and then stirred for another 2 h. The resulting SPA-coated blue SiNPs were collected by centrifugation and dispersed in 10 ml of water with 1% BSA for 1 h at room temperature to block unreacted sites.

Characterization of Synthesized SiNPs and Core-Shell Blue SiNPs

SiNPs and core-shell blue SiNPs were characterized by a transmission electron microscope (TEM) (200 kV) and a Fourier infrared transform spectrometer (FT-IR). KBr was set as the scanning background, and wavenumbers were set to 500–3,500 cm^{-1} of FT-IR. After the dry samples were mixed with KBr, the samples were scanned at a speed of 2 cm^{-1}.

Fabrication of Core-Shell Blue SiNPs-Based LFIA

The structure of the core-shell blue SiNPs-LFIA is shown in **Scheme 1**. LPS (1 mg/ml) and goat anti-mouse IgG (0.6 mg/ml) were loaded on the T line and the control line (C line) separately. The distance between the two pipelines was 5 mm. Finally, NC membrane, releasing pad, adsorbent pad, and sample pad were fabricated onto the backing pad. The LFIA was stored in a dark and dry place.

Brucellosis Serum Samples

Standard brucellosis serum (*B. melitensis*), brucellosis-positive control serum (*B. melitensis*), and negative control serum were purchased from Shanghai Jianglai Biotechnology Co., Ltd. The Brucellosis Prevention and Control Base, Chinese Centers for Disease Control and Prevention (Baicheng, Jilin, China) donated a total of 102 human serum samples from their three clinical groups, including 69 human brucellosis serum samples, 24 negative control serum samples from healthy individuals, and 9 serum samples infected with other bacteria. All the serum samples were stored in a −80°C refrigerator. The serum agglutination test (SAT), the gold standard diagnostic method for brucellosis, was run following the Health Industry Standards of the People's Republic of China: Diagnosis for brucellosis GB/T (WS 269-2019), and each sample was run with three parallel tests. Relevant information on the serum samples is presented in **Supplementary Table 1**.

Application of LFIA in the Diagnosis of Brucellosis

Fifty microliters of human serum sample was fully mixed with 50 μl of blue SiNPs, and then the mixed solution was added dropwise to the sample pad of the strip. After 15 min of reaction, the visual results of the T line and C line were observed by the naked eye. As shown in **Scheme 1**, when the serum was

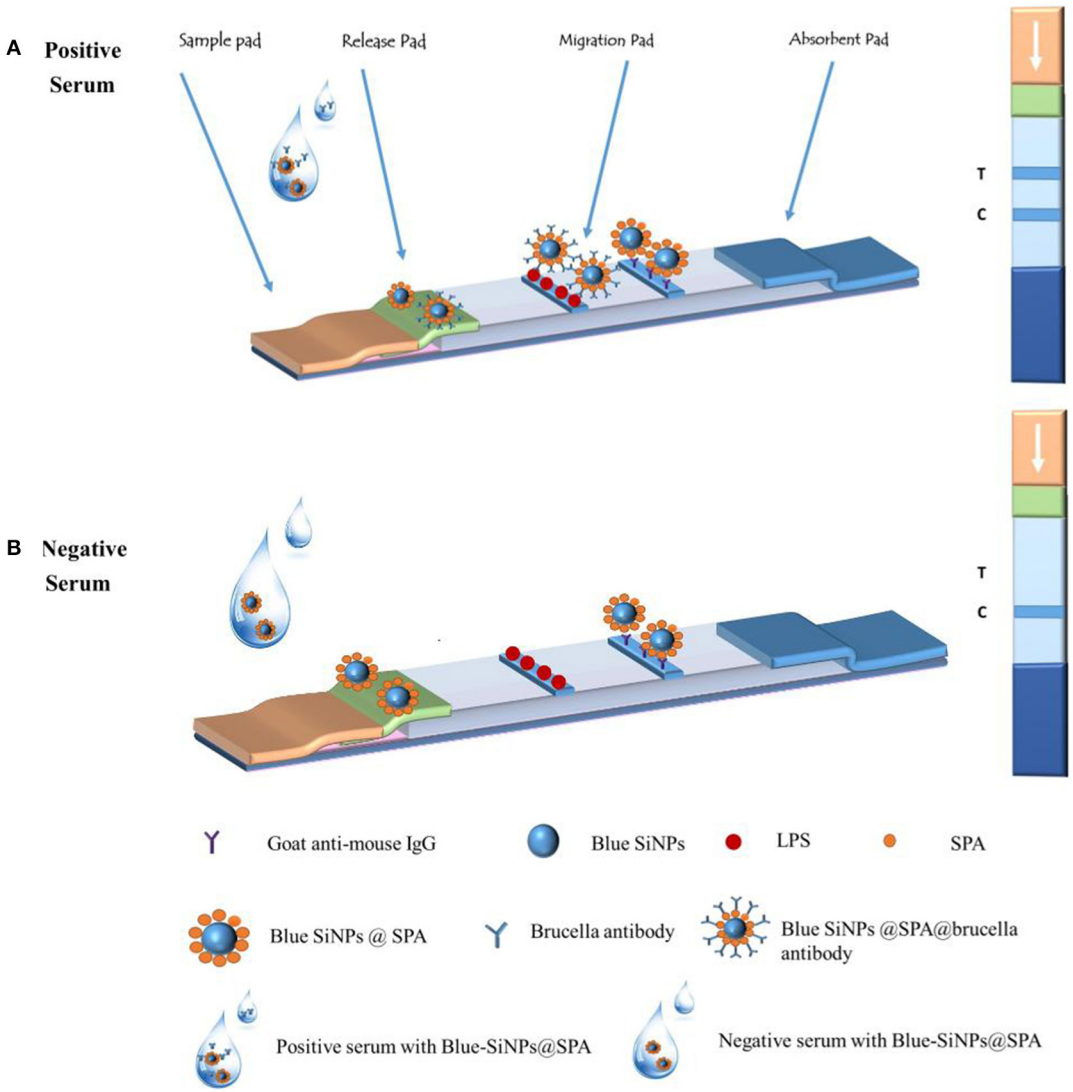

SCHEME 1 | The principle of the core-shell blue SiNPs-based LFIA system and the illustration of the result judgment.

a brucellosis-positive serum, the blue SiNPs@SPA bound with the *Brucella* spp. antibody in the serum, and then the blue SiNPs@SPA with antibody was captured by LPS on the T line, so the T line turned blue; some blue SiNPs@SPA that did not bind with the *Brucella* spp. antibody were captured by the secondary antibody on the C line, making the C line appear blue. When the serum was a brucellosis-negative serum, there was no *Brucella* spp. antibody in the serum; then, the blue SiNPs@SPA was not specifically captured by LPS on the T line, making it appear colorless, while the blue SiNPs@SPA was captured by the secondary antibody on the C line, making the C line appear blue.

To test the specificity of this method, nine non-brucellosis serum samples infected with other bacteria were used: *Escherichia coli O157:H7* serum, *Staphylococcus aureus* serum, *Staphylococcus epidermidis* serum, *Staphylococcus saprophyticus* serum, *Streptococcus salivarius* serum, *Streptococcus anginosus* serum, *Klebsiella pneumoniae* serum, *Salmonella enteritidis* serum, and *Ralstonia picri* serum.

To test the sensitivity of this method, standard brucellosis serum was diluted with saline in the range of 10^{-1} to 10^{-6} IU/ml to test the detection limit based on the methods we developed.

The Comparison Between Our Developed LFIA and Indirect ELISA (IELISA)

In order to verify the effectiveness of the detection method that we developed, we compared the detection results of human serum samples between LFIA and iELISA. The SAT, the gold standard diagnostic method for brucellosis, was run following the Health Industry Standards of the People's Republic of China: Diagnosis for brucellosis GB/T (WS 269-2019), and each sample

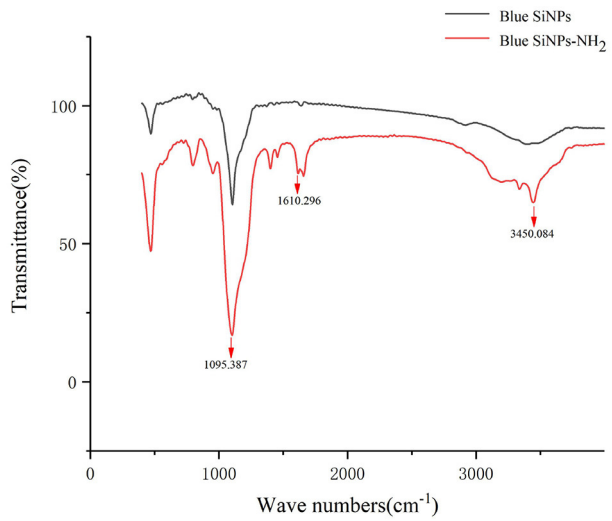

FIGURE 1 | FT-IR spectra of blue SiNPs (top) and blue SiNP-NH_2 (bottom).

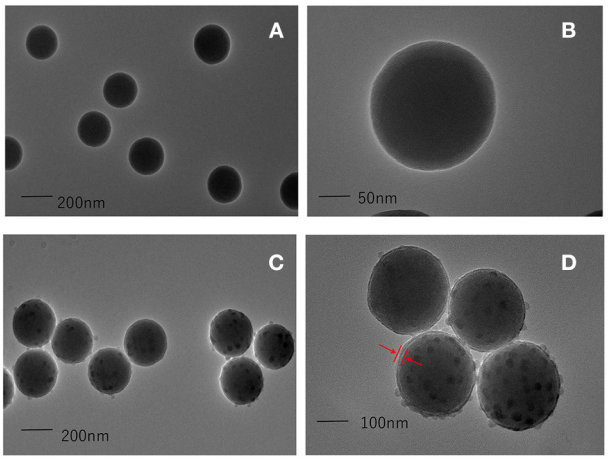

FIGURE 2 | TEM images of colorless SiNPs **(A,B)**, and core-shell blue SiNPs **(C,D)**. The red arrow means that a layer of silica shell has been successfully wrapped on the outside of the silica nanoparticles, and the position of the shell is marked with the red arrow.

was run with three parallel tests. iELISA was run according to the previous protocol.

RESULTS AND DISCUSSION

FT-IR Spectra of Blue SiNPs and Blue SiNPs-NH_2

FT-IR was used to characterize whether the amino group was modified on the surface of SiNPs. FT-IR provided direct proof for the functionalization of amino groups on the SiNPs, because FT-IR can detect the stretching vibration of chemical bonds on the surface of blue SiNPs and blue SiNPs-NH_2, as shown in **Figure 1**. Both blue SiNPs and blue SiNPs-NH_2 showed strong infrared absorption bands in the region of 800–1,180 cm^{-1}, corresponding to Si-O-Si on the silica surface. As shown in the FT-IR absorption spectra of blue SiNPs-NH_2, 3,450 and 1,610 cm^{-1} were attributed to the N-H bonds of the amino group. The above results were comparable with the blue SiNPs being successfully wrapped with an amino-modified silica shell; therefore, it is reasonable to believe that APTES was successfully conjugated with blue SiNPs, and amino groups were successfully coupled on blue SiNPs.

Characterization of Core-Shell Blue SiNPs

A TEM method was used to characterize the synthesized SiNPs. The TEM images of the colorless SiNPs and core-shell blue SiNPs are shown in **Figures 2A,B**. Under the same magnitude of enlargement, both the SiNPs and core-shell blue SiNPs showed good morphology, dispersion, and dispensability. According to the TEM images (**Figures 2C,D**), there was a layer of silica shell that can be seen on the surface of SiNPs (The part indicated by the red arrow). Moreover, in the process of coating SiNPs, many small uneven particles were formed on the surface of the silica shell by self-hydrolysis of TEOS. According to previous literature (17), the unsmooth surface of the particles can provide more binding sites for protein and help to coat more SPA. Therefore, the results of TEM showed that blue SiNPs were successfully prepared in this work.

Also, we tested the steadiness of blue SiNPs compared with colloidal gold nanoparticles in different pH values and different concentrations of salt solution (**Supplementary Figure 1**). The results showed that the scalar variability of pH and concentrations of NaCl solution had little influence on the change in blue SiNPs' color; on the contrary, aggregated colloidal gold nanoparticles demonstrated a different color with the varying pH and concentration of NaCl solution, indicating that blue SiNPs were more stable than colloidal gold nanoparticles at different pH values and concentrations of the NaCl solution. These results indicated that blue SiNPs were more suitable as visible labels of LFIA than colloidal gold nanoparticles due to their good stability.

Characterization of SPA-Conjugated Core-Shell Blue SiNPs

LFIA was employed to identify that SPA-conjugated core-shell blue SiNPs were successfully synthesized. The results could be observed by the naked eye, and it was obvious that the SPA-conjugated core-shell blue SiNPs were captured by a secondary antibody, and it showed a strong blue color at the C line (**Supplementary Figure 2B**). In contrast, the core-shell blue SiNPs could not combine with a secondary antibody, so the C line was colorless (**Supplementary Figure 2A**). This result demonstrated that SPA was successfully combined with core-shell blue SiNPs.

Optimization of Experiment Conditions

Optimization of the Dosage of Dye

To achieve the optimal response condition, four factors that would affect the final results were investigated. First of all, the amount of dye used in the synthesis of blue SiNPs was optimized. When too much dye was used, it was dissolved in the solvent

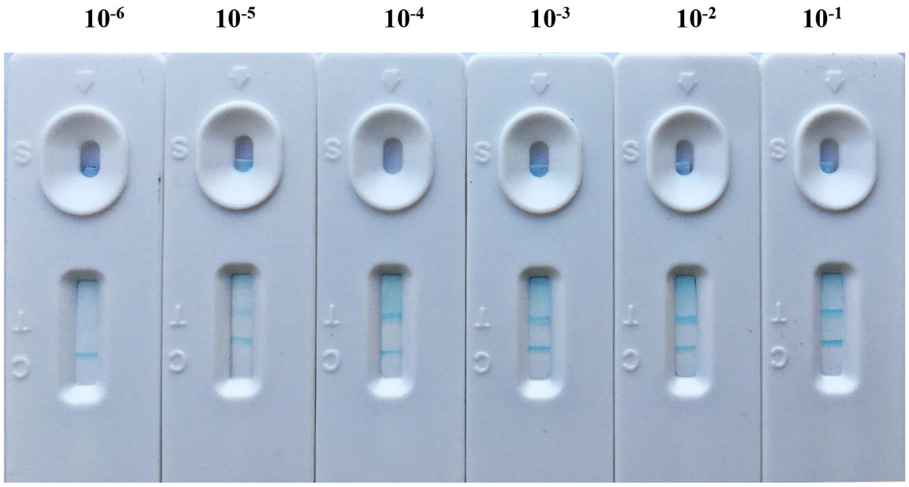

FIGURE 3 | The sensitivity of LFIA based on blue SiNPs for visible detection of standard brucellosis serum, after a series of standard brucellosis-positive serum (standard brucellosis-positive serum was diluted to 10^{-1} to 10^{-6} IU/ml) were mixed with blue SiNPs.

and made it difficult for the blue SiNPs to be coated on the shell, which had been hydrolyzed by TEOS; however, if only a small amount of dye was used, then the color was not bright enough. So, it is necessary to find a suitable amount of dye that can not only make the color of blue SiNPs bright enough, but also prevent interferences. From **Supplementary Figure 3**, the results indicated that when the additional amount of dye was 100 μl (100 mg/ml), the color of blue SiNPs was bright enough and dye did not leak too much. Therefore, we decided to set the final additional amount of dye at 100 μl.

Optimization of the Dosage of LPS

Secondly, the sprayed concentration of LPS on the T line was optimized. It was obvious that the concentration of LPS affected the binding ability of LPS with antibodies in standard brucellosis serum. It can be seen from **Supplementary Figure 4** that when the concentration of LPS was 1 mg/ml, the binding ability of LPS with standard brucellosis serum was better than the other concentrations of LPS. Therefore, 1 mg/ml was chosen as the optimum concentration of LPS.

Optimization of the Dosage of Goat Anti-mouse IgG

Next, we optimized the dosage of goat anti-mouse IgG. The sprayed concentration of goat anti-mouse IgG on the C line of the test strip could affect the binding ability of goat anti-mouse IgG with SPA. The goat anti-mouse IgG was printed in different concentrations (1, 0.8, 0.6, 0.4, and 0.2 mg/ml) on the control line. It can be seen from **Supplementary Figure 5** that when the concentration of goat anti-mouse IgG was 0.6 mg/ml, the color of the C line was bright enough, and the binding ability between goat anti-mouse IgG and SPA was better. In order to save experimental materials, 0.6 mg/ml was chosen as the best concentration of goat anti-mouse IgG.

Optimization of the Dosage of SPA

Finally, we optimized the dosage of SPA. The concentration of SPA that coated on the surface of blue SiNPs could also affect the binding ability between SPA and antibodies in standard brucellosis serum. Experimental studies on the binding ability between SPA and LPS under different concentrations of SPA were carried out, and it can be seen from **Supplementary Figure 6** that when the concentration of SPA was 1 mg/ml, the binding ability was better than the other concentrations. Therefore, 1 mg/ml was chosen as the suitable concentration of SPA.

Sensitivity of Core-Shell Blue SiNPs-Based LFIA

After the abovementioned experiment condition optimization procedure, the core-shell blue SiNPs-based LFIA was evaluated by standard brucellosis serum under optimal conditions. After the series of standard brucellosis serum (standard brucellosis serum was diluted to 10^{-1} to 10^{-6} IU/ml) were mixed with blue SiNPs, the sensitivity of the core-shell blue SiNPs-based LFIA for *Brucella* antibody was obtained. From **Figure 3**, we can see that when the serum dilution was 10^{-5}, the T line still showed a blue color. According to the above results, we can conclude that our LFIA could detect *Brucella* spp. antibody at a level of 10^{-5} (0.01 IU/ml) in serum with no false positives.

Specificity of Core-Shell Blue SiNPs-Based LFIA

The specificity of core-shell blue SiNPs-based LFIA was evaluated with control experiments that involved *S. epidermidis* serum, *S. anginosus* serum, *E. coli O157:H7* serum, *K. pneumoniae* serum, *S. aureus* serum, *S. saprophyticus* serum, *R. picri* serum, *S. enteritidis* serum, and *S. salivarius* serum. To explore the specificity of LFIA based on blue SiNPs to diagnose human brucellosis-positive serum, the nine abovementioned serums, as a control group, were studied. After incubation, we saw that the T line and C line of the strip both displayed a bright blue color in the presence of human brucellosis-positive serum; in contrast, we did not observe a blue color on the T line in the presence of the other tested serums (**Figure 4**). These results indicated the

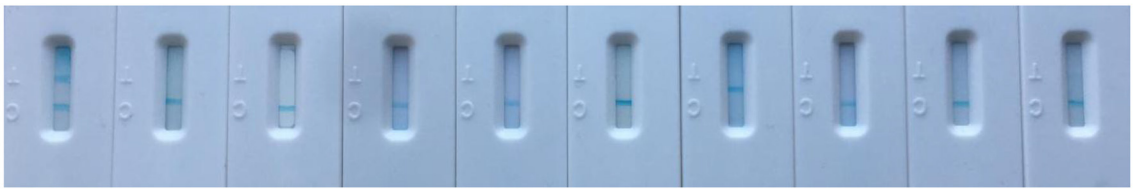

FIGURE 4 | The specificity picture from left to right was **(A)** positive brucellosis serum, **(B)** *Staphylococcus epidermidis* serum, **(C)** *Streptococcus anginosus* serum, **(D)** *Escherichia coli O157:H7* serum, **(E)** *Klebsiella pneumoniae* serum, **(F)** *Staphylococcus aureus* serum, **(G)** *Staphylococcus saprophyticus* serum, **(H)** *Ralstonia picri* serum, **(I)** *Salmonella enteritidis* serum, and **(J)** *Streptococcus salivarius* serum.

TABLE 1 | The evaluation results of our developed LFIA and iELISA.

Methods	Cutoff value	Positive		Negative		PPV (%)	NPV (%)
		TP	FN	TN	FP		
LFIA	≥68.94	61	2	31	8	87.0	93.9
iELISA	≥0.532	59	1	32	10	85.5	96.9

SAT was used as the gold standard to distinguish the results of LFIA and iELISA. TP, true positive; TN, true negative; FP, false positive; FN, false negative; PPV, positive predictive value, TP/(TP+FP) × 100%; NPV, negative predictive value, TN/(TN+FN) × 100%.

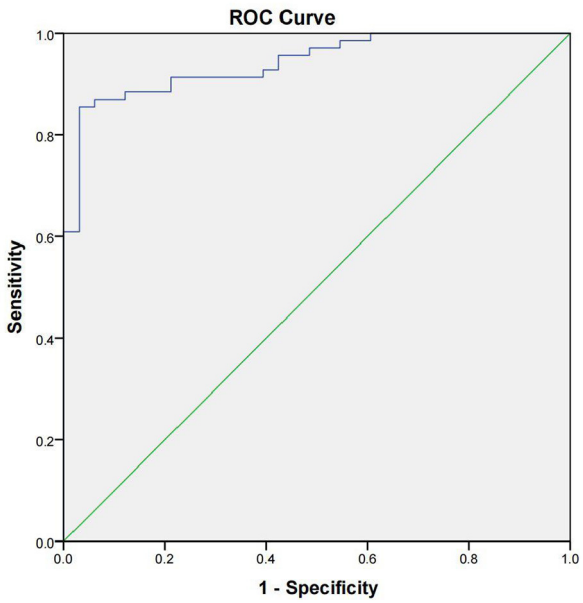

FIGURE 5 | The receiver operating characteristic curve of the lateral flow immunoassay with the SAT method as state variable. The area under the curve (AUC) was 0.942 (95% CI, 0.900–0.984); the standard errors (under the non-parametric assumption) were 0.022, $p < 0.05$.

excellent specificity of our testing strip based on the core-shell blue SiNPs for the detection of human brucellosis serum.

Detection of Human Serum Samples

In order to evaluate the sensitivity and accuracy of our method, we applied our developed method to detect human serum samples. A total of 102 human serum samples were firstly detected by the serum agglutination test (SAT) to determine whether the serum could be diagnosed as positive or negative; SAT followed the Health Industry Standards of the People's Republic of China: Diagnosis for brucellosis GB/T (WS 269-2019) to guarantee that there were no false positives, and each sample was run with three parallel tests to ensure accuracy. Indeed, the LFIA that we developed could detect antibodies in serum, in the whole blood, and even in plasma. Usually in a typical LFIA, the complex matrix can make the NC membrane change colors, which leads to a high background, especially in whole blood. However, due to the bright color of the blue SiNPs, even if the NC membrane turns red, the results were also easy to observe. In particular, the SiNPs can combine with a variety of dyes and appear in a variety of colors; therefore, the SiNPs can be more widely applied in the detection technology.

We applied our developed LFIA to detect 69 positive brucellosis serum samples, 24 negative brucellosis serum samples, and nine non-brucellosis serum samples infected with other bacteria samples, and all the serum samples were verified by SAT. The sensitivity, specificity, and accuracy of core-shell blue SiNPs-based LFIA were assessed completely. From the results, we can see that with our method, 61 positive brucellosis serum samples were identified as "positive" correctly, eight positive brucellosis serum samples were wrongly identified as "negative," 2 negative serum samples were wrongly identified as positive, and 31 of the negative samples were identified as "negative" correctly, as described in **Table 1**. Also, we used SPSS software to draw a receiver operating characteristic (ROC) curve (**Figure 5**) to evaluate the feasibility of our strip for actual samples; area under the curve (AUC) was used to present the accuracy of the method. The AUC of our experiment was 0.942 [95% confidence interval (CI), 0.900 to 0.984], demonstrating that the accuracy of this method is convincing and our detection results are highly authentic. In addition, a positive predictive value (PPV) of 87.0% and a negative predictive value (NPV) of 93.9% of our developed method were obtained from an optimum cutoff value of 68.94 (Youden's index optimum). With this cutoff value, 61 of 69 brucellosis samples were screened correctly as positive, and only two negative cases were screened incorrectly as positive.

Furthermore, we also compared our methods with iELISA to evaluate the sensitivity and specificity. Compared with our

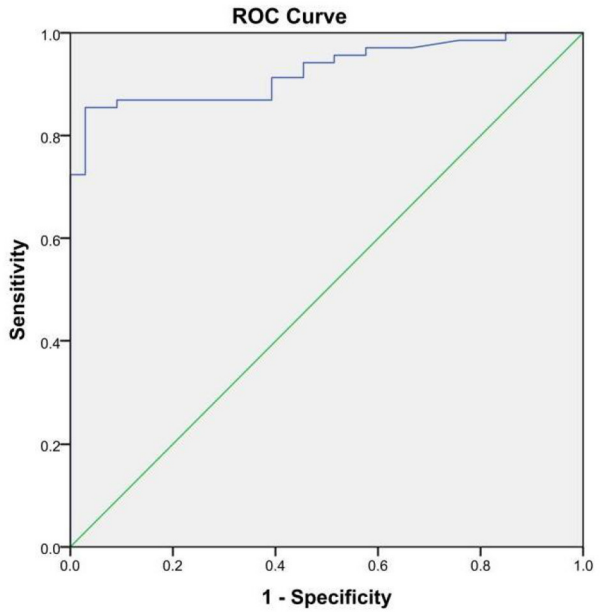

FIGURE 6 | The receiver operating characteristic curve of the indirect ELISA with the SAT method as state variable. The area under the curve (AUC) was 0.926 (95%CI, 0.877–0.975); the standard errors (under the non-parametric assumption) were 0.025, $p < 0.05$.

developed method, iELISA was also used to detect the same 102 serum samples, and the resulting ROC curve and the results of iELISA are shown in **Figure 6** and **Table 1**. From **Figure 6**, we can see that the AUC of the ROC curve was 0.926 (95% CI, 0.877–0.975). When the optimal cutoff value was selected at 0.532 (Youden's index optimum) as the standard critical value of diagnosis, the PPV was 85.5% and the NPV was 96.9%. With this cutoff value, 59 of 69 brucellosis samples were screened correctly as positive, and only one negative case was screened incorrectly as positive. Above all, there was no significant difference in the diagnostic sensitivity and specificity between our developed LFIA and iELISA (**Table 1**). Furthermore, the sensitivity of our experiment was slightly better than iELISA. These results indicated that the accuracy and sensitivity of our method were reliable, and our developed method can be applied in the diagnosis of human brucellosis in the future.

DISCUSSION AND CONCLUSION

As a new nanomaterial, SiNPs have significant advantages, namely, stability and feasibility, compared with other nanoparticles. Based on their stability, bioavailability, colorfulness, sensitivity, and specificity, SiNPs have shown great promise in immunology (27), virus detection (28), cell biology (29), and environmental monitoring (30). Blue SiNPs as a new nanomaterial were used as a signal probe and SPA was used as a capture probe to catch and immobilize antibodies in the serum as well as combined with the secondary antibody on the C line in our research. When SPA-functionalized blue SiNPs (the capture probe) were obtained, the capture probe could catch the antibody when the serum was brucellosis-positive, and then the captured antibody specifically bound with LPS on the T line, which made the T line blue. The probe we synthesized had better stability and sensitivity compared with other traditional capture probes. As the signal probe, the SiNPs were coated with dye and then were wrapped with a silica shell hydrolyzed by TEOS, demonstrating its environmentally friendly and simplified procedure. The usage of SPA made the detection more accurate and simple. SPA can be linked to the Fc fragment of IgG molecules by hydrophobic interactions, resulting in the orientation and arrangement of antibody molecule probes on the surface of blue SiNPs. This oriented fixation is better organized than either direct physical adsorption or covalent binding, and it has less impact on the activity of antibodies. Thus, the entire activity of the functionalized capture probe has been improved (4, 31). Above all, a LFIA-based visible blue SiNPs label was developed for the rapid screening or diagnosis of people who have suffered from human brucellosis. As a promising probe, blue SiNPs can be successfully applied in the detection of human brucellosis by LFIA. Compared with the traditional diagnosis methods, the LFIA based on blue SiNPs can not only save time but also reduce cost simultaneously; in addition, blue SiNPs have many advantages such as good stability, bright color, and lower price, compared to other traditional methods. Taken together, these results suggest that the LFIA based on the blue SiNPs can be applied to diagnose brucellosis in remote areas where there is a lack of testing condition and instruments. Moreover, the minimize visual cutoff values of the antibody titer in serum was 0.01 IU/ml, indicating the high sensitivity of our method. Additionally, there was no cross-reaction between different serum samples when we applied the strip to human serum samples from different individuals infected with various microorganisms. In summary, the blue SiNPs-based LFIA has shown great promise for rapid and inexpensive diagnosis of human brucellosis. Moreover, this LFIA-based detection method may have future application for multiple immunochromatography detection, which deserves further development. As far as our current experiment is concerned, a single color cannot be satisfied with multiple detection. In the future, we will also develop various colored SiNPs for multiple immunochromatography detection.

DATA AVAILABILITY STATEMENT

The original contributions presented in the study are included in the article/**Supplementary Material**, further inquiries can be directed to the corresponding authors.

ETHICS STATEMENT

The studies involving human participants were reviewed and approved by Institutional Research Ethics Committee of Medicine, the School of Public Health, Jilin University, permit number: JLU2014-0303.2.4. The patients/participants provided their written informed consent to participate in this study.

AUTHOR CONTRIBUTIONS

LG, JL, and KX conceived and designed the study. LG, DW, FL, and YZ performed the assay of experimental detection. YW, JZ, and LZ analyzed the data. LG drafted the manuscript. JL, JW, and XS provided constructive opinions and suggestions. KX, JL, and XS reviewed and made improvements in the manuscript. All authors have read and approved the final version of this manuscript.

FUNDING

This work was financially supported by the Department of Education of Jilin Province, China (Grant Numbers: JJKH20211221KJ, JJKH20180239KJ and JJKH20211220KJ), the National Natural Science Foundation of China (Grant Numbers: 82173572 and 81401721), the Science and Technology Development Bureau of Jilin Province, China (Grant Number: 2018010195JC), the Jilin Provincial Development and Reform Commission (Grant Number: 2020C038-7), the Jilin Provincial Health and Family Planning Commission (Grant Number: 2017J074), and the Graduate Innovation Fund of Jilin University (Grant Number: 101832020CX275).

ACKNOWLEDGMENTS

All authors are aware of the common instruments and equipment of Jilin University. The authors thank Dali Wang for the donation of human serum by the China Center for Disease Control and Prevention of Baicheng, Jilin Province, China.

SUPPLEMENTARY MATERIAL

The Supplementary Material for this article can be found online at: https://www.frontiersin.org/articles/10.3389/fvets.2021.771341/full#supplementary-material

REFERENCES

1. Liu J, Wang B, Huang HC, Jian D, Lu YA, Shan YK, et al. Quantitative ciprofloxacin on-site rapid detections using quantum dot microsphere based immunochromatographic test strips. *Food Chem.* (2021) 335:127596. doi: 10.1016/j.foodchem.2020.127596
2. Zhang B, Yang XS, Liu XX Li J, Wang CW, Wang SQ. Polyethyleneimine-interlayered silica-core quantum dot-shell nanocomposites for sensitive detection of *Salmonella typhimurium* via a lateral flow immunoassay. *R Soc Chem Adv.* (2020) 10:2483–9. doi: 10.1039/c9ra09252h
3. Wang C, Li XM, Peng T, Wang ZH, Wen K, Jiang HY. Latex bead and colloidal gold applied in a multiplex immunochromatographic assay for high-throughput detection of three classes of antibiotic residues in milk. *Food Control.* (2017) 77:1–7. doi: 10.1016/j.foodcont.2017.01.016
4. Mu XH, Tong ZY, Huang QB, Liu B, Liu ZW, Hao LQ, et al. Nano-magnetic immunosensor based on staphylococcus protein A and the amplification effect of HRP-conjugated phage antibody. *Sensors.* (2015) 15:3896–910. doi: 10.3390/s150203896
5. Xu W, Chen XL, Huang XL, Yang WC, Liu CM, Lai WH, et al. Ru(phen)(3)(2+) dope silica nanoparticle based immunochromatographic strip for rapid quantitative detection of beta-agonist residues in swine urine. *Talanta.* (2013) 114:160–6. doi: 10.1016/j.talanta.2013.04.013
6. Zhu CJ, Zhao GY, Dou WC. Immunochromatographic assay using brightly colored silica nanoparticles as visible label for point-of-care detection of clenbuterol. *Sens Actuators B.* (2018) 266:392–9. doi: 10.1016/j.snb.2018.03.085
7. Yang QH, Gong XQ, Song T, Yang JM, Zhu SJ Li YH, et al. Quantum dot-based immunochromatography test strip for rapid, quantitative and sensitive detection of alphafetoprotein. *Biosens Bioelectron.* (2011) 30:145–50. doi: 10.1016/j.bios.2011.09.002
8. Medintz I, Uyeda HE, Goldman ER, Mattoussi H. Quantum dot bioconjugates for imaging, labelling and sensing. *Nat Mater.* (2005) 4:435–46. doi: 10.1038/nmat1390
9. Zhao XJ, Bagwe RP, Tan WH. Development of organic-dye-doped silica nanoparticles in a reverse microemulsion. *Adv Mater.* (2004) 16:173–6. doi: 10.1002/adma.200305622
10. Bagwe RP, Yang CY, Hilliard LR, Tan WH. Optimization of dye-doped silica nanoparticles prepared using a reverse microemulsion method. *Langmuir.* (2004) 20:8336–42. doi: 10.1021/la049137j
11. Bagwe RP, Hilliard LR, Tan WH. Surface modification of silica nanoparticles to reduce aggregation and nonspecific binding. *Langmuir.* (2006) 22:4357–62. doi: 10.1021/la052797j
12. Montalti M, Prodi L, Rampazzo E, Zaccheroni N. Dye-doped silica nanoparticles as luminescent organized systems for nanomedicine. *Chem Soc Rev.* (2014) 43:4243–68. doi: 10.1039/c3cs60433k
13. Su ZX, Zhao GY, Dou WC. Determination of trace aflatoxin M1(AFM1) residue in milk by an immunochromatographic assay based on (PEI/PSS)(4) red silica nanoparticles. *Microchimica Acta.* (2020) 187:658. doi: 10.1007/s00604-020-04636-6
14. Senarath-Yapa MD, Phimphivong S, Coym JW, Wirth MJ, Aspinwall CA, Saavedra SS. Preparation and characterization of poly(lipid)-coated, fluorophore-doped silica nanoparticles for biolabeling and cellular imaging. *Langmuir.* (2007) 23:12624–33. doi: 10.1021/la701917w
15. Yu H, Zhao GY, Dou WC. Simultaneous detection of pathogenic bacteria using agglutination test based on colored silica nanoparticles. *Curr Pharm Biotechnol.* (2015) 16:716. doi: 10.2174/1389201016666150505121713
16. Sun Q, Zhao GY, Dou WC. Blue silica nanoparticle-based colorimetric immunoassay for detection of *Salmonella pullorum*. *Anal Methods.* (2015) 7:8647–54. doi: 10.1039/c5ay02073e
17. Sun Q, Zhao GY, Dou WC. A nonenzymatic optical immunoassay strategy for detection of Salmonella infection based on blue silica nanoparticles. *Anal Chim Acta.* (2015) 898:109–15. doi: 10.1016/j.aca.2015.09.041
18. Schmoock G, Ehricht R, Melzer F, Elschner M, Tomaso H, Neubauer H, et al. Development of a diagnostic multiplex polymerase chain reaction microarray assay to detect and differentiate Brucella spp. *Diagn Microbiol Infect Dis.* (2011) 71:341–53. doi: 10.1016/j.diagmicrobio.2011.08.013
19. Foster G, Osterman BS, Godfroid J, Jacques I, Cloeckaert A. *Brucella ceti* sp. nov and *Brucella pinnipedialis* sp. nov for Brucella strains with cetaceans and seals as their preferred hosts. *Int J Syst Evol Microbiol.* (2007) 57:2688–93. doi: 10.1099/ijs.0.65269-0
20. Scholz HC, Hubalek Z, Sedlacek I, Vergnaud G, Tomaso H, Al Dahouk S, et al. *Brucellamicroti* sp. nov, isolated from the common vole *Microtus arvalis*. *Int J Syst Evol Microbiol.* (2008) 58:375–82. doi: 10.1099/ijs.0.65356-0
21. Scholz HC, Nöckler K, Gollner C, Bahn P, Vergnaud G, Tomaso H, et al. *Brucellainopinata* sp. nov, isolated from a breast implant infection. *Int J Syst Evol Microbiol.* (2010) 60:801–8. doi: 10.1099/ijs.0.011148-0
22. Eisenberg T, Hamann HP, Kaim U, Schlez K, Seeger H, Schauerte N, et al. Isolation of potentially novel *Brucella* spp. from frogs. *Appl Environ Microbiol.* (2012) 78:3753–5. doi: 10.1128/AEM.07509-11
23. Li MH, Liu ZG, Pu DR, Zhao HY, Tian GZ, Jiang H. Genetic polymorphism analysis of rpoB gene of Brucella melitensis strains isolated in China. *Dis Surveillance.* (2018) 33:193–7. doi: 10.3784/j.issn.1003-9961.2018.03.006
24. Zhu MS, Zhang J, Cao JJ, Ma JF Li XR, Shi F. Ultrasensitive dual-color rapid lateral flow immunoassay via gold nanoparticles with two different

morphologies for the serodiagnosis of human brucellosis. *Anal Bioanal Chem.* (2019) 411:8033–42. doi: 10.1007/s00216-019-02156-8
25. Yu QQ, Liu J, Zhao GY, Dou WC. A silica nanoparticle based 2-color immunochromatographic assay for simultaneous determination of clenbuterol and ractopamine. *Microchim Acta.* (2019) 186:421. doi: 10.1007/s00604-019-3529-z
26. Aramesh M, Shimoni O, Ostrikov K, Prawer, S, Cervenka, J. Surface charge effects in protein adsorption on nanodiamonds. *Nanoscale.* (2015).7:5726–36. doi: 10.1039/c5nr00250h
27. Shams A, Zarif BR, Salouti M, Shapouri R, Mirzaii S. Designing an immunosensors for detection of Brucella abortus based on coloured silica nanoparticles. *Artif Cells Nanomed Biotechnol.* (2019) 47:4109. doi: 10.1080/21691401.2019.1674496
28. Liu J, Yu QQ, Zhao GY, Dou WC. A novel immunochromatographic assay using ultramarine blue particles as visible label for quantitative detection of hepatitis B virus surface antigen. *Anal Chim Acta.* (2020) 1098:140–7. doi: 10.1016/j.aca.2019.11.037
29. Di Sano C, D'Anna C, Scurria A, Lino C, Pagliaro M, Ciriminna R, et al. Mesoporous silica particles functionalized with newly extracted fish oil (Omeg@Silica) inhibit lung cancer cell growth. *Nanomedicine.* (2021) 16:2061–74. doi: 10.2217/nnm-2021-0202
30. Yu ZX, Min X, Li F, Chen Q. Synthesis of Ag–SiO2–APTES nanocomposites by blending Poly(Vinylidene Fluoride) Membrane with Potential Applications on Dye Wastewater Treatment. *Nano.* (2018) 13:1–12. doi: 10.1142/S1793292018500340
31. Mu XH, Tong ZY, Huang QB, Liu B, Liu ZW, Hao LQ, et al. An electrochemiluminescence immunosensor based on gold-magnetic nanoparticles and phage displayed antibodies. *Sensors.* (2016) 16:308. doi: 10.3390/s1603 0308

Conflict of Interest: The authors declare that the research was conducted in the absence of any commercial or financial relationships that could be construed as a potential conflict of interest.

Publisher's Note: All claims expressed in this article are solely those of the authors and do not necessarily represent those of their affiliated organizations, or those of the publisher, the editors and the reviewers. Any product that may be evaluated in this article, or claim that may be made by its manufacturer, is not guaranteed or endorsed by the publisher.

frontiers | Frontiers in Nanotechnology

TYPE Original Research
PUBLISHED 29 March 2023
DOI 10.3389/fnano.2023.1132783

OPEN ACCESS

EDITED BY
Gerson Nakazato,
State University of Londrina, Brazil

REVIEWED BY
Puneet Khandelwal,
Johns Hopkins Medicine, United States
Pramod K. Gupta,
Fraunhofer USA (FHG), United States
Hongwu Sun,
Third Military Medical University, China
Sri Ramulu Torati,
Old Dominion University, United States
Ateet Dutt,
National Autonomous University of Mexico, Mexico

*CORRESPONDENCE
Duraipandian Thavaselvam,
dtselvam.drde@gov.in

SPECIALTY SECTION
This article was submitted to Biomedical Nanotechnology, a section of the journal Frontiers in Nanotechnology

RECEIVED 27 December 2022
ACCEPTED 20 February 2023
PUBLISHED 29 March 2023

CITATION
Hans R, Yadav PK, Zaman MB, Poolla R and Thavaselvam D (2023), A rapid direct-differential agglutination assay for *Brucella* detection using antibodies conjugated with functionalized gold nanoparticles.
Front. Nanotechnol. 5:1132783.
doi: 10.3389/fnano.2023.1132783

A rapid direct-differential agglutination assay for *Brucella* detection using antibodies conjugated with functionalized gold nanoparticles

Richa Hans[1], Pranjal Kumar Yadav[1], M. Burhanuz Zaman[2], Rajaram Poolla[2] and Duraipandian Thavaselvam[3]*

[1]Division of Biodetector Development Test and Evaluation, Defence Research and Development Establishment (DRDO), Gwalior, Madhya Pradesh, India, [2]School of Studies in Physics, Jiwaji University, Gwalior, Madhya Pradesh, India, [3]Director General Life Sciences (DGLS) Office, Defence Research and Development Organization (DRDO) Headquarters, Ministry of Defence, SSPL Campus, Timarpur, New Delhi, India

Brucellosis is the most widespread and serious zoonotic disease worldwide which affects livestock, sylvatic wildlife, marine dwellers, and humans. It is acquired through Alphaproteobacteria which belong to the genus *Brucella* and is categorized as a potential bio-threat agent. In this study, we developed a rapid and direct differential whole cell (WC) agglutination-based assay for its on-field detection. The recombinant outer membrane (rOmp28) protein-derived specific mice IgG polyclonal antibodies (pAbs) of *Brucella* were purified using affinity chromatography and conjugated with functionalized gold nanoparticles (AuNPs) for rapid agglutination. A positive blot of 32 kDa protein revealed specific immuno-reactivity of rOmp28-pAbs using immunoblot analysis. For the synthesis of AuNPs, the conventional "Turkevich method" was optimized at a concentration < 1 mM of gold precursor for obtaining 50-nm-sized particles. Also, their physico-chemical characteristics were analyzed using UV-visible spectrophotometry, Fourier transform infra-red spectroscopy (FT-IR), Raman spectroscopy, X-ray diffraction (XRD), scanning electron microscopy (SEM), transmission electron microscopy (TEM), dynamic light scattering (DLS), zeta potential (ζ, ZP), and fluorescence spectroscopy. Furthermore, these AuNPs were functionalized with N-(3-dimethylaminopropyl)-N′-ethylcarbodiimide hydrochloride (EDC) and N-hydroxysuccinimide (NHS) to prepare modified carboxylated AuNPs. For bioconjugation with *Brucella* rOmp28 IgG pAbs, antibody-conjugated functionalized AuNP constructs were prepared and characterized using FT-IR analysis with strong N–H deformations. Subsequently, these bioconjugated AuNPs were used to develop a direct-differential slide agglutination assay with a detection limit of 10^4 CFU mL^{-1}. The sensitivity of this assay was compared with standard double-antibody sandwich ELISA (S-ELISA) using rOmp28 IgG pAbs with an LOD of 10^3 CFU mL^{-1} and a detection range of 10^2–10^8 CFU mL^{-1}. No intraspecies cross-reactivity was observed based on evaluation of its specificity with a battery of closely related bacterial species. In conclusion, the increased sensitivity and specificity of the developed agglutination assay obtained using bioconjugated functionalized AuNPs is ≥ 98% for the detection of *Brucella*. Therefore, it can be used as an alternate rapid method of direct WC detection

of bacteria as it is simple, robust, and cost-effective, with minimal time of reaction in the case of early disease diagnosis.

KEYWORDS

Brucella, agglutination assay, rOmp28, gold nanoparticles, outer membrane protein, polyclonal antibody

1 Introduction

Brucellosis is an endemic, mostly neglected but re-emerging, bacterial zoonosis; it mostly affects the world's low-income and low–middle income countries (Lemos et al., 2018; Bagheri Nejad et al., 2020). Its infection is spread by small, aerobic, intracellular, facultative, Gram-negative coccobacilli bacteria of the genus *Brucella*, and is considered one of the most economically important public health concerns (Bakri et al., 2018; Jansen et al., 2020). Brucellosis was propounded for the first time by Sir David Bruce on military campaigns in Malta, predominantly in the central Mediterranean region along with Sir M. Louis Hughes and Themistocles Zammit (Sayer, 2016). Sir Zammit explored the association of this disease with the consumption of raw milk from naturally infected goats and discovered its route of transmission (Wyatt, 2013). This disease is prevalent worldwide, mainly occurring in Central Asia and the Middle East; it is also widespread in South Asian countries such as India, China, Pakistan, and Sri Lanka, with sero-positive cases of human brucellosis mostly in agro-farmers, veterinary professionals, slaughter houses, and dairy workers (Guan et al., 2018; Xu et al., 2020). The four main species of *Brucella* (*Brucella abortus*, *Brucella melitensis*, *Brucella canis*, and *Brucella suis*) are well-known for their sustained endemicity, wide distribution, and prolonged systemic cases of Brucellosis in both domestic and wild hosts (Olsen and Tatum, 2016; Olsen et al., 2018; Yagupsky et al., 2019). On infection with brucellosis, livestock suffer from reduced milk production followed by frequent abortions, still births, retained placental lesions, vesiculitis, orchitis, epididymitis, and life-time sterility (El-Sayed and Awad, 2018; Khan et al., 2020). In humans, the symptoms include high undulant fever of unknown origin (FUO), focal complications with severe flu-like symptoms, fatigue, myalgia, neurobrucellosis, hepatosplenomegaly, loss of appetite, premature delivery, arthritis, septicemia, and destructive localized spinal infections (Rubach et al., 2013; Khan and Zahoor, 2018; Ukita et al., 2021). *Brucella* infection in humans is transmitted through consumption of unpasteurized milk, raw or undercooked meat, and infected animal by-products (MusallamAbo-Shehada et al., 2016; Holt et al., 2021). Occupational hazards and environmental disease reservoirs also propagate brucellosis infection in agriculture-based pastoral communities (Galinska and Zagorski, 2013; Shi et al., 2021). The transmission of bovine brucellosis is rapid, debilitating, and most prevalent in areas dominated by animal husbandry, and, because of its complex treatments in the absence of specific vaccines for humans, *Brucella* has become a candidate agent of major bioweapons (Pappas et al., 2006; Boggiatto et al., 2019; Yagupsky et al., 2019). For proper control and prevention of increased cases of brucellosis, serological surveillance, bacteriological investigation, immunoassay-based detection, and alternate diagnostic methods are deliberately used in screening acute and chronic cases (Lalsiamthara and Lee, 2017). The improper clinical management and misidentification of *Brucella* also contribute to the relapse of infection (Etemadi et al., 2019). Several tests which are based upon serological implications and its characterization are routinely used to test *Brucella*-related infection such as serum tube agglutination test (SAT), Rose Bengal plate test (RBPT), enzyme-linked immunosorbent assay (ELISA), 2-β mercaptoethanol test (2 ME), complement fixation test (CFT), and Brucellin skin test (BST) (Yohannes et al., 2012; Moreno et al., 2022). Direct slide agglutination assays are sensitive, cost-effective, rapid, and simple in terms of facilitating users with less expertise and require minimum time for multiple-sample testing (Saxena, 2012; Saxena and Kaur, 2013; Purwar et al., 2016). Such types of serological tests for the diagnosis of brucellosis in bovines, caprines, and ovines explore common surface antigens present in different species and strains of *Brucella* (Ghazy et al., 2016; Govindasamy et al., 2021). The sensitivity of the standard agglutination test was reported to be 95.6 %, with a specificity of 100 % at 1/320 antibody dilution using the standardized set of *Brucella* antigens (Memish et al., 2002). Also, in another study, the sensitivity and specificity of the immunocapture agglutination assay were reported to be 90.6%, with 94.2 % of negative predictive values determining the blocking antibodies in preliminary diagnosis of *Brucella* (Ozdemir et al., 2011). A rapid slide agglutination test using latex beads coated with four recombinant antigens of *Brucella* as potential biomarkers was reported to offer high specificity in serodiagnosis of canine brucellosis (Watarai et al., 2007). Moreover, the Centers for Disease Control and Prevention (CDC) has also recommended the use of *Brucella*-specific agglutination methods for further advent confirmations of serologically tested positive samples and all equivocals which are parallely screened by enzyme immunoassay (EIA) (Centers for Disease Control and Prevention (CDC), 2005). Therefore, a combination of available potential serological and molecular tests along with rapid agglutination assays can facilitate specific detection of *Brucella* with no time delay in cases of early clinical emergency (Al Dahouk and Nockler, 2011; Di Bonaventura et al., 2021; Lukambagire et al., 2021; Suo et al., 2021). Significantly, the primary and secondary polyclonal antibodies (pAbs) specific to immuno-dominant cellular antigens of *Brucella* can also be utilized efficiently in conjugation with various nanoparticles and functionalized biosensors for *Brucella* species-level detection in clinical samples (Baltierra-Uribe et al., 2019; Taheri et al., 2020). The active adsorption of specific IgG pAbs and monoclonal antibodies (mAbs) onto functionalized nanoparticles enhances the rate of agglutination reaction and antigen–antibody binding avidity due to multivalent effects (Choktaweesak et al., 2016; Busch et al., 2019). Recently, an immuno-chromatographic test system was developed for rapid serodiagnosis of *Brucella* based on the application of gold nanoparticles and quantum dots for detection of low but diagnostically significant titers of specific antibodies in revealing sub-clinical stages of brucellosis (Sotnikov et al., 2020). Another potential colorimetric immunoassay was developed for prompt detection of *Brucella abortus* using immunosensors conjugated with pAbs on activation, with 1-ethyl-3-(3-dimethylaminopropyl)-carbodiimide (EDC) and N-hydroxysuccinimide (NHS) as efficient detection probes (Shams et al., 2019). pAbs were conjugated with quantum dots, and

modified magnetic beads along with gold nanoparticle-screen printed carbon electrodes were shown to detect *Brucella* at 10^2 and 10^5 CFU mL^{-1}, respectively (Wu et al., 2013; Song et al., 2017). When such modified approaches were applied together with a sandwich immunoassay, successful detection of *Brucella* antibodies from multiple test serum samples was achieved (Li et al., 2017). Although the gold standard, known for early disease diagnosis, potentially relies on the propagation of bacterial cell culture, the use of specific isolation techniques and culture-based methods are very laborious, time-consuming, not used routinely, not cost-effective, methodologically complex, and requires highly skilled technical subject experts for handling of infectious live cultures (Sagi et al., 2017; Santos et al., 2021). The new approach of developing test methods based on specific antigen–antibody conjugation with metallic nanoparticles is conversely more reliable, efficient, and robust for low pathogen detection (Malaspina et al., 2017; Lin et al., 2021). Functionalized bioconjugated AuNPs exhibit unique optical properties that not only improve biosensing technology but also the specificity of antigen–antibody interactions for the development of rapid on-field detection assays (Tripathi and Driskell, 2018; Okyem et al., 2021). Moreover, the performance of commonly used ELISAs, to overcome existing challenges associated with sensitivity and stability, can be improved by exploring the unique physical and chemical properties of metal oxide nanoparticles (Gao et al., 2020). One such modified test method is a hybridization assay; the use of conjugated metal nanoparticles resulted in sensitive detection of *Brucella* up to 10^3 CFU mL^{-1} during direct visual detection of specific DNA sequences (Pal et al., 2017). In recent reports, the efficacy of anti-spike antibody and 4-aminothiophenol-conjugated gold nanoparticle-based SERS was newly demonstrated for detecting low concentrations of such microbiological viral antigens (1,000 virus particles per mL) within 5 min (Pramanik et al., 2021). Recently, in the case of *Brucella*, reduced limits of detection were observed with a new version of rapid vertical flow technology that can detect 4 IU mL^{-1} of the *Brucella* antibody as the experimental lower limit, with gold nanoparticles treated with β-cyclodextrin as a reducing agent (Fang et al., 2022). Also, a lateral flow immunoassay (LFA) strip test using anti-*Brucella* pAbs conjugated with colloidal AuNPs was reported, which can detect 10^7 CFU mL^{-1} of inactivated whole cells of *Brucella abortus* S99 (Prakash et al., 2021). In the present study, we functionalized and conjugated AuNPs to *Brucella* species-specific recombinant outer membrane protein (rOmp28)-derived mice IgG pAbs for enhancing the specific binding of avid antigen–antibody complexes by employing a rapid direct-differential slide agglutination assay in the predominant whole-cell detection of *Brucella*. The developed assay is highly sensitive and specific, with minimal time of reaction, and can be deployed in both field-based and clinical applications for screening multiple sample matrices concomitant to animal and human brucellosis.

2 Material and methods

The present study includes the preparation and functionalization of AuNPs prior to bioconjugation with mice IgG pAbs derived from *Brucella melitensis* 16M-specific recombinant outer membrane protein (rOmp28) for developing a direct-differential slide agglutination assay as shown in the schematic (Figure 1). Initially, the assay was optimized for sensitivity with a detection range and limit of detection (LOD) of 10^1–10^8 CFU mL^{-1} with two standard species of *Brucella* (*Brucella melitensis* 16M and *Brucella abortus* S99); there was further screening with a total of 36 clinical isolates and nine other standard strains of *Brucella* at the lowest LOD of 10^4 CFU mL^{-1}. The specificity of the assay was evaluated by a cross-reactive study with 26 other bacterial species closely related to *Brucella*. Validation of the experimental assay was performed by direct-slide agglutination of spiked whole cell (WC) Ags of *Brucella* in both clinical (urine and serum) and non-clinical (raw-milk) sample matrices. Furthermore, the specific potential efficacy of rOmp28-derived mice IgG pAbs was evaluated using earlier optimized double-antibody sandwich ELISA (S-ELISA) for WC detection of *Brucella* at an experimental LOD of 10^3 CFU mL^{-1} with a detection range of 10^2–10^8 CFU mL^{-1} (Hans et al., 2020).

2.1 Chemical reagents

The reagents used in thus study were chloroauric acid trihydrate ($HAuCl_4.3H_2O$, from Sigma-Aldrich, 520918), trisodium citrate dihydrate (Hi-media, GRM 1415), citric acid (Sigma, 251275 BCBZ1757), sodium borohydride (Sigma, 452874), Milli-Q Water (Milli-Q Direct 8, Millipore Unit), bovine serum albumin (BSA from Hi-media RM 105), fetal bovine serum (FBS from Hi-media, RM10409), *Brucella* selective supplements (BSS from Hi-media FD-005, 0000077461), *Brucella* selective broth (BSB from Hi-media, M348), brain–heart infusion broth (BHI from Hi-media, M210), Luria–Bertani broth (LB from Hi-media, M1245), protein-A antibody purification kit (PROSEP-A Montage-Millipore, United States, LSK2ABA20 AK082402), N-(3-dimethylaminopropyl)-N′-ethylcarbodiimide hydrochloride (EDC Sigma Ultra from Sigma-Aldrich, E–1769, 037K07536), N-hydroxysuccinimide (NHS from Sigma-Aldrich, 130672, BCBF1078V), O-phenylenediamine dihydrochloride (OPD from Sigma, 030153, 012-146-008), isopropyl β-D-1-thiogalactopyranoside (IPTG from Sigma, I6758, 056M4040V), iso-propanol (iso-propyl alcohol from Qualigens Fine Chemicals, 26895, NL17386305V), kanamycin sulfate (antibiotic from Sigma, K1377, SLBB0945V), Ni-NTA gel (Superflow from Qiagen, 30430, 154016665), polyclonal goat and rabbit anti-mice immunoglobulins/HRP (P0447, 20083051 and P0260, 20079831 from Dako Denmark), polyclonal goat anti-rabbit immunoglobulins/HRP (P0448, 20083037 from Dako Denmark), sodium azide (Sigma-Aldrich, S2002), urea (Sigma, U5378, 118K0087), methanol (Thermo-Fisher Scientific, 32407, 1,128/3 7109–6), phosphate buffer saline (PBS, pH 7.2, 10 mM L^{-1} from Sigma, P4417, SLBS1525V), hydrochloric acid (0.01 M HCl (Sigma, H1758), and 16-mercaptohexadecanoic acid (99 % MHA from Sigma-Aldrich, 674435).

2.2 Preparation of sol–colloid gold nanoparticles

The AuNPs were synthesized through a chemical reduction method (citrate synthesis) using gold tetrachloride trihydrate ($HAuCl_4.3H_2O$) as a starting material. The citrate synthesis (sol preparation) of AuNPs was performed by using the conventional and reproducible "Turkevich method" with slight modifications as described by Turkevich et al. (1951) and Laaksonen et al. (2006). Different concentrations of the starting material were used and optimized to obtain particles 50 nm in size at a constant volume of solvent (20 mL sterile Milli-Q water) and a

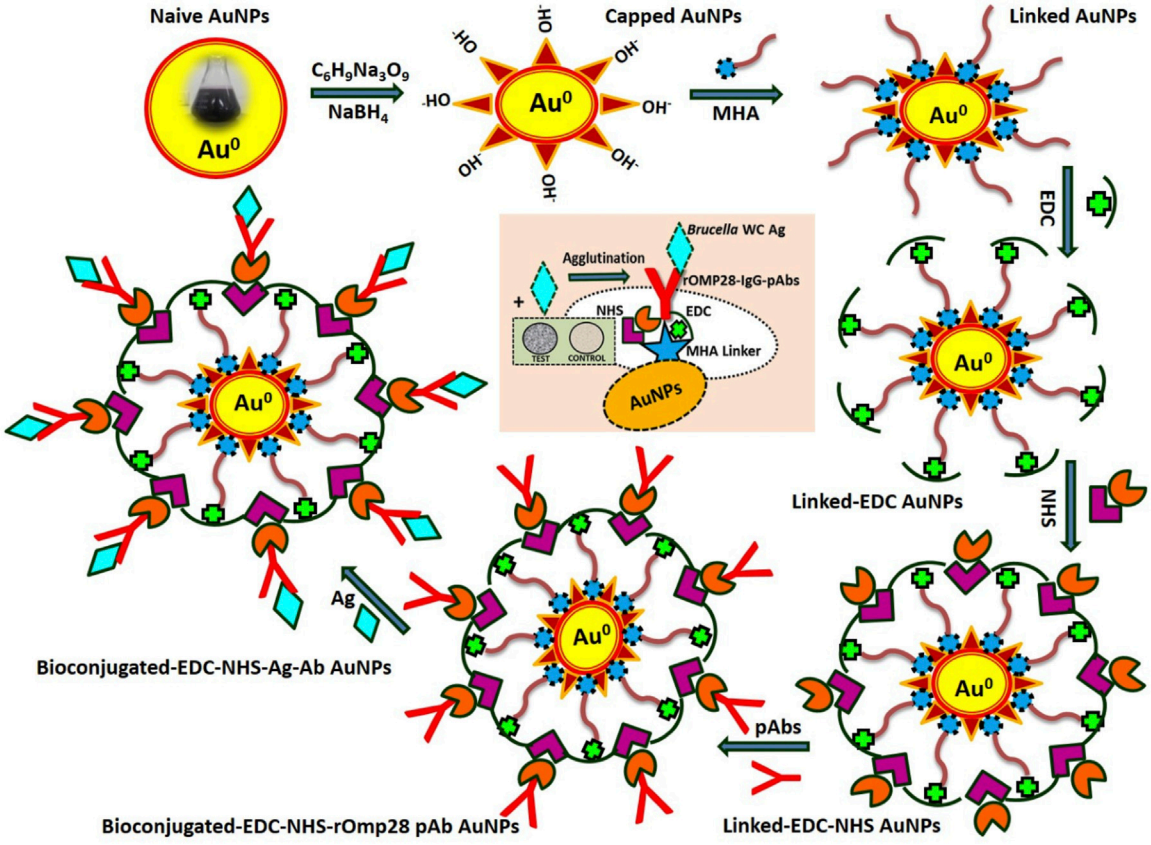

FIGURE 1
A complete scheme representing the methodology applied for development of agglutination assay using modified, functional, and bioconjugated AuNPs.

TABLE 1 Different rational concentrations of gold tetrachloride trihydrate (chloroauric acid, $HAuCl_4.3H_2O$) as a precursor material were used in the preparation of spherical sol–colloid nano-metallic AuNPs. Wine-red colored ruby-red tinted nanosize particles were inferred at an optimized concentration of 0.073 mM (<0.1 mM) with a particle size of 50 nm, prepared using a constant volume of solvent for 10–15 min (particle size analyzed by UV/Vis and TEM analysis).

Sample batch ID	Volume (solvent MQ in mL)	H (mL) $AuCl_4.3H_2O$ (Molarity in mM)	H (mM) $AuCl_4.3H_2O$ (in µL)	$HAuCl_4.3H_2O$ (in mg)	Trisodium citrate dihydrate (v/v)	Heating time (in min.)	Inference (color change)
A	20	0.990	2.71	8.67	2 mL 1% solution	10-15	Violet
B	20	0.990	2.71	8.67	Citric acid buffer A (50 % citrate + 50 % citric acid)	10-15	Yellowish orange
C	20	0.990	2.71	8.67	Citric acid buffer B (75 % citrate + 25 % citric acid)	10-15	Dark violet
D	20	0.990	5.4	15.606	2 mL 1% solution	10-15	Greyish violet
E	20	0.490	1.35	3.901	2 mL 1% solution	10-15	Dark violet
F	20	0.366	1	2.890	2 mL 1% solution	10-15	Crimson red
G	20	0.183	0.5	1.445	2 mL 1% solution	10-15	Dark red
H	20	0.073	0.2	0.578	2 mL 1% solution	10-15	Wine red
I	20	0.036	0.1	0.289	2 mL 1% solution	10-15	Orange red

fixed time of heating (10–15 min), as mentioned in Table 1. Glassware used in the preparation of AuNPs was first treated with aqua regia and washed at least thrice with triple distilled water (DW). After washing, glassware was sterilized with steam autoclaving (121°C for 15 to 20 min at 15 lbs pressure) using a Sanyo Labo Autoclave, MLS-3780, and hot-air dried (at 50°C) using a Labcon, FSIM Standard Incubator. For single-batch preparation of carboxylated AuNPs (thiol-linked AuNPs), 5 µL $HAuCl_4.3H_20$ (0.073 mM) prepared in 10 mL sterile milli-Q water was added to 200 mL ethanol (50 %) solution containing 0.3 mmol MHA at a boiling temperature of 100°C (Ellis et al., 2008; Hashemi et al., 2019). To this boiling solution (light pale-yellow colored), 2 mL freshly prepared 1 % solution of trisodium citrate dihydrate (capping agent) was added, and the obtained solution was allowed to cool to room temperature (Khashayar et al., 2017). The citrate reduction of gold resulted in the formation of AuNPs in sol–colloid form. After cooling, the pH value of the gold sol–colloid was measured [EUTECH pH-meter, Fisher Scientific, INDIKROM Papers (pH 1.0 to 14.0)] and was found to be in the range 6–8 (see Supplementary Figure S1). Thereafter, 20 mL freshly prepared aqueous solution of sodium borohydride (380 mg) was added as a strong reducing agent in order to further reduce the gold (Jurkin et al., 2016; Karimi et al., 2019). The aforementioned solution containing capped carboxylated AuNPs in MHA was continuously stirred (Magnetic Stirrer Spinot, Tarsons) for another 5 h at a constant speed of 200 rpm and was then allowed to precipitate at the bottom of the flask. These precipitated thiol-linked nanoparticles were washed using high speed centrifugation (15,000 to 20,000 rpm for 30 min) and vacuum-dried (Jouan RC 10.22, Thermo Fisher Scientific) for another 7–8 h for further characteristic analysis.

2.3 Characterization of synthesized AuNPs

Functionalized AuNPs were characterized by using UV-visible (UV-2450 Shimadzu), FT-IR (Perkin Elmer, Model Spectrum Two), and Raman spectroscopy (Renishaw Invia Raman Microscope, Gloucestershire, United Kingdom) to determine their optical properties and functional group. Analysis of the NPs' chemical nature, size, structure, surface morphology, and elemental composition was performed with XRD (Rigaku, fifth Generation Mini Flex 600 with Cu-Kα 1 radiation), SEM-EDX (HR FESEM, ULTRA Plus Model with EDX), and TEM (JEOL 1230) along with selected area electron diffraction (SAED). For obtaining the net surface charge, particle size distribution, quantitative binding stoichiometry, and bioconjugation stability of the functionalized AuNPs, apparent ZP (ζ) zeta potential (Nano-ZS, MALVERN Zetasizer Nanoseries, Software Version 7.11) and dynamic light scattering (Nano-ZS Zetasizer, MALVERN) analyses were performed. In parallel, serial UV-vis spectrophotometry (IMPLEN NanoPhotometer, Version 7122 V1.6.1) and fluorescence spectroscopy (PerkinElmer LS-55, Software FL WinLab™) for binding sensitivity and specificity were critically monitored to determine the accuracy of NP modification.

2.4 Bacterial strains and culture growth condition

In this study, nine standard strains of *Brucella* species (Supplementary Table S1), 26 *Brucella* closely related intraspecies (Supplementary Table S2), 36 human *Brucella* clinical isolates from different geographic regions of India (Supplementary Table S3), and a rOmp28-positive clone (*Escherichia coli* BL-21 clone) maintained in 30% glycerol (stored at −80°C) in the laboratory were used (Barua et al., 2016). Bacterial cultures were grown in BSB and BHI growth media with suitable supplements (BSS and 5 % FBS) incubated at 37°C inside a gyrating shaker incubator (Labcon 5081U shaking incubator from Labcon, United States) at a constant shaking speed of 180 rpm. The *Escherichia coli* BL-21 positive clone was grown in LB media supplemented with kanamycin sulfate (50 µg mL^{-1}) antibiotic selection. The handling of pathogenic bacteria and research work associated with this study was performed in a high-containment facility (HCF, DRDE-DRDO Gwalior, India) in the laboratory, following all the standard operating procedures and regulatory methods.

2.5 Cloning, expression, and purification of the recombinant outer membrane protein

A positive clone for the expression of the rOmp28 protein was obtained from the established bacterial molecular cloning-amplified clones, which was done earlier in our laboratory as described (Thavaselvam et al., 2010). The *Omp*28 gene (753bp) of *Brucella melitensis* 16M was PCR amplified, digested, and ligated using the pET-28a expression system. The *Escherichia coli* BL-21 (DE3) expression host was transformed with pET-28a (+) plasmid, and a bacterial culture for the positive recombinant clone was grown with kanamycin (50 µg mL^{-1}) antibiotic selection. The colony-PCR confirmed positive clone was induced with 1 mM IPTG at 5 h for recombinant protein expression. Furthermore, bacterial cells were lysed under denaturing conditions (urea) for rOmp28 protein purification with His-tag binding Ni-NTA gel filtration in Ni-NTA Gel Superflow for affinity column chromatography using different pH buffers [lysis buffer (pH 8.0), wash buffer (pH 6.3), and elution buffer (pH 4.5)]. The purified rOmp28 protein was dialyzed for desalting with subsequent changes in 6 M, 4 M, and 2 M urea buffer followed by sterile 1X PBS (pH 7.2) and was further estimated for protein analysis using the Folin–Lowry method and first dimension SDS PAGE gel electrophoresis (Lowry et al., 1951; Laemmli, 1970).

2.6 Animal immunization for pAb production and IgG purification

For generation of rOmp28 protein antigen (Ag)-derived IgG pAbs, a total of 12 BALB/c female mice were immunized. For animal dosing, 50 µg of Ag per dose per mice was administered at an interval of 1 week over a period of 2 months with six booster doses completed: day 0 (control bled for pre-immune sera, PIS), day 7 (priming with complete Freund's adjuvant, CFA), and day 14 to 49 (boosters with incomplete Freund's adjuvant, IFA) (Zhang et al., 2015). For the estimation of antibody (Ab) titer, whole blood collected from immunized animals was incubated at 37°C for 1 h and centrifuged at 5,000 rpm for 5 to 10 min at 4°C to obtain the hyper-immune sera (HIS) supernatant. Mice IgG pAbs were affinity purified with Montage protein-A columns as per the instructions of the antibody purification kit (Montage-Millipore, United States) and further analyzed using ELISA, SDS-PAGE, and

immunoblotting as per methods previously described (Hans et al., 2020). The antibody titer was estimated using indirect-ELISA whereby, rOmp28 protein Ag at a concentration of 20 μg mL^{-1} was suspended in sodium carbonate–bicarbonate coating buffer (0.05 M, pH 9.6) and immobilized on ELISA immuno-modules (Thermo-Nunc F8 Loose Maxisorp Immunomodules, 469949, 127747) for overnight (O/N) incubation at 4°C. Modules were washed with PBS/PBS-T thrice and blocked with 2% BSA O/N at 4°C, and ELISA was performed as detailed previously (Hans et al., 2020). The total yield of the purified IgG antibody obtained was 6 mg mL^{-1} and was analyzed by SDS-PAGE. The aliquoted purified antibody was stored at −20°C until further use.

2.7 Bioconjugation with functionalized AuNPs

Functionalized AuNPs were prepared by one-step EDC/NHS coupling with linked AuNPs, and then, they are conjugated to mice IgG pAbs according to the reported method with slight modifications (Zhao et al., 2004; Hashemi et al., 2019). To 5 mL of sterile 1X PBS (pH 7.2, 10 mM L^{-1}) containing 0.25 gm EDC (1.3 mM) and 0.25 gm NHS (2.2 mM) in a 1:1 ratio, 0.1 gm of prepared carboxylated-linked AuNPs and 0.002 gm of purified IgG pAbs were added (Busch et al., 2019). The solution was stirred slowly at 100 rpm for approximately 45 min at room temperature (RT). To this buffer solution, 3% bovine serum albumin fraction-V was added, and the solution containing bioconjugated AuNPs was centrifuged and washed twice in 10 mM PBS. The supernatant with unbound pAbs was removed, and conjugates were resuspended in 10 mM PBS. For small working test batches, 0.1 mL (100 μL from 6 mg mL^{-1} IgG pAb suspended in 10 mM PBS, stored with 0.3 gm of sodium azide as preservative) PBS containing 600 μg pAbs and 30 mg modified carboxylated-linked AuNPs were added to 1.5 mL 10 mM PBS solution containing EDC and NHS. For development of the agglutination assay, an optimized 50:1 ratio for active bioconjugation of AuNPs and IgG pAbs resulted in maximum stability of the conjugated pAbs. Increased concentration of the pAbs can hinder the orientation on the nanoparticle surface and can resist binding of the whole-cell antigens. For analysis of the conjugated pAb stability, FT-IR and optical intensity of conjugation were measured. Also, toxicity evaluation of the conjugated constructs was performed with validation studies using spiked clinical samples without any test analytes, for testing the performance of clinical matrices prior to agglutination. On conjugation, the functionalized bioconjugated material was subjected to characterization using FT-IR analysis.

2.8 Slide agglutination of WC *Brucella* using pAb-conjugated AuNPs

For development of the direct-differential slide agglutination assay, one drop (50 μL) from each of the prepared AuNPs-conjugated IgG pAbs and 10-fold serial dilutions of WC Ags (10^8 to 10^1 CFU mL^{-1} in 1X PBS) of *Brucella* at a 1:1 ratio were applied on the test slide. During positive reaction, visible aggregated clumps of WC particulate Ag and Ab complexes appeared on active immuno-agglutination. Such a direct agglutination was considered a positive test for the applied WC Ag. The detection range of agglutinated WCs in CFU mL^{-1} also indicated the experimental LOD for the developed assay.

2.9 Evaluation of assay sensitivity and specificity using inter- and intraspecies

For sensitivity and specificity of the developed assay, WC Ags at 1×10^5 CFU mL^{-1} of both inter- and intraspecies closely related to *Brucella* were tested, and the obtained results were analyzed. WC Ags of bacterial species for testing were mixed with AuNP-conjugated pAbs separately on test slides in a 1:1 ratio (50 μL each). The appearance of strong positive agglutinations during the test result revealed sensitivity, and the corresponding negative test result indicated specificity of the assay.

2.10 Assay validation for direct-slide agglutination in spiked matrices

For the purpose of assay validation, WC Ag at a concentration of 1×10^5 CFU mL^{-1} for two standard species of *Brucella* (*Brucella melitensis* 16M and *Brucella abortus* S99) was spiked in different clinical and non-clinical sample matrices. Then, 20 mL of unpasteurized raw-midstream cow and human milk, curdled with 5 mL of 10% citric acid prepared in 1X PBS, was diluted at a 1:1 dilution ratio in PBS. Furthermore, it was centrifuged at 6,500 rpm for 5 min, and the supernatant was used as the non-clinical sample matrix. Similarly, FBS and human sera (1:1,000 in PBS) along with morning midstream cow and human urine (1:1 in PBS) were used as clinical sample matrices. The results of the validation study indicated the AuNP-conjugated construct-related toxicity and direct potential efficacy of the developed assay in both clinical- and field-based applications.

2.11 Comparative S-ELISA for determining the test efficacy of rOmp28 IgG pAbs

The Sandwich-ELISA immunoassay was optimized for WC detection of *Brucella* in determining the specific test efficacy of rOmp28 protein-derived mice IgG pAbs, as described earlier by (Hans et al., 2020). The *Brucella* WC-derived rabbit IgG pAb (capture pAb at 10 μg mL^{-1}) and rOmp28-derived mice IgG pAb (detection pAb at 100 μg mL^{-1}), as optimized earlier using checker-board S-ELISA, were used for the developed assay (Hans et al., 2020). The sensitivity, detection range, and LOD of rOmp28-derived mice IgG pAbs for WC detection of *Brucella* using S-ELISA were determined to evaluate its test efficacy and its potential for the developed nanoparticle-based direct-differential slide agglutination assay in a clinical scenario.

2.12 Ethical Approval

This work was carried out at the Defence Research and Development Establishment (DRDE-DRDO), Ministry of Defence, Government of India, and was approved by the Institutional Animal Ethics Committee (No: 37/GO/Rbi/S/99/CPCSEA and IAEC MB-43/

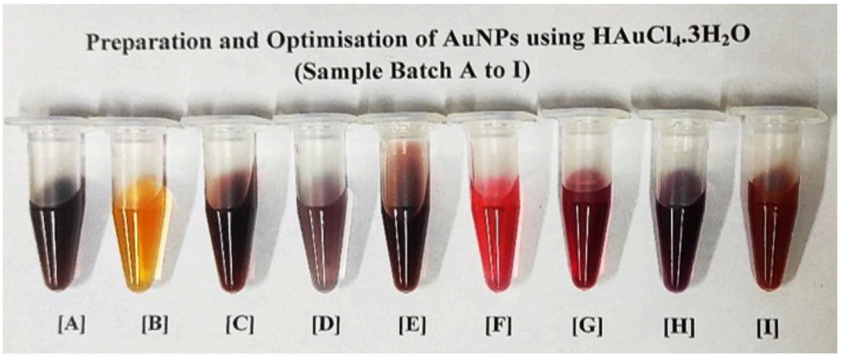

FIGURE 2
Batch-wise **(A–I)** sample preparation and optimisation of AuNPs at defined molar concentrations of gold precursor as shown in Table 1. Different batches of sol-colloids were obtained having **(A)** with violet, **(B)** with yellowish orange, **(C)** with dark violet, **(D)** with greyish violet, **(E)** with dark violet, **(F)** with crimson red, **(G)** with dark red, **(H)** with wine red and **(I)** with orange red colored nanoparticles. The batch sample 'H' with ruby-red wine color was standardized in bio-assay development for direct-rapid WC Ag agglutination of *Brucella* (concentration < 0.1 mM having particle size 50 nm).

57/DTS, dated: 14/06/2018 and IAEC BDTE-01/59/SP, dated: 05/06/2020) for the purpose of control and supervision of experimental animals. All the methods performed in this study were carried out in accordance with proper guidelines and regulations. The study was also approved by the Institutional Biosafety Committee of the Defence Research and Development Establishment (DRDE-DRDO), Ministry of Defence, Government of India vide protocol no. IBSC/15/MB/DTS/6.

3 Results

3.1 UV-visible spectrum analysis and measurement of the prepared AuNPs

Nanometallic AuNPs were prepared using sodium citrate and sodium borohydride as strong co-reducing agents (Haider et al., 2016). On reduction, gold Au^{3+} ions of $HAuCl_4.3H_2O$ were reduced to nano gold Au^0 and this was confirmed by the formation of wine-red sol–colloid with a ruby-colored red-tint at an optimized working concentration of 0.073 mM, which is almost < 0.1 mM of the precursor material (as shown in Figure 2). The particle size of AuNPs was controlled by optimizing the gold-to-citrate ratio as shown in Table 1. The synthesized naive monodispersed colloid particles (before capping) typically had a relative change in the particle size distribution range when analyzed by recording the mean absorbance of the samples. As a result of the analysis, corresponding absorbance spectra displayed a single absorption peak (λ_{max}) in the visible range between 510 and 550 nm (see Figure 3A). With the growth of particles, λ_{max} shifted toward longer wavelengths, and spherical-shaped nanoparticles appeared to have lesser eccentricities. The occurrence of this peak in the absorbance spectra was due to the effect of surface plasmon resonance (SPR). The increase in the SPR peak with the relative particle size of AuNPs was confirmed experimentally at an absorption peak value of 523 nm (see Figure 3A and Supplementary Figure S2A). The total band width of the prepared AuNPs indicated the energy band gap estimated by using the Tauc plot (Eq. 1) in a single particle spectrum, and was found to be 2.68 eV, attributed to the spherical shape of AuNPs (as shown in Figure 3B).

$$(\alpha \cdot h\nu) = A\left(h\nu - \mathrm{E}g\right)^m, \quad (1)$$

where α is the absorption coefficient, h is Plank's constant, ν is the incident photon frequency, A is the optical constant, E*g* is the band gap energy related to the particular transitions of a material, and m is the exponential factor, which depends on the nature of electron transitions and is equal to values 1/2 or 2 for direct or indirect transition band gaps, respectively (Makula et al., 2018).

3.2 Characterization of AuNPs with FT-IR and Raman spectroscopy

FT-IR spectra of modified (naive, capped, and linked) and functionalized AuNPs (bioconjugated-EDC-NHS-Ab AuNPs) were recorded in the wave number range of 4,000 cm^{-1}–450 cm^{-1}, and the results obtained were analyzed for the identification of functional groups (Figure 4A). Initially, for naive nanoparticles collected before reduction, absorption at 3,300–3,400 cm^{-1} corresponds to medium N–H stretching vibrations of hydrogen bonds in amines along with strong and broad bonds of the pendant hydroxyl (–OH) group of alcohols. Another sharp broad peak at 2,500–3,300 cm^{-1} originated from strong O–H stretching of pendant carboxylic acid and weak S–H stretching of thiols (Bartczak and Kanaras, 2011; Dey et al., 2018). Also, the absorption peaks at 1,640 cm^{-1} and 1,403 cm^{-1} of AuNPs are ascribed to strong C=O stretching vibrations of amides, C=C stretching of monosubstituted alkenes, carboxylic group, and relates to the sulfonyl chloride (Shikha et al., 2017). After the addition of reducing agents, capping of AuNPs occurs and medium to strong C–H stretching vibrations of the $-CH_2$ group are assigned to the 2,983 cm^{-1} absorption peak. The shift of peaks at relative position of 2,600–2,550 cm^{-1} is attributed to weak S–H stretching of the thiol group. The strong peak at 1,643 cm^{-1} relates to C=C stretching of monosubstituted alkenes and absorption at 1,250–1,275 cm^{-1} is assigned to C–O stretching of the alkyl aryl group along with corresponding O–H bending in capped AuNPs.

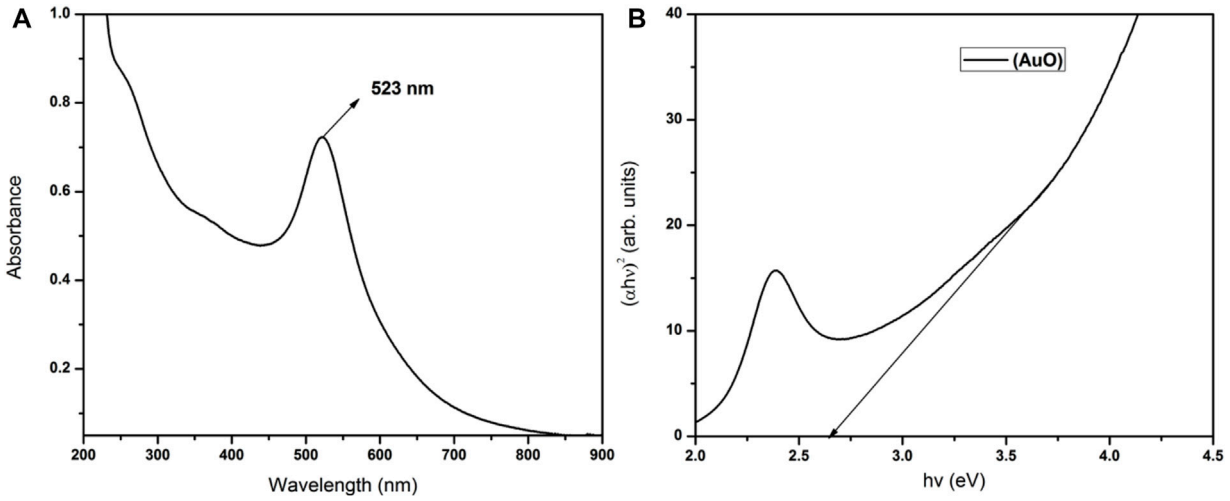

FIGURE 3
UV-visible analysis with **(A)** absorption spectra of AuNPs showing an optical absorption peak at λ_{max} 523 nm and **(B)** total optical absorption band width of reduced nanogold obtained using the Tauc plot showing the corresponding band gap energy at 2.68 eV, attributed to the relative size of AuNPs.

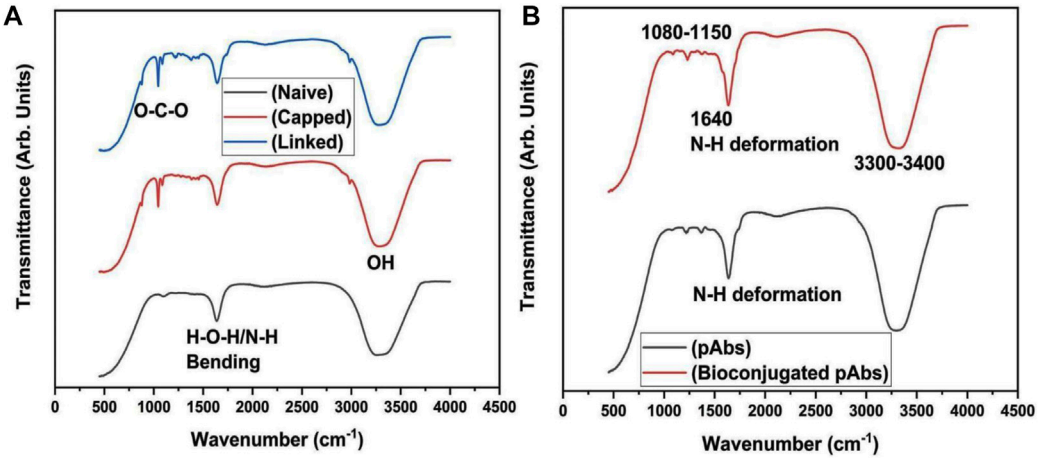

FIGURE 4
Characterization of AuNPs with **(A)** FT-IR analysis indicating N–H (3,300–3,400 cm^{-1}) stretching vibrations of amines, C=O (1,640 and 1,403 cm^{-1}), O–H (2,500–3,300 cm^{-1}), and S–H (2,600–2,550 cm^{-1}) stretching of amide, carboxylic, and thiol groups, C–O (1,250–1,275 cm^{-1}) stretching of alkyl aryl group and –OH bending of alcohols along with C=C (1,643 cm^{-1}), C–H (1,382 and 2,983 cm^{-1}), N–O (1,505 cm^{-1}), and CO–O–CO (1,044–1,085 cm^{-1}) stretching of carboxylic, alkanes and alkyl groups, nitro, alcohols and anhydride groups at different absorption peaks for naive, capped, and linked AuNPs and characterization of naive and bioconjugated pAbs (bioconjugated-EDC-NHS-Ab); **(B)** FT-IR spectrum analysis of naive pAbs with strong N–H (3,300–3,400 cm^{-1}), S–H, and S=O (1,400–1,300 cm^{-1}) stretching vibrations of amide, thiol, sulphonyl, and convoluted O–H groups. For antibody peptide bonds, stretching vibration peaks of C–N and C–O (1,500–1,650 cm^{-1}) along with strong N–H bending of amide groups were analyzed. In bioconjugated functionalized pAb, FT-IR analysis indicated enhanced stretching vibrations of S–H, N–H, and C–H bonds (3,300–3,400 cm^{-1}) for thiol and amide groups along with N–H and C=O (1,640 cm^{-1}), C–N, and N-H (1,230–1,330 cm^{-1}) bending vibrations, and C–O (1,080–1,150 cm^{-1}) strong stretching vibration of amides, amines, carbonyl, aromatic amine with analyzed sharp bending vibrations of N–H deformation for functionalized pAbs.

The relative peaks with corresponding shift in absorption at 1,505 cm^{-1}, 1,382 cm^{-1}, and 1,044 to 1,085 cm^{-1} are attributed to stretching vibrations of N–O of the nitro group, C–H bending of alkanes, and C–O stretching of alcohol along with strong bond CO–O–CO stretching of the anhydride of $NaBH_4$ as the hydride source, respectively (Muddapur et al., 2022). For linked AuNPs, MHA crystallinity on modified NPs can be monitored by a sharp and strong broad bond peak at 3,001 cm^{-1}, indicating N–H and C–H stretching of amine and alkyl groups of EDC and NHS along with the aforementioned peaks (Hinterwirth et al., 2013). Also, AuNPs generally exhibit superlative "surface enhanced Raman scattering (SERS)" properties which were analyzed by Raman spectroscopy (Khatoon et al., 2018). Raman spectra obtained for modified capped and linked AuNPs with corresponding bonds stretching are shown in Figure 5. In the presence of AuNPs, quenching of the fluorescence signal occurred, resulting in spectra with different peaks. Due to the light-scattering process, a change in energy (loss or gain) of the scattered photon at varied wavelengths corresponds to particular bonds in a

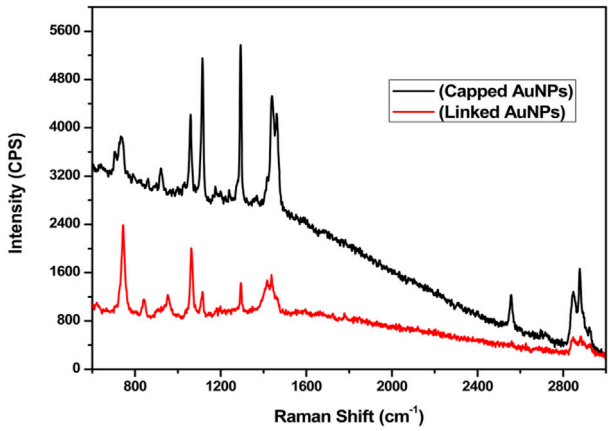

FIGURE 5
Raman spectroscopy (SERS) showing spectra of chemical bond stretching for C–H, S–H, C–H, N=N, C–O–C, C–C, and C–S at corresponding peaks of 2,845, 2,878, 2,556, 1,463, 1,440, 1,292, 1,114, 1,058, 921, 736, and 705 cm^{-1} for capped AuNPs and stretching vibrations of C–H, C=O, N=N, C–C, C–O–C, and C–S at enhanced peaks of 2,843, 1,723, 1,425, 1,294, 1,112.94, 1,063, and 744 cm^{-1} for linked AuNPs, respectively.

molecule. This spectral fingerprint is unique and defines a relative molecular structure of AuNPs based on the characteristic analysis of its physical properties. A 785 nm excitation wavelength laser beam was used. The bands located at 2,845, 2,878, 2,556, 1,463, 1,440, 1,292, 1,114, 1,058, 921, 736, and 705 cm^{-1} were assigned to strong C–H, S–H, asymmetric $–CH_2$ and $–CH_3$, aromatic N=N, asymmetric C–O–C, C–C, and C–S bonds stretching vibrations in capped AuNPs, respectively (Gorbachevskii et al., 2018). The three transient peaks at 1,292, 1,114, and 1,050 cm^{-1} are assigned to stretching vibrations of strong C–S and C–C, along with peaks at 736 and 705 cm^{-1} representing bending vibration of the C–S, indicating overlapping intensity of AuNP samples on active reduction. The enhanced peaks at 1,292 and 1,114 cm^{-1} correspond to aliphatic chain stretching vibrations of C–C and asymmetric C–O–C bonds, respectively. Due to the oxidation of citrate ligands in citrate-capped gold nanoparticles, amplification of SERS occurs, and in citrate-stabilized nanoparticles, citrate can be easily exchanged with –NH and –SH functional ligands (Piella et al., 2017). In the modified linked AuNPs, bands at 2,843, 1,723, 1,425, 1,294, 1,112.94, 1,063, and 744 cm^{-1} are attributed to strong C–H, C=O, N=N bond stretching, C–C bond aliphatic chain vibrations, asymmetric C–O–C, and aliphatic C–S and thiol bonds, as shown in Figure 5 (Madzharova et al., 2020; Aldosari, 2022). The bands located at 1,300 cm^{-1} and in the range 1,060–1,150 cm^{-1} can be associated with aromatic C–C band stretching and C–O–C, C=S stretching, C–H bending vibrations, respectively (Wei et al., 2019).

3.3 Powder X-ray diffraction analysis of AuNPs

On XRD analysis of the dried AuNPs, a pure crystalline structure of nanoscale particles was analyzed. The intense diffraction peaks at 2θ values 38.16°, 44.31°, 64.41°, and 77.50° correspond to the reflections of (111), (200), (220), and (311) set of planes, respectively, of a face-centered cubic (fcc) lattice, as shown in Figure 6 (Biao et al., 2018; Roddu et al., 2020). A peak at 56.32° along with other two peaks at 75° and 83.5° correspond to the orthorhombic phase of Au_2O_3 material [56.32° = (711), 75° = (113), and 83.5° = (333)], calculated from PCPDFWIN ICSD # 710579 (see Figure 6A). This revealed that in addition to Au, a small fraction of Au_2O_3 material is also present in naive gold nanoparticles. The defined sharpness of the peaks directly associates with the crystalline size of AuNPs. For a smaller crystallite size, the peaks are wide and for big crystallites, the peaks are sharper. The crystallite size was calculated by applying the Debye Scherrer formula, as shown in Eq. 2 (Zaman et al., 2019).

$$D = \frac{0.9\lambda}{\beta \cos\theta}, \tag{2}$$

where D is the average crystallite size, λ is the wavelength of the X-ray used, and β is the width at half maximum of the diffraction X-ray peak. This width of the peak and crystallite size had an inverse relation. The larger the crystallite size, the sharper the diffraction peak. In this XRD analysis, the crystallite sizes of naive, capped, and linked AuNPs are 10 nm, 13.5 nm, and 14.5 nm, respectively (as shown in Figures 6A–C). Therefore, the sharpness of the peaks follows the respective order: linked > capped > naive, and θ is Bragg's angle. The lattice parameter was calculated for all the three samples using the following formula for cubic systems:

$$\frac{1}{d_{hkl}} = \frac{h^2 + k^2 + l^2}{a^2}.$$

Also, the lattice parameters for naive, capped, and linked AuNPs samples were calculated to be 4.1 Å, 4.1 Å, and 4.09 Å, respectively, and are very close to the reported values (Busch et al., 2019). In capped AuNPs, aggregation of particles was prevented due to stearic hindrance and electrostatic repulsions introduced by the capping agents, preventing AuNP cementation which also affects the sharpness of peaks. On the contrary, in linked AuNPs, this intensity of sharpness is more intense and clear due to increased intensity and particle size at minimum agglomeration. The results, however, indicated that all the AuNPs were grown in a cubic crystal system of lattice.

3.4 Characterization of AuNPs with SEM and TEM-SAED imaging

SEM-EDX analysis was performed at an applied voltage of 20 keV, and a spectrum of pure gold atoms with spherical-shaped nanoparticles was analyzed (see Supplementary Figure S3). For TEM analysis, copper–carbon mesh grids were coated with a drop of AuNP colloid and mixed together with iso-propanol to reduce the surface tension. These grids loaded with test samples were dried for 20–30 min inside the vacuum chamber and analyzed for the results. The sizes of nanoparticles from TEM micrographs were found to be ~50 nm, ~64 nm, and 110 nm for naive, capped, and linked AuNPs, respectively (as shown in Figures 7A–C). On further analysis of the TEM-SAED pattern for naive AuNPs, bright spots with concentric circular rings for the (111), (200), and (220) set of planes of gold indicated the polycrystalline nature of the gold nanoparticles (Figure 7D). Therefore, at a lesser concentration of the gold precursor (0.073 mM < 0.1 mM) for the synthesis of AuNPs, more

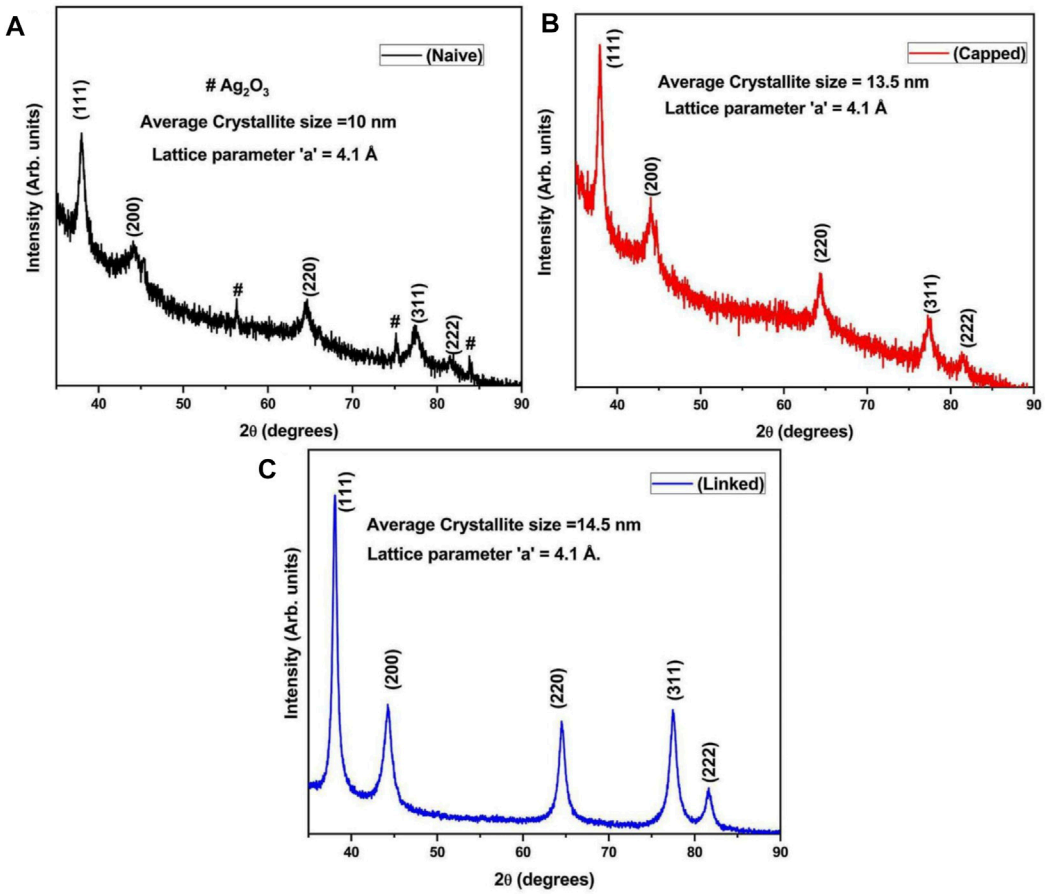

FIGURE 6
Characterization using powder-XRD with **(A–C)** XRD analysis showing angular diffraction peaks at 2θ values of 38.16°, 44.31°, 64.41°, and 77.50° with interplanar spatial reflections of the fcc crystal lattice at the (111), (200), (220), and (311) set of planes for naive, capped, and linked AuNPs. Diffraction peaks at 56.32°, 75°, and 83.5° corresponding to the orthorhombic phase of Au_2O_3 with spatial reflections of the fcc crystal lattice at the (711), (113), and (333) set of planes for naive and capped AuNPs. The parameters of the crystal lattice were obtained at 4.1 Å, 4.1 Å, and 4.09 Å at 10 nm, 13.5 nm, and 14.5 nm, respectively.

uniform, relatively identical, and small-sized spherical particles are obtained for stable bioconjugation (Ngo Thanh et al., 2016). Also, the synthesis and dispersion of nanoparticles in alcohol solution induced less aggregation than water and resulted in AuNPs with pendant carboxylic and alcoholic functional groups for strong bonding with Ab peptides.

3.5 Evaluation of NP surface charge and stable biomolecular binding with ZP (ζ) and DLS

For potential bioassay development, AuNPs were modified (viz., naive, capped, and linked AuNPs), and their step-by-step upgradation was critically monitored by measuring the zeta potential [at temperature 25°C with 12 (ζ) runs] of samples using deionized water (DI) as a dispersant in the zeta dip cell. The two-step citrate reduction of NPs shows a negatively charged surface at neutral pH. Also, on characteristic chemical linking with MHA, an increased negative surface potential was observed (ζ = −10.6 ± 7.25/−12.1 ± 3.42/−23.3 ± 5.01 mV for naive, capped, and linked AuNPs, respectively) due to covalent and site-specific thiol linking (see Supplementary Figure S4A,B; Supplementary Figure S5A,B,C). On functionalization of AuNPs with EDC and NHS, the relative ζ-potential further changed with respect to carboxylated NPs, and their biomolecular covalent binding during bioconjugation with pAbs further resulted in an increase of the net negative surface charge (ζ = −21.2 ± 5.35 and −22.8 ± 5.44 mV for linked-EDC-NHS and bioconjugated-EDC-NHS-Ab, respectively) as shown in Supplementary Figure S4C,D and Supplementary Figure S5D,E,F. On specific Ag-Ab interactions with bioconjugated-EDC-NHS-Ab AuNPs, adsorption of negatively charged rOmp28 protein Ag (depending on orientation of binding) on bioconjugated-EDC-NHS-Ab AuNPs having positively charged protein lysine residues experienced a positive shift in the ζ-potential distribution (ζ = −18.1 ± 4.97 mV from −22.8 ± 5.44 mV for bioconjugated-EDC-NHS-Ag-Ab from bioconjugated-EDC-NHS-Ab, respectively) as shown in Supplementary Figure S4C,D. The observed relative intensity (by phase, voltage, and current) of AuNP surface ζ-potential qualitatively increased with the potential drop of interaction and provided specific and sensitive affinity binding

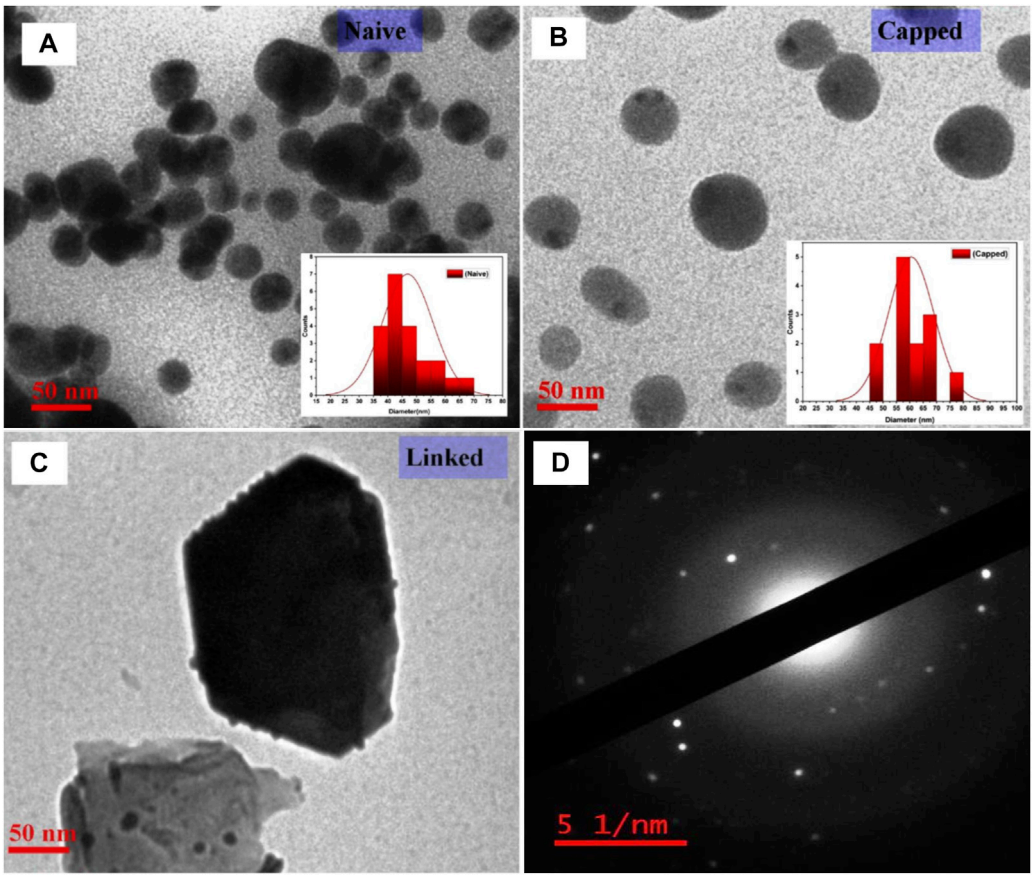

FIGURE 7
Characterization of AuNPs using TEM-SAED with, **(A–C)** TEM micrograph analysis indicating the sizes of the nanoparticles as ~50 nm, ~64 nm, and 110 nm for naive, capped, and linked AuNPs, respectively, with the relative shift in particle size on analysis by UV-vis spectroscopy, and **(D)** TEM-SAED showing patterns with bright spots of concentric circular rings (center to periphery) corresponding to the (111), (200), and (220) lattice planes of polycrystalline gold.

of antigenic sites with characteristic pAbs (see Supplementary Figure S6A–D). The specific orientation of available protein residues during biomolecular binding also increased the surface ζ-potential on NPs (Khashayar et al., 2017; Busch et al., 2019). The increased negative potential of AuNPs explained surface formation of pAb corona face-orientations (compared to less charged carboxylated NPs) for sensitive and stable Ag–Ab bioconjugations below the protein isoelectric point (pH ≤ 9), as shown previously in two different overlay combinations (viz., naive, capped, and linked combination and linked-EDC-NHS, bioconjugated-EDC-NHS-Ab, and bioconjugated-EDC-NHS-Ag-Ab combination). A key aspect for the formation of promising nanostructures is to control and characterize their physico-chemical parameters resulting in stable bioconjugates. Therefore, to determine such biomolecular orientation and nanosize distribution, modified AuNPs were characterized using the DLS analytical tool. Size distribution, both by intensity and volume, were observed with Zetasizer DLS [at a temperature 25°C with 60s–80s durations] using DI water as the dispersant in disposable sizing cuvettes. For every modified NP sample, a total of three DLS measurements with three consecutive test repeats against each measurement were performed, with an initial equilibration of 120 s. Furthermore, 10 μL mL^{-1} of each sample was measured from each batch (before and after bioconjugation of overlay combinations) of AuNPs in DI water against their respective pH of suspended buffer (see Supplementary Figure S1). DLS for mean hydrodynamic diameter and particle size was observed for two different overlay combinations (viz., naive, capped, linked and linked-EDC-NHS, bioconjugated-EDC-NHS-Ab, and bioconjugated-EDC-NHS-Ag-Ab). Also, DLS values obtained were found to be larger due to the presence of a double-layer effect of particle radius in solutions as compared to SEM/TEM analysis, which is obtained for dried powdered states of samples (Supplementary Figure S7) (Khashayar et al., 2017; Fernandez-Ponce et al., 2018). Hence, the resulting particle size distributions by intensity were observed to be 50.51 (d.nm) ± 23.20 (intensity 83.9 %), 106.7 (d.nm) ± 16.95 (94.3 %), and 112.2 (d.nm) ± 15.05 (100 %) for naive, capped, and linked AuNPs, respectively (see Supplementary Figure S7D; Supplementary Figure S8A–C). For the bioconjugated AuNP combination, the particle size distributions by intensity were observed to be 106.7 (d.nm) ± 15.54 (94.5 %), 233.2 (d.nm) ± 16.84 (100 %), and 262.5

(d.nm) ± 15.70 (100 %) for linked EDC-NHS, bioconjugated-EDC-NHS-Ab, and bioconjugated-EDC-NHS-Ag-Ab AuNPs, respectively (see Supplementary Figure S7C; Supplementary Figure S8D–F). Also, to predict the particle size distributions by volume, DLS of naive, capped, and linked AuNPs (before bioconjugation) were observed with Z-average = 428.2 (d.nm), having 100 % distribution by volume and linked AuNPs at a particle size of 108.9 (d.nm) ± 18.52 (d.nm) (see Supplementary Figure S7B).

3.6 Characteristic UV-Vis analysis and fluorescence spectroscopy of modified AuNPs

For the accuracy of bioconjugation and sensitive binding, modified AuNPs were analyzed at very low concentrations of NPs using fluorescence spectroscopy. Parallel to fluorescence, UV-visible analysis for nanoscopic characteristics, measurement of absorption peaks, and curve appearance were also observed. The shift in absorption peak determined the increase in particle size of NPs, and the absence of bands above 650 nm (wavelength range between 200 and 800 nm at a pathlength of 10 mm) wavelength indicated minimal aggregation of AuNPs. Likewise, for modified AuNPs, absorption peaks were observed at 523 nm with decreased absorbance values of 0.649, 0.461, and 0.097 for naive, capped, and linked AuNPs, respectively (see Supplementary Figure S2A–C). Therefore, it suggested that during two-step reduction (citrate-stabilized and borohydride co-reduction), surface hydrogen species were formed, which, on interaction with linking MHA (carboxylic acid-terminated with thiol heads), underwent ligand exchanges and conferred changes in the refractive index and dielectric constant to the AuNP surface (Willey et al., 2004; Pengo et al., 2017; Ansar et al., 2018). Due to electrostatic repulsion from surrounding negative citrate particles, SPR showed an absorption peak at 523 nm. Sodium citrate is an efficient capping agent; on the other hand, sodium borohydride is a strong reducing agent. This co-reduction was done purposefully to control the particle growth for bio-functionalization of AuNPs, since smaller nanoparticles are difficult to modify and often lead to bioconjugate toxicity. Therefore, to obtain biocompatible functionalized AuNPs with less reactivity toward clinical matrices (such as blood, serum, plasma, lymph, and body fluids), dual reduction of AuNPs was performed for stable agglutinations. Co-reduction in an aqueous solution favored a fast nucleation process and homogenous particle size growth and ripening (Piella et al., 2016; Fernandez-Ponce et al., 2018). The hydrodynamic diameters and particle size distributions for naive, capped, and linked AuNPs were measured by TEM and DLS methods and the results indicated the formation of spherical monodispersed AuNPs. In DLS, a higher proportion of homogenous particle sizes is appreciated with maximum size distribution. Furthermore, the decreased absorption value due to MHA-associated corona formation on the surface of AuNPs showed less electrostatic repulsions (Techane et al., 2011; Li et al., 2019). On the other hand, for bioconjugated AuNPs, absorption peaks were observed at a wavelength shift of 528 nm with corresponding absorbance values of 0.098, 0.306, and 0.291 for linked EDC-NHS, bioconjugated-EDC-NHS-Ab, and bioconjugated-EDC-NHS-Ag-Ab AuNPs, respectively (see Supplementary Figure S2D–F). This shift in the UV-vis absorption maximum of AuNP surface plasmon to a higher wavelength reflected an increase in the particle diameter (Suchomel et al., 2018). The bi-functional EDC-NHS functionalization was attributed to the formation of carboxylated AuNPs and, during bioconjugation with pAbs, resulted in corona face-off orientations on AuNPs with a stable net surface charge (Totaro et al., 2016; Busch et al., 2019). This further corresponds to an apparent increase in the absorption value with a relative drop after the interaction of a specific protein antigen by quenching F(ab)2 fragments of pAbs oriented on AuNPs. Therefore, the fluorescence of modified AuNPs was measured with nanochromators with an excitation range of 200–800 nm (with zero order selectable) and emission at 200–650 nm (a standard photo multiplier is zero order at 800–900 nm, with an optional R928 photo multiplier). The accuracy of the wavelength was ± 1.0 nm with a reproducibility of ± 0.5 nm (filter wavelengths 290, 350, 390, 430, 525 nm; a black shutter with 1% attenuator; and clear beam position) and the signal-to-noise ratio was 500:1 r.m.s (Raman band of water at excitation 350 nm and bandpath 10 nm). The samples were analyzed using a single position water thermostable holder for the quartz cuvettes. The emitted light (perpendicular to excitation) was collected by a spectrometer and calibration was performed by subtracting the spectrum of a blank sample (DI water with no AuNPs) from all the spectra of modified AuNPs (Zuber et al., 2015). In this study, a fluorescence peak at 619 nm was observed for naive, capped, and linked AuNPs, and a subsequent increase in the intensity of the peak at 621 nm was measured for each modified bioconjugated sample of AuNPs (1:15 ratio, 0.2/3 mL of DI water), as shown in Figure 8. It was observed that the intensity of the fluorescence peak increased for 50 nm naive AuNPs and was quantitatively enhanced further with increasing particle size at low concentrations of NPs. Similarly, it also decreases with a decrease in the particle size at high NP concentrations. The shift and high intensity of fluorescence peaks for modified AuNPs (naive, capped, and linked) during bioconjugation represented an increase in biomolecular binding on the AuNP surface (Figure 8).

3.7 Expression and purification of the *Brucella* recombinant rOmp28 protein

For the generation of IgG-pAbs to bioconjugate with AuNPs, the expressed rOmp28 protein was purified utilizing different pH-gradient buffer systems with His-tag binding Ni-NTA gel filtration affinity column chromatography, and a 32-kDa protein was obtained with a total yield of 3 mg mL^{-1} on purification (see Figure 9A). For animal immunization, 50 μg mL^{-1} of dialyzed rOmp28 protein was suspended in 1X PBS and administered in animals for production of rOmp28-derived IgG pAbs.

3.8 Production of pAbs against rOmp28 protein Ag

The antibody titer value ≥ 64,000 was obtained with I-ELISA using rOmp28 Ag as “immobilization Ag” on the ELISA test

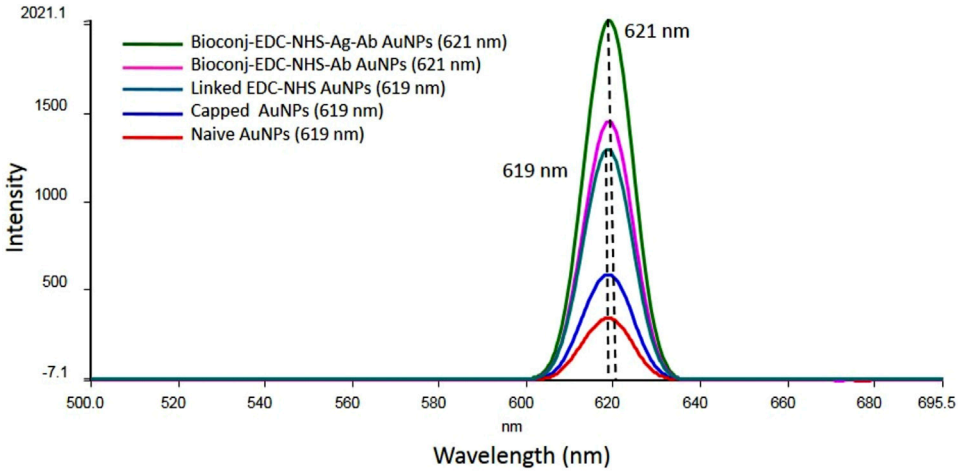

FIGURE 8
Fluorescence spectroscopy analysis of AuNPs showing the characteristic shift and an increase in the intensity of the absorption spectrum related to the surface plasmon resonance of naive, capped, linked, and bioconjugated AuNPs (bioconjugated-EDC-NHS-Ab and bioconjugated-EDC-NHS-Ag-Ab) with the corresponding peak shift from 619 nm to 621 nm. The increase in the intensity of the absorption maximum during step-by-step AuNP modification indicated selective detection of particles with a particular size and shape.

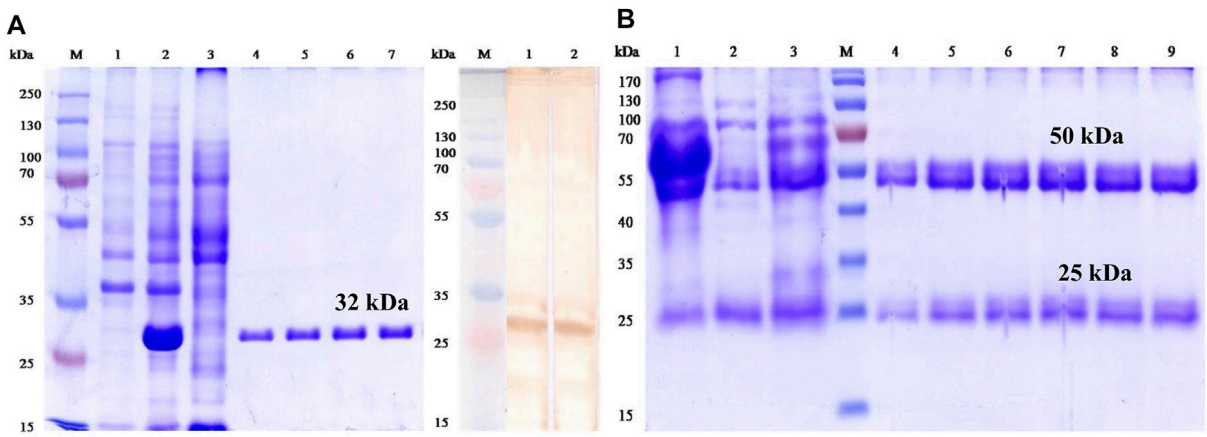

FIGURE 9
First-dimension SDS-PAGE and immunoblot analysis of rOmp28 Ag and IgG-pAbs, respectively, with **(A)** characterization of the expressed and purified rOmp28 protein of *Brucella melitensis* 16M using SDS-PAGE showing the purified recombinant protein of 32 kDa (molecular weight) without any impurity. PAGE analysis with un-induced (*Escherichia coli*, BL-21 clone) lysate (Lane 1), 1 mM IPTG induced (BL-21) clone for 5 h (Lane 2), Ni-NTA agarose column flow through (Lane 3), purified rOmp28 protein elutes 1 to 4 (Lane 4 to 7) in 8M urea at denaturing conditions, Lane M with Fermentas #SM1811 protein marker, and characteristic immunoblot analysis of the specific immuno-reactivity of rOmp28-derived mice IgG pAbs showing positive immunoblot with *Brucella melitensis* 16M rOmp28-purified protein antigen (Lanes 1 and 2) and Lane M with Fermentas #SM1811 protein marker, respectively. **(B)** SDS PAGE analysis of purified rOmp28 mice IgG pAbs developed against the rOmp28 protein antigen of *Brucella melitensis* 16M showing crude mice polyclonal HIS (Lane 1), column wash and flow through (Lane 2 and 3), purified mice IgG pAbs elutes 1 to 6 (Lane 4 to 9) and Lane M with Fermentas #SM0671 protein marker. On polyclonal IgG antibody purification, heavy (large) and light (small) chain fragments at 50 and 25 kDa molecular size, respectively, were obtained.

plates, as shown in Supplementary Figure S9. The antibody titer is defined as the "highest dilution that represents an absorbance greater than or equal to 2.1 fold of the background absorbance" (blank OD value/negative value) (Zhu et al., 2016). Also, a polyclonal regression co-efficient value (R^2) equal to 0.981 was obtained, with linearity in the data pattern and minimum low bias.

3.9 SDS-PAGE and immunoblot analysis of purified IgG pAbs

SDS-PAGE electrophoresis was run at 12% gel composition, and it revealed two fragments of IgG pAbs. One heavy chain fragment at 50 kDa and another light chain small fragment at 25 kDa were obtained on antibody purification (see Figure 9B). A total of 5 μg

lysed sample of IgG pAbs was applied on the SDS gel for analysis. On immunoblot analysis, a positive blot of 32 kDa protein, was obtained with rOmp28 IgG pAbs at 1:100 working dilution prepared in 1X PBS, as shown in Figure 9A. The immunoblot results revealed strong immuno-reactivity and immuno-affinity of the rOmp28 protein toward its purified IgG pAbs of BALB/c mice.

3.10 FT-IR analysis for "bioconjugated pAbs-AuNPs"

The FT-IR spectrum analysis of naive pAbs and its bioconjugated entity showed initial absorption peaks at 3,300 to 3,400 cm^{-1}, 2,604 cm^{-1}, and 1,400 to 1,300 cm^{-1} due to strong stretching vibrations of N–H, S–H, and S=O of thiol and sulphonyl groups along with convoluted O–H bands, respectively (Figure 4B). The major strong peak from 1,500 to 1,650 cm^{-1} was related to the characteristics of the protein and appeared due to the C–N and C=O stretching vibrations of peptide bonds in combination with strong N–H bending of amide I and II groups, as shown in Figure 4B. The FT-IR spectroscopy revealed a vibrational mode of the amide I region in pAbs at 1,650 cm^{-1} due to the carbonyl group –C=O stretching and amide II at 1,500 or 1,550 cm^{-1} due to N–H in-plane bending vibrations (Barth and Zscherp, 2002), since an antibody is a biological molecule protein and contains protein peptide bonds as amide bonds. The absorption spectra of these amides as amide I, II, and III and their multiband IR spectrum indicate fine components within the amides (Ji et al., 2020). In bioconjugated functionalized AuNPs, a strong peak at 3,300 to 3,400 cm^{-1} represented stretching vibrations of N–H and C–H bonds of the amide group and S–H stretching of the thiol group (Sibai et al., 1996). Compounds with the $–NH_2$ group have two IR bands between 3,400 and 3,300 cm^{-1} regardless of the molecule containing the functional group and also, some regions of the protein contain peaks from side chains or any other prosthetic or chemical group attached to the protein (Haris, 2013). In this case, rOmp28 pAbs are bioconjugated and functionalized with linked-EDC-NHS AuNPs as commonly carboxylated thiol-linked AuNPs. The absorption peaks at 1,640 cm^{-1} and 1,230 to 1,330 cm^{-1} indicated bending vibrations of N–H bonds of amide and C=O, C–N of aromatic amine, along with N–H deformation of antibody-conjugated particles. The peaks at 1,080 to 1,150 cm^{-1} were attributed to strong stretching of C–O bonds.

3.11 Slide agglutination reaction of bioconjugated AuNPs with *Brucella* WC Ag

When bioconjugated AuNPs were allowed to react with the corresponding outer membrane surface antigen of WC *Brucella abortus* S99 and *Brucella melitensis* 16M suspended in PBS at a detection range of 10^8–10^1 CFU mL^{-1}, clear visible clumps were observed at a 1:1 (50 µL each) test ratio, as shown in Figure 10. At a minimum time interval of 5 to 10 min, clumping of conjugated pAb–Ag complexes appeared on the reaction site with a lower detection limit of 10^4 CFU mL^{-1} (Figure 10). 1X PBS was used as a test control and was allowed to react with only AuNP-conjugated pAbs, where no clumping was observed, and direct strong agglutinations of the test sample was considered as "test positive" for the applied assay.

3.12 The sensitivity and specificity assays with inter- and intraspecies

On estimating the direct-differential agglutination assay with WC Ag at a concentration of 1×10^4 CFU mL^{-1} of *Brucella* standard strains and a total of 36 randomly selected human clinical isolates, strong positive agglutinations in the test results were obtained which determined the relative efficacy of the method employed, and the high sensitivity of the developed assay (see Figure 11 and Supplementary Table S1; Supplementary Table S3). Similarly, WC Ag (at an optimized test LOD) of 26 *Brucella* closely related and non-related other bacterial species reacted to agglutinate for about 5 to 10 min and for which strong negative results were obtained (Figure 12 and Supplementary Table S2). Hence, on analysis, it was found that the direct-differential slide agglutination assay is both sensitive and specific in whole-cell detection of the genus *Brucella*.

3.13 Validation of the direct-agglutination assay with spiked studies

For validation and evaluation of the direct slide agglutination assay, differential agglutination with *Brucella* WC Ag spiked clinical and non-clinical samples was performed at an optimized detection limit of 10^4 CFU mL^{-1}. The clinical samples such as cow urine, FBS, human sera, human urine and non-clinical samples such as cow milk and human milk have shown no background interference with Ag–Ab agglutination reactions on using AuNP-conjugated rOmp28 mice IgG pAbs, which explained the relatively low toxicity of conjugated constructs (see Figure 13). In fact, a clear, rapid, and strong positive agglutination reaction appeared when the assay was performed within 5 to 10 min. It was clearly inferred during the agglutination reaction that the clumping of modified nanomaterial functionalized with the IgG antibody and its complexes with spiked *Brucella* WC antigens first appeared in spiked sera samples (within 5 min), followed by milk and urine samples after 5 min. This therefore indicated that the developed rapid slide agglutination assay is quite efficient for on-field application in the screening of *Brucella* infection directly from a patient's blood. Also, this assay successfully detected all the spiked standard strains of *Brucella* used in spiking study at an optimized LOD of 10^4 CFU mL^{-1}. The validation study also suggested that the selection of conserved and specific targets for rapid WC Ag detection has relatively high potential to develop sensitive, specific, and accurate detection assays with minimum cross-reactivity and maximum test performance for the confirmation of positive clinical cases. Also, for futuristic approaches, new prospects can be focused on modification of the test antibody to monospecific monoclonal forms or bioengineered antibody fragments to enhance species level biodetection using the proposed direct-differential agglutination assay.

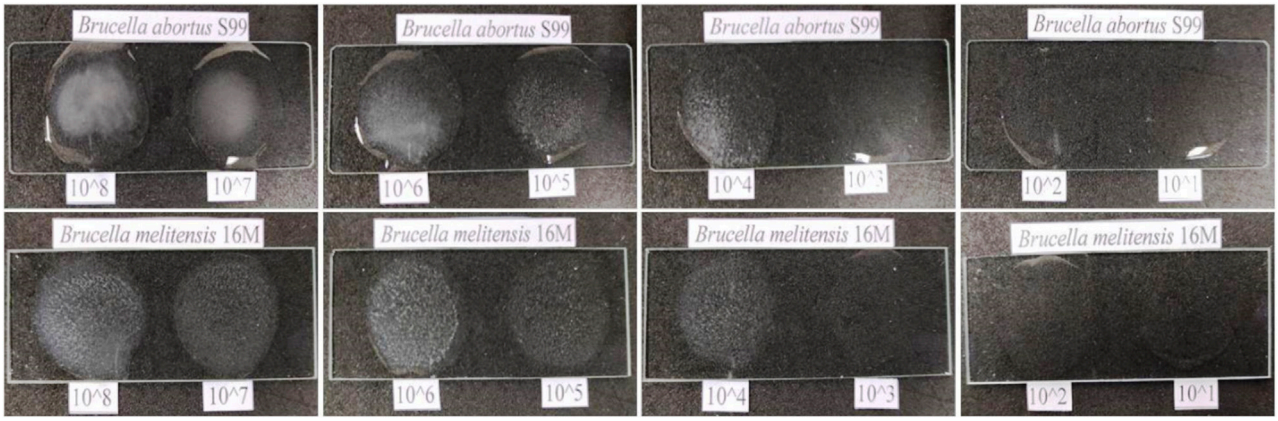

FIGURE 10
Rapid direct-differential slide agglutination assay determining a lower limit of detection (LOD) of 10^4 CFU mL^{-1} at an experimental detection range of 10^8–10^1 CFU mL^{-1} on positive agglutination reaction observed with two standard bacterial species of genus *Brucella* (*Brucella abortus* S99 and *Brucella melitensis* 16M). No hook or prozone effect was observed during positive agglutinations.

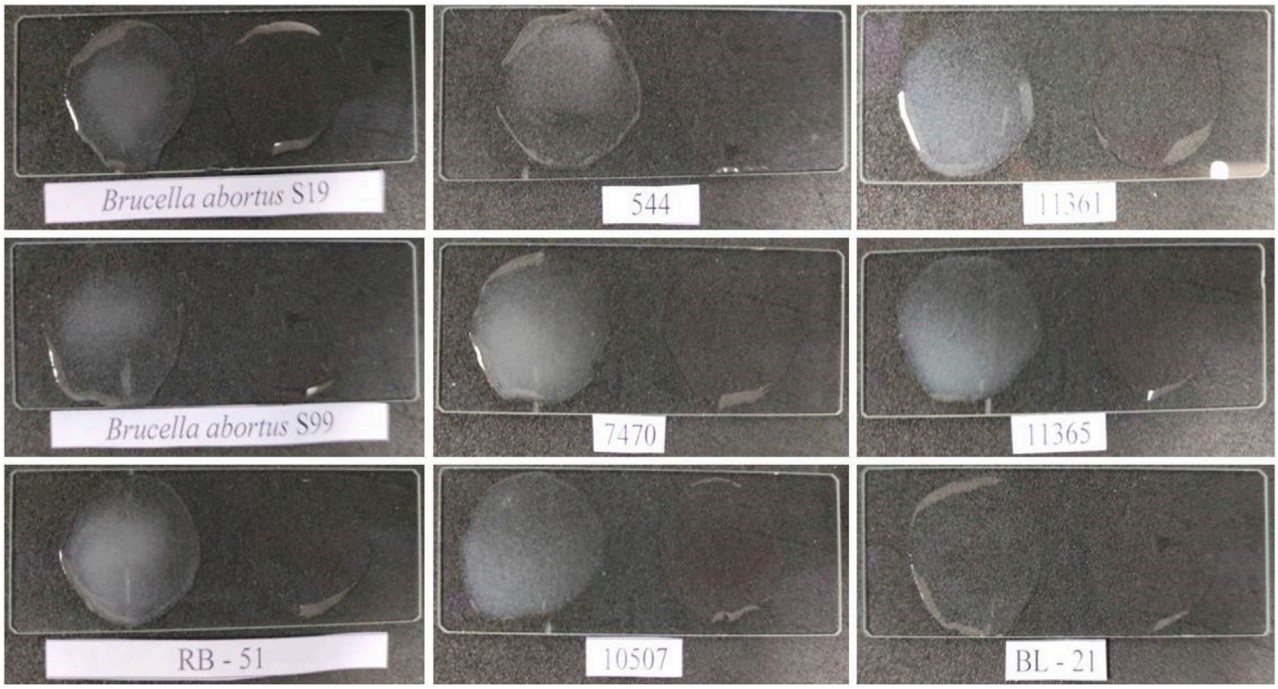

FIGURE 11
Estimation for investigation of test sensitivity of direct-differential slide agglutination assay with WC antigen of *Brucella* standard strains at an obtained experimental LOD of 10^4 CFU mL^{-1} with *Escherichia coli* (BL-21) and 1X PBS having bioconjugated AuNPs without test antigen as a negative test control ("Test Negative"). A rapid and strong agglutination reaction with all *Brucella* standard strains/biotypes was observed, and the results were inferred as "Test Positive" for the developed assay. No agglutination was observed with the test negative *Escherichia coli* and PBS.

3.14 Comparative S-ELISA for *Brucella* whole-cell detection using mice IgG pAbs

To determine the efficacy of the purified rOmp28 mice IgG detection antibody used in the agglutination assay for the evaluation of its rapid immuno-reactivity and minimum detection limits, a comparative S-ELISA for WC Ag detection of standard strains, closely related and non-related bacterial species, and human clinical isolates was performed. The S-ELISA assay detected WC CFU at a minimum LOD of 10^3 CFU mL^{-1} with a detection range of 10^2–10^8 CFU mL^{-1} (Figure 14). *Brucella* standard strains were detected at 10-fold serial dilution with linearity in the trend, a logarithmic regression equation of $y = -0.489 \ln(x) + 1.685$, and $R^2 = 0.846$, as shown in Figure 14A. Also, *Brucella* clinical isolates

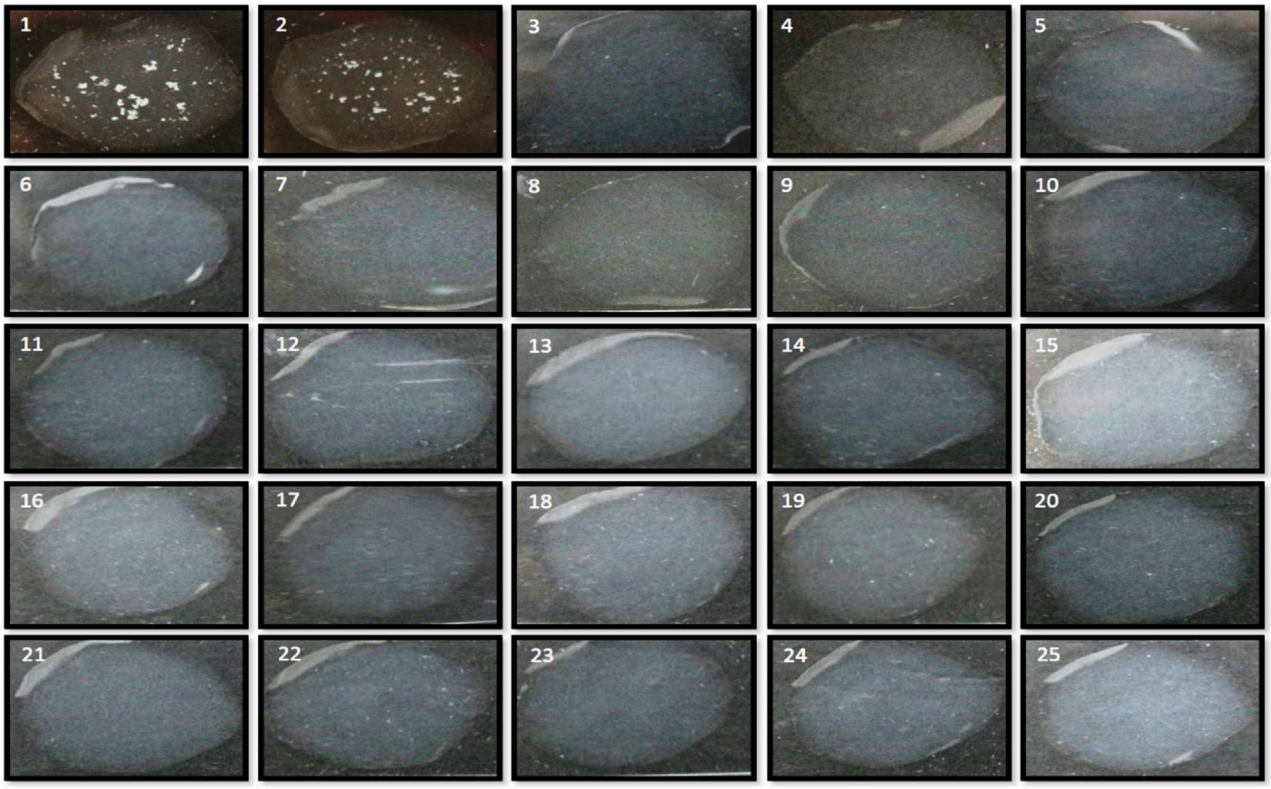

FIGURE 12
Estimation for investigation of test specificity of direct-differential slide agglutination assay with WC antigen of *Brucella* and other closely related and non-related bacterial species to evaluate the cross-reactivity at an obtained experimental LOD of 10^4 CFU mL^{-1}. No clumping for positive agglutination reaction was observed, and the results were inferred as "Test Negative" for the developed assay on testing along with positive test controls (*Brucella abortus* S99 and *Brucella melitensis* 16M) of *Brucella*.

randomly screened at 10-fold serial dilution using the rOmp28 mice IgG detection antibody (at 100 μg mL^{-1}) presented an experimental LOD of 10^3 CFU mL^{-1} (see Figure 14B). The 100% detection of *Brucella* clinical and standard species determined the relative sensitivity and potential efficacy of the optimized test antibody for the developed slide-agglutination assay. In order to determine the comparative specificity of the agglutination assay, cross-reactions with other closely related and non-related bacterial species were evaluated using the rOmp28 mice IgG detection antibody in the double-antibody S-ELISA format, and no intraspecies cross-reactivity was observed at the obtained LOD with similar comparative S-ELISA (see Figure 14C). The minimum LOD was obtained at an experimental cut-off value of 0.3 OD at 495 nm absorbance and was found to have "no detection" as compared to the < 0.5 OD value of positive S-ELISA for WC detection of *Brucella*. In comparison, S-ELISA presented an LOD of 10^3 CFU mL^{-1} with a detection range of 10^2–10^8 CFU mL^{-1} using double-antibody at optimized concentrations (WC rabbit IgG at 10 μg mL^{-1} as the capture antibody and rOmp28 mice IgG at 100 μg mL^{-1} as the detection antibody). We also utilized a labeled anti-species enzyme-conjugated secondary antibody with an experimental run-time of approximately 4 to 5 h. In comparison, although a 1 $\log_{10}$ higher LOD was obtained with the direct-differential slide agglutination assay, it offers minimum time of performance, easy to operate, rapid, cost-effectiveness, sensitive, specific, no hook or prozone effects, higher capacity for multiple sample screening, no false positive or false negative results, and requires minimum expertise or intensive labor. Therefore, recombinant rOmp28 IgG pAbs of *Brucella melitensis* 16M has a high potential for direct-differential WC detection of the genus *Brucella* and can be deployed for early clinical diagnosis.

4 Discussion

Brucella infection is severely contagious with frequent relapse due to its diverse disease pool, intracellular life, antibiotic resistance, and no available vaccines. In our present study, functionalized bioconjugated gold nanoparticles were used in direct-differential whole-cell agglutination of *Brucella* as a rapid, sensitive, and specific detection method for its potential on-field application. We observed a strong positive agglutination reaction due to the rapid Ag–Ab complexes formed with bioconjugated AuNPs, and this method involves a low risk of infection. For *Brucella* rapid detection, many assays have been reported using modified rapid slide agglutination test (RSAT) over conventional RSAT to distinguish rough and smooth strains of *Brucella* (Shell et al., 2012). Microplate agglutination testing (MAT) using multiple recombinant antigen-

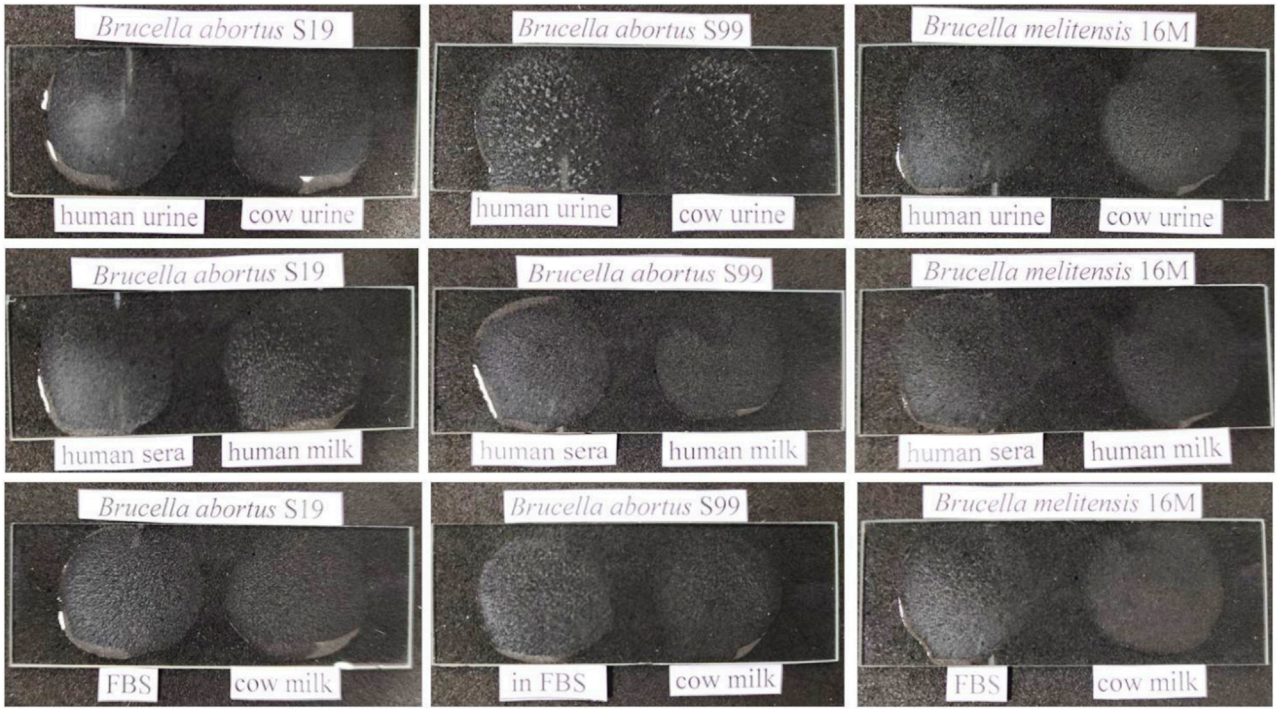

FIGURE 13
Evaluation of experimental validation for rapid and direct-differential slide agglutination assay with spiked WC Ags of *Brucella* standard strains (*Brucella abortus* S19, *Brucella abortus* S99, and *Brucella melitensis* 16M) in different clinical (cow and human urine, FBS-fetal bovine sera, and human sera) and non-clinical (cow and human milk) matrices at an obtained experimental LOD of 10^4 CFU mL^{-1}. A clear, rapid, and strong positive agglutination reaction appeared initially in spiked sera samples, followed by milk and urine samples with no relative interference of test matrices.

coated latex beads for *Brucella canis* identification and tube agglutinin testing (TAT) using antigenic solutions of safranin stained *Brucella canis* were reported (Kimura et al., 2008; Castillo et al., 2014). Latex agglutination testing (LAT) with soluble *Brucella melitensis* periplasmic proteins (SBPPs) for the detection of ovine brucellosis offered better efficacy over the buffered plate agglutination test (BPAT), RBT, SAT, and I-ELISA, but they are less specific with a high rate of false-positives (Ismael et al., 2016). A comparison between the sero-agglutination test (SAT), Coombs anti-*Brucella* test, and brucellaCapt test revealed high sensitivity with brucellaCapt, but it also lacks specificity at lower diagnostic titers (Orduna et al., 2000). Similarly, combined confirmatory tests such as complement fixation test (CFT) and agar gel precipitation test (AGPT) were used together with agglutination assays employing R-LPS antigens, but they also presented prozone effects, high cost, long turn-around time, low sample capacitance, intensive labor, and a high rate of false positives and negatives (Hollett, 2006). On the other hand, our investigation indicated that the employment of rOmp28 as a specific surface marker of *Brucella* is specific, sensitive, and accurate in the detection of whole-cell bacteria with bioconjugated AuNPs. Clinical validation of our study showed direct testing of sample matrices where the availability of *Brucella* is significantly high. Also, AuNPs have a natural tendency to conjugate with active biological moieties and their nanobio interfaces involve amine and thiol group couplings during pAb bioconjugations (Arvizo et al., 2010). We therefore explored specific antigen–antibody-based selective immuno-reaction platforms by conjugating AuNPs for sensitive bacterial detection. Our findings suggest that the drawbacks of serology-based identification can be improved using suitable bioconjugated nanoparticles for early disease detection, diagnosis, and therapeutics (Arruebo et al., 2009). In our study, we modified AuNPs by initial co-reduction for MHA SAM linking, and MHA further favored bi-functional EDC/NHS coupling to preserve the biological activity, stability, and binding affinity of the *Brucella*-specific rOmp28 antibody. The multivalent surface presentations of active functional groups by AuNPs have enhanced covalent linking and ionic adsorptions with the primary amines (N-end) and carboxylic acid ends (C-end) of the antibody for surface immobilization (Fratila et al., 2014; Jazayeri et al., 2016). Hence, conjugation with specific IgG pAbs provided targeted multivalent capture of whole-cell bacteria (Busch et al., 2019). Omp28 is a sensitive diagnostic marker, a non-LPS precursor protein, and a specific immunogen of major OMPs of group-3 immunodominant *Brucella* antigens and has evolved as a selective candidate for improved serological detection of conserved epitopes among *Brucella melitensis* and *Brucella abortus* (Liang et al., 2010; Lim et al., 2012a; Kumar et al., 2012; Ahmed et al., 2015; Manat et al., 2016; Hisham and Ashhab, 2018; He et al., 2022). Its high sensitivity, specificity, and accuracy were discovered in I-ELISA and LAT with the latter showing more rapid detection of anti-*Brucella* antibodies in human and bovine brucellosis and a high degree of suitability in rapid agglutination tests for clinical serodiagnosis (Kumar et al., 2008; Chaudhuri et al., 2010; Lim et al., 2012b; Tiwari et al., 2013; Koyuncu et al., 2018). We therefore selected rOmp28 pAbs in our

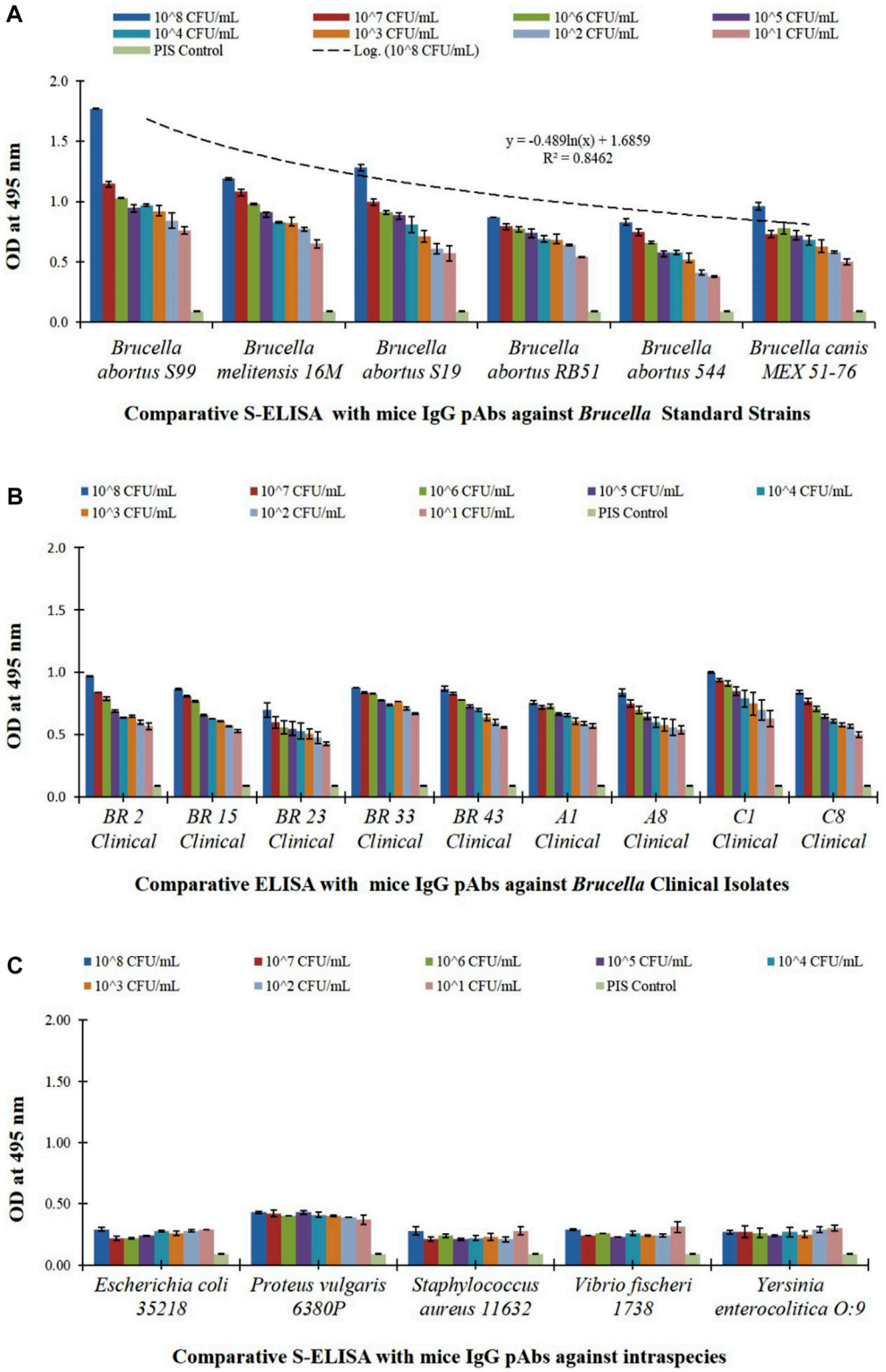

FIGURE 14
Comparative S-ELISA assay for *Brucella* intact WC detection and for evaluation of cross-reactivity with optimized bioconjugated test antibody (rOmp28 mice polyclonal IgG detection antibody) used in the direct-differential slide agglutination assay, with **(A)** S-ELISA graph plot showing WC detection of 10-fold serial diluted WC Ag of *Brucella* standard species at an LOD of 10^3 CFU mL^{-1} with a detection range of 10^2–10^8 CFU mL^{-1} along the x-axis and absorbance at 495 nm along the y-axis. An experimental logarithmic regression coefficient value of R^2 = 0.8462 was obtained with the variable model equation of y = –0.489ln(x) + 1.6859, showing linearity in the trend of *Brucella* WC Ag detection, **(B)** S-ELISA graph plot showing WC detection of 10-fold serial diluted, randomly screened WC Ag of *Brucella* human clinical isolates at an LOD of 10^3 CFU mL^{-1} with a detection range of 10^2–10^8 CFU mL^{-1} along the x-axis and absorbance at 495 nm along the y-axis, and **(C)** S-ELISA graph plot showing WC detection of 10-fold serial diluted
(*Continued*)

FIGURE 14 (Continued)
WC Ag of *Brucella* closely related bacterial intraspecies (*Escherichia coli*, *Proteus vulgaris*, *Staphylococcus aureus*, *Vibrio fischeri*, and *Yersinia enterocolitica*) for evaluation of cross-reactivity at a detection range of 10^2–10^8 CFU mL^{-1} along the x-axis and absorbance at 495 nm along the y-axis. A cut-off OD value of < 0.5 was obtained with no detection as compared to a positive S-ELISA OD value of > 0.5 for *Brucella* standard species and clinical isolates.

detection assay because *bp*26 gene sequencing for the immunogenic BP26 periplasmic protein had revealed identical sequences with minor differences in *Brucella abortus* S19 and *Brucella melitensis* 16M can be abbreviated as for *Brucella* genus like *B. suis* and *B. ovis*, and because it can potentially detect species of *Brucella* (Seco-Mediavilla et al., 2003). We observed that modification of the nanometallic moiety is important in developing a sensitive diagnostic assay. The 16-MHA long chain aliphatic linker (n-alkanethiolate chains) has modified AuNPs for an apparent increase in Ag-to-Ab ratios, increased thiol linkages with rOmp28 pAbs, reduction of non-specific binding, eliminated toxic effects, fabricated stable molecular assemblies, and high passivation of pAbs. IgG antibodies contain an F(ab) region with an amine group and an Fc region with N-glycan residues. A non-specific binding to F(ab) causes inactivation of the antibody by blocking antigen binding sites in variable regions of heavy and light chains (Welch et al., 2017). In this study, 16-MHA acted as the "master molecule" with thiol anchorage allowing fabrication of gold nanoparticles to minimize F(ab) bindings, and, together with EDC/NHS, binds to the Fc region of heavy chains by activating –COOH groups of antibodies to form reactive N-hydroxysuccinimide esters that further bind with amino peptide groups (Bhadra et al., 2015; Drozd et al., 2021). Thus, toxic reactive intermediates of carbodiimide are stabilized by these esterified sulfo-succinimides (NHS). Moreover, in this study, we have evaluated toxic effects with validation studies using clinical samples without the test analyte, and no patching, hooks, or agglomeration of samples was observed. The developed agglutination assay is highly specific and sensitive, and for further species level detection of *Brucella*, we suggest the use of the monospecific monoclonal antibody for bioconjugation. Second, the LOD of 10^4 CFU mL^{-1} for the differential assay can be minimized by using *Brucella*-specific OMPs as combined fusion proteins. Lastly, nanometallic particle integration with the antibody can be replaced with nanoscale metal organic frameworks (MOFs) for further modifications, since the infecting dose of *Brucella* is very low with 10 to 100 CFU mL^{-1} of bacteria required in early on-set of brucellosis infection (Yagupsky, 2022). Therefore, for early disease diagnosis and prevention, more advert nanotechniques with selective markers of *Brucella* are required. In this present study, we selectively used the rOmp28 surface protein marker and found an excellent rate of agglutination in positive test samples, showing no false positives or cross-reactivity with the optimized assay. Therefore, the developed agglutination assay can be used as a preliminary test method in direct whole-cell detection of *Brucella* antigens available in the common disease matrix. Moreover, this assay is rapid, easy to apply, cost-effective, and requires no laboratory set-ups for its clinical application and can be deployed for on-field testing of differential diseased cases where pathogen identification is misleading and under-diagnosed.

5 Conclusion

Brucellosis is the most contagious, debilitative, and widespread common zoonosis, with acute, sub-acute, and chronic disease presentation worldwide, since low doses of 10 to 100 CFU mL^{-1} of bacteria are capable of spreading its infection. In our present study, we therefore developed a concurrent, highly sensitive, differentially rapid, and direct agglutination-based diagnostic assay using 16-MHA SAMs linked functionalized metal oxide gold nanoparticles. This assay offered maximum detection accuracy at an LOD of 1×10^4 CFU mL^{-1} with limited test matrices, and is simple, safe, and reliable with minimum time consumption required for employment in on-field test environments. It is the first assay of its kind with direct differential detection of intact whole-cell *Brucella* achieved at an optimized detection range of 10^1–10^8 CFU mL^{-1}, with diagnostic potential of the recombinant rOmp28 surface protein marker of *Brucella melitensis* 16M. Bioconjugated AuNPs constructs with specific rOmp28 IgG pAbs showed good agreement with in-house available comparative S-ELISA and favorable clinical validation with a related and non-related battery of test pathogens. The sensitivity and specificity of the developed assay is ≥ 98 % which shows the serological potential of the rOmp28 antigen with unique epitopes for limited homology within genus *Brucella*. Moreover, this assay has detected the whole-cell *Brucella* antigen with no similar cross reactions with five closely related bacteria in the S-ELISA format at an LOD of 10^3 CFU ml^{-1}. No toxicity of the functionalized bioconjugated AuNPs was observed as no hemolysis of blood serum was found, and we obtained 100 % true positive agglutinations. The performance time of the assay is minimal, and it requires only 2 to 3 drops of valuable test samples for preliminary diagnostic examination using standard methods. It is therefore sensitive for detecting whole-cell bacteria in low disease burden and a true alternate method for early disease detection. To conclude, we have developed and evaluated the performance of a rapid and direct-differential slide agglutination assay with reduced non-specific reactivity. The comprehensive methodology for the synthesis of biologically stable gold nanoparticles is promising and can be utilized as a potential ready-to-use agglutination-based differential diagnostic method in the low-resource settings of the developing world where brucellosis is highly endemic. Furthermore, this direct agglutination assay can be used for primary characterization of bacterial isolates, and after screening with this agglutination assay, the results can be provided by efficient medical set-ups for management of early clinical cases.

Data availability statement

The original contributions presented in the study are included in the article/Supplementary Material; further inquiries can be directed to the corresponding author.

Ethics statement

The animal study was reviewed and approved by the Institutional Animal Ethics Committee (No: 37/GO/Rbi/S/99/CPCSEA and IAEC MB-43/57/DTS Dated: 14/06/2018 and IAEC BDTE-01/59/SP Dated: 05/06/2020).

Author contributions

DT and RH designed the experiments. RH performed all the experiments and manuscript writing. PY helped in maintaining bacterial cultures. MZ performed SEM, TEM, and TEM-SAED for NP characterization. DT, RP, MZ, and RH performed characteristic analysis of the gold nanomaterial. DT and RH evaluated and analyzed all the experimental results. DT accepted, reviewed, and revised the complete manuscript. This research work was completed by RH under the proper guidance of DT.

Acknowledgments

The authors are thankful to D. K. Dubey, Director, Defence Research and Development Establishment, Defence Research and Development Organisation (DRDO), Jhansi Road, Gwalior—474002 (M.P.), India, for his encouragement and continuous support of this study. Also, the authors extend their acknowledgements to faculty and technical staff of A.P.J. Abdul Kalam Central Instrumentation Facility (C.I.F.), Jiwaji University, Gwalior, Biosensor Development Division and the Electron Microscopy Division, DRDE (DRDO), Gwalior, India, for providing the necessary instrumentation for characterization. This paper has been allotted the DRDE accession no. DRDE/BDTE/50/2020.

Conflict of interest

The authors declare that the research was conducted in the absence of any commercial or financial relationships that could be construed as a potential conflict of interest.

Publisher's note

All claims expressed in this article are solely those of the authors and do not necessarily represent those of their affiliated organizations, or those of the publisher, the editors, and the reviewers. Any product that may be evaluated in this article, or claim that may be made by its manufacturer, is not guaranteed or endorsed by the publisher.

Supplementary material

The Supplementary Material for this article can be found online at: https://www.frontiersin.org/articles/10.3389/fnano.2023.1132783/full#supplementary-material

References

Ahmed, I. M., Khairani-Bejo, S., Hassan, L., Bahaman, A. R., and Omar, A. R. (2015). Serological diagnostic potential of recombinant outer membrane proteins (rOMPs) from Brucella melitensis in mouse model using indirect enzyme-linked immunosorbent assay. *BMC Vet. Res.* 11, 275. doi:10.1186/s12917-015-0587-2

Al Dahouk, S., and Nockler, K. (2011). Implications of laboratory diagnosis on brucellosis therapy. *Expert Rev. anti. Infect. Ther.* 9, 833–845. doi:10.1586/eri.11.55

Aldosari, F. M. M. (2022). Characterization of labeled gold nanoparticles for surface-enhanced Raman scattering. *Molecules* 27, 892. doi:10.3390/molecules27030892

Ansar, S. M., Chakraborty, S., and Kitchens, C. L. (2018). pH-Responsive mercaptoundecanoic acid functionalized gold nanoparticles and applications in catalysis. *Nanomater. (Basel)* 8, 339. doi:10.3390/nano8050339

Arruebo, M., Valladares, M., and Gonzalez-Fernandez, A. (2009). Antibody-conjugated nanoparticles for biomedical applications. *J. Nanomater* 2009, 1–24. doi:10.1155/2009/439389

Arvizo, R., Bhattacharya, R., and Mukherjee, P. (2010). Gold nanoparticles: Opportunities and challenges in nanomedicine. *Expert Opin. Drug Deliv.* 7, 753–763. doi:10.1517/17425241003777010

Bagheri Nejad, R., Krecek, R. C., Khalaf, O. H., Hailat, N., and Arenas-Gamboa, A. M. (2020). Brucellosis in the Middle East: Current situation and a pathway forward. *PLoS Negl. Trop. Dis.* 14, e0008071. doi:10.1371/journal.pntd.0008071

Bakri, F. G., AlQadiri, H. M., and Adwan, M. H. (2018). The highest cited papers in brucellosis: Identification using two databases and review of the papers' major findings. *Biomed. Res. Int.* 1, 1–10. doi:10.1155/2018/9291326

Baltierra-Uribe, S. L., Chanona-Perez, J. J., Mendez-Mendez, J. V., Perea-Flores, M. J., Sanchez-Chavez, A. C., Garcia-Perez, B. E., et al. (2019). Detection of *Brucella abortus* by a platform functionalized with protein A and specific antibodies IgG. *Microsc. Res. Tech.* 82, 586–595. doi:10.1002/jemt.23206

Bartczak, D., and Kanaras, A. G. (2011). Preparation of peptide-functionalized gold nanoparticles using one pot EDC/sulfo-NHS coupling. *Langmuir* 27, 10119–10123. doi:10.1021/la2022177

Barth, A., and Zscherp, C. (2002). What vibrations tell about proteins. *Q. Rev. Biophys.* 35, 369–430. doi:10.1017/s0033583502003815

Barua, A., Kumar, A., Thavaselvam, D., Mangalgi, S., Prakash, A., Tiwari, S., et al. (2016). Isolation & characterization of *Brucella melitensis* isolated from patients suspected for human brucellosis in India. *Indian J. Med. Res.* 143, 652–658. doi:10.4103/0971-5916.187115

Bhadra, P., Shajahan, M. S., Bhattacharya, E., and Chadha, A. (2015). Studies on varying n-alkanethiol chain lengths on a gold coated surface and their effect on antibody-antigen binding efficiency. *RSC Adv.* 5, 80480–80487. doi:10.1039/c5ra11725a

Biao, L., Tan, S., Meng, Q., Gao, J., Zhang, X., Liu, Z., et al. (2018). Green synthesis, characterization and application of proanthocyanidins-functionalized gold nanoparticles. *Nanomaterials* 8, 53. doi:10.3390/nano8010053

Boggiatto, P. M., Schaut, R. G., Kanipe, C., Kelly, S. M., Narasimhan, B., Jones, D. E., et al. (2019). Sustained antigen release polyanhydride-based vaccine platform for immunization against bovine brucellosis. *Heliyon* 5, e02370. doi:10.1016/j.heliyon.2019.e02370

Busch, R. T., Karim, F., Weis, J., Sun, Y., Zhao, C., and Vasquez, E. S. (2019). Optimization and structural stability of gold nanoparticle–antibody bioconjugates. *ACS Omega* 4, 15269–15279. doi:10.1021/acsomega.9b02276

Castillo, Y., Tachibana, M., Kimura, Y., Kim, S., Ichikawa, Y., Endo, Y., et al. (2014). Microplate agglutination test for canine brucellosis using recombinant antigen-coated beads. *Int. Sch. Res. Not.* 2014, 1–4. doi:10.1155/2014/348529

Centers for Disease Control and Prevention (CDC) (2005). Public health consequences of a false-positive laboratory test result for *Brucella* – Florida, Georgia, and Michigan. *MMWR Morb. Mortal. Wkly. Rep.* 57, 603–605.

Chaudhuri, P., Prasad, R., Kumar, V., and Gangaplara, A. (2010). Recombinant OMP28 antigen-based indirect ELISA for serodiagnosis of bovine brucellosis. *Mol. Cell Probes* 24, 142–145. doi:10.1016/jmcp.2009.12.002

Choktaweesak, N., Krasathong, P., and Ammaranond, P. (2016). Development of enhancing agglutination reaction using gold nanoparticle for pre-transfusion testing. *Transfus. Med.* 26, 360–364. doi:10.1111/tme.12330

Dey, A., Yogamoorthy, A., and Sundarapandian, S. M. (2018). Green synthesis of gold nanoparticles and evaluation of its cytotoxic property against colon cancer cell line. *Res. J. Life Sci. Bioinform. Pharm. Chem. Sci.* 4, 1–17. doi:10.26479/2018.0406.01

Di Bonaventura, G., Angeletti, S., Ianni, A., Petitti, T., and Gherardi, G. (2021). Microbiological laboratory diagnosis of human brucellosis: An overview. *Pathogens* 10, 1623. doi:10.3390/pathogens10121623

Drozd, M., Karon, S., and Malinowska, E. (2021). Recent advancements in receptor layer engineering for applications in SPR-based immunodiagnostics. *Sensors* 21, 3781. doi:10.3390/s21113781

El-Sayed, A., and Awad, W. (2018). Brucellosis: Evolution and expected comeback. *Int. J. Vet. Sci. Med.* 6, S31–S35. doi:10.1016/j.ijvsm.2018.01.008

Ellis, A. V., Chong, S., and Jansen, M. (2008). Formation of an α-cyclodextrin/16-mercaptohexadecanoic acid complex and its deposition on gold surfaces. *J. Incl. Phenom. Macrocycl. Chem.* 63, 267–272. doi:10.1007/s10847-008-9516-3

Etemadi, A., Moniri, R., Neubauer, H., Dasteh Goli, Y., and Alamian, S. (2019). Laboratory diagnostic procedures for human brucellosis: An overview of existing approaches. *Jundishapur J. Microbiol.* 12, e91200. doi:10.5812/jjm.91200

Fang, A., Feng, D., Luo, X., and Shi, F. (2022). Gold nanoparticles prepared with cyclodextrin applied to rapid vertical flow technology for the detection of brucellosis. *Biosens. (Basel)* 12, 531. doi:10.3390/bios12070531

Fernandez-Ponce, C., Munoz-Miranda, J. P., de Los Santos, D. M., Aguado, E., Garcia-Cozar, F., and Litran, R. (2018). Influence of size and surface capping on photoluminescence and cytotoxicity of gold nanoparticles. *J. Nanopart. Res.* 20, 305. doi:10.1007/s11051-018-4406-0

Fratila, R. M., Mitchell, S. G., del Pino, P., Grazu, V., and de la Fuente, J. M. (2014). Strategies for the biofunctionalization of gold and iron oxide nanoparticles. *Langmuir* 30, 15057–15071. doi:10.1021/la5015658

Galinska, E. M., and Zagorski, J. (2013). Brucellosis in humans-etiology, diagnostics, clinical forms. *Ann. Agric. Environ. Med.* 20, 233–238.

Gao, Y., Zhou, Y., and Chandrawati, R. (2020). Metal and metal oxide nanoparticles to enhance the performance of enzyme-linked immunosorbent assay (ELISA). *ACS Appl. Nano Mat.* 3, 1–21. doi:10.1021/acsanm.9b02003

Ghazy, N. A., Abdel Aziz, W. R., Shell, W. S., and Samy, A. A. (2016). Efficiency of different preparations of rapid slide agglutination antigens for the diagnosis of bovine and ovine brucellosis. *Asian J. Anim. Vet. Adv.* 11, 399–404. doi:10.3923/ajava.2016.399.404

Gorbachevskii, M. V., Kopitsyn, D. S., Kotelev, M. S., Ivanov, E. V., Vinokurov, V. A., and Novikov, A. A. (2018). Amplification of surface-enhanced Raman scattering by the oxidation of capping agents on gold nanoparticles. *RSC Adv.* 8, 19051–19057. doi:10.1039/C8RA00417J

Govindasamy, K., Etter, E. M. C., Harris, B. N., Rossouw, J., Abernethy, D. A., and Thompson, P. N. (2021). Knowledge of brucellosis, health-seeking behaviour, and risk factors for *Brucella* infection amongst workers on cattle farms in Gauteng, South Africa. *Pathogens* 10, 1484. doi:10.3390/pathogens10111484

Guan, P., Wu, W., and Huang, D. (2018). Trends of reported human brucellosis cases in mainland China from 2007 to 2017: An exponential smoothing time series analysis. *Environ. Health Prev. Med.* 23, 23. doi:10.1186/s12199-018-0712-5

Haider, A. J., Shabeeb, D. A., and Mohammed, A. T. (2016). Synthesis and stabilization of gold nanoparticles by inverse reduction method using sodium citrate and sodium borohydride as reducing agent. *J. Univ. Anbar Pure Sci.* 10, 37–47. doi:10.37652/juaps.2016.132440

Hans, R., Yadav, P. K., Sharma, P. K., Boopathi, M., and Thavaselvam, D. (2020). Development and validation of immunoassay for whole cell detection of *Brucella abortus* and *Brucella melitensis*. *Sci. Rep.* 10, 8543. doi:10.1038/s41598-020-65347-9

Haris, P. I. (2013). Probing protein-protein interaction in biomembranes using Fourier transform infrared spectroscopy. *Biochim. Biophys. Acta Biomembr.* 1828, 2265–2271. doi:10.1016/j.bbamem.2013.04.008

Hashemi, H., Varshosaz, J., Fazeli, H., Sharafi, S. M., Mirhendi, H., Chadeganipour, M., et al. (2019). Rapid differential diagnosis of vaginal infections using gold nanoparticles coated with specific antibodies. *Med. Microbiol. Immunol.* 208, 773–780. doi:10.1007/s00430-019-00622-9

He, C. Y., Yang, J. H., Ye, Y. B., Zhao, H. L., Liu, M. Z., Yang, Q. L., et al. (2022). Proteomic and antibody profiles reveal antigenic composition and signatures of bacterial ghost vaccine of brucella abortus A19. *Front. Immunol.* 13, 874871. doi:10.3389/fimmu.2022.874871

Hinterwirth, H., Kappel, S., Waitz, T., Prohaska, T., Lindner, W., and Lammerhofer, M. (2013). Quantifying thiol ligand density of self-assembled monolayers on gold nanoparticles by inductively coupled plasma-mass spectrometry. *ACS Nano* 7, 1129–1136. doi:10.1021/nn306024a

Hisham, Y., and Ashhab, Y. (2018). Identification of cross-protective potential antigens against pathogenic brucella spp. through combining pan-genome analysis with reverse vaccinology. *J. Immunol. Res.* 2018, 1–15. doi:10.1155/2018/1474517

Hollett, R. B. (2006). Canine brucellosis: Outbreaks and compliance. *Theriogenology* 66, 575–587. doi:10.1016/j.theriogenology.2006.04.011

Holt, H. R., Bedi, J. S., Kaur, P., Mangtani, P., Sharma, N. S., Gill, J. P. S., et al. (2021). Epidemiology of brucellosis in cattle and dairy farmers of rural Ludhiana, Punjab. *Plos Negl. Trop. Dis.* 15, e0009102. doi:10.1371/journal.pntd.0009102

Ismael, A. B., Swelum, A. A., Mostafa, S. A., and Alhumiany, A. R. (2016). Latex agglutination using the periplasmic proteins antigen of *Brucella melitensis* is a successful, rapid, and specific serodiagnostic test for ovine brucellosis. *Int. J. Immunopathol. Pharmacol.* 29, 480–487. doi:10.1177/0394632016648709

Jansen, W., Demars, A., Nicaise, C., Godfroid, J., de Bolle, X., Reboul, A., et al. (2020). Shedding of Brucella melitensis happens through milk macrophages in the murine model of infection. *Sci. Rep.* 10, 9421. doi:10.1038/s41598-020-65760-0

Jazayeri, M. H., Amani, H., Pourfatollah, A. A., Pazoki-Toroudi, H., and Sedighimoghaddam, B. (2016). Various methods of gold nanoparticles (GNPs) conjugation to antibodies. *Sens. Biosensing Res.* 9, 17–22. doi:10.1016/j.sbsr.2016.04.002

Ji, Y., Yang, X., Ji, Z., Zhu, L., Ma, N., Chen, D., et al. (2020). DFT-calculated IR spectrum amide I, II and III band contributions of N-Methylacetamide fine components. *ACS Omega* 5, 8572–8578. doi:10.1021/acsomega.9b04421

Jurkin, T., Gulis, M., Drazic, G., and Gotic, M. (2016). Synthesis of gold nanoparticles under highly oxidizing conditions. *Gold Bull.* 49, 21–33. doi:10.1007/s13404-016-0179-3

Karimi, S., Moshaii, A., and Nikkhah, M. (2019). Controlled synthesis of colloidal monodisperse gold nanoparticles in a wide range of sizes: Investigating the effect of reducing agent. *Mat. Res. Express.* 6, 1150f2. doi:10.1088/2053-1591/ab3e13

Khan, A. U., Melzer, F., Hendam, A., Sayour, A. E., Khan, I., Elschner, M. C., et al. (2020). Seroprevalence and molecular identification of *Brucella* spp. in bovines in Pakistan-investigating association with risk factors using machine learning. *Front. Vet. Sci.* 7, 594498. doi:10.3389/fvets.2020.594498

Khan, M. Z., and Zahoor, M. (2018). An overview of brucellosis in cattle and humans, and its serological and molecular diagnosis in control strategies. *Trop. Med. Infect. Dis.* 3, 65. doi:10.3390/tropicalmed3020065

Khashayar, P., Amoabediny, G., Larijani, B., Hosseini, M., and Vanfleteren, J. (2017). Fabrication and verification of conjugated AuNP-antibody nanoprobe for sensitivity improvement in electrochemical biosensors. *Sci. Rep.* 7, 16070. doi:10.1038/s41598-017-12677-w

Khatoon, N., Yasin, H. M., Younus, M., Ahmed, W., Rehman, N. U., Zakaullah, M., et al. (2018). Synthesis and spectroscopic characterization of gold nanoparticles via plasma-liquid interaction technique. *AIP Adv.* 8, 015130. doi:10.1063/1.5004470

Kimura, M., Imaoka, K., Suzuki, M., Kamiyama, T., and Yamada, A. (2008). Evaluation of a microplate agglutination test (MAT) for serological diagnosis of canine brucellosis. *J. Vet. Med. Sci.* 70, 707–709. doi:10.1292/jvms.70.707

Koyuncu, I., Kocyigit, A., Ozer, A., Selek, S., Kirmit, A., and Karsen, H. (2018). Diagnostic potential of Brucella melitensis Rev1 native Omp28 precursor in human brucellosis. *Cent. Eur. J. Immunol.* 43, 81–89. doi:10.5114/ceji.2018.74877

Kumar, A., Tiwari, S., Thavaselvam, D., Sathyaseelan, K., Prakash, A., Barua, A., et al. (2012). Optimization and efficient purification of recombinant Omp28 protein of Brucella melitensis using Triton X-100 and β-mercaptoethanol. *Protein Expr. Purif.* 83, 226–232. doi:10.1016/j.pep.2012.04.002

Kumar, S., Tuteja, U., Kumar, A., and Batra, H. V. (2008). Expression and purification of the 26 kDa periplasmic protein of Brucella abortus: A reagent for the diagnosis of bovine brucellosis. *Biotechnol. Appl. Biochem.* 49, 213–218. doi:10.1042/BA20070111

Laaksonen, T., Ahonen, P., Johans, C., and Kontturi, K. (2006). Stability and electrostatics of mercaptoundecanoic acid-capped gold nanoparticles with varying counterion size. *Chemphyschem* 7, 2143–2149. doi:10.1002/cphc.200600307

Laemmli, U. K. (1970). Cleavage of structural proteins during the assembly of the head of bacteriophage T4. *Nature* 227, 680–685. doi:10.1038/227680a0

Lalsiamthara, J., and Lee, J. H. (2017). Development and trial of vaccines against *Brucella*. *J. Vet. Sci.* 18, 281–290. doi:10.4142/jvs.2017.18.S1.281

Lemos, T. S., Cequinel, J. C., Costa, T. P., Navarro, A. B., Sprada, A., Shibata, F. K., et al. (2018). Outbreak of human brucellosis in Southern Brazil and historical review of data from 2009 to 2018. *PLoS Negl. Trop. Dis.* 12, e0006770. doi:10.1371/journal.pntd.0006770

Li, L., Yin, D., Xu, K., Liu, Y., Song, D., Wang, J., et al. (2017). A sandwich immunoassay for brucellosis diagnosis based on immune magnetic beads and quantum dots. *J. Pharm. Biomed. Anal.* 141, 79–86. doi:10.1016/j.jpba.2017.03.002

Li, R., Gu, X., Liang, X., Hou, S., and Hu, D. (2019). Aggregation of gold nanoparticles caused in two different ways involved in 4-mercaptophenylboronic acid and hydrogen peroxide. *Mater. (Basel)* 12, 1802. doi:10.3390/ma12111802

Liang, L., Leng, D., Burk, C., Nakajima-Sasaki, R., Kayala, M. A., Atluri, V. L., et al. (2010). Large scale immune profiling of infected humans and goats reveals differential

recognition of Brucella melitensis antigens. *PloS Negl. Trop. Dis.* 4, e673. doi:10.1371/journal.pntd.0000673

Lim, J. J., Kim, D. H., Lee, J. J., Kim, D. G., Min, W., Lee, H. J., et al. (2012). Evaluation of recombinant 28 kDa outer membrane protein of *Brucella abortus* for the clinical diagnosis of bovine brucellosis in Korea. *J. Vet. Med. Sci.* 74, 687–691. doi:10.1292/jvms.11-0512

Lim, J. J., Kim, D. H., Lee, J. J., Kim, D. G., Min, W., Lee, H. J., et al. (2012). Protective effects of recombinant Brucella abortus Omp28 against infection with a virulent strain of Brucella abortus 544 in mice. *J. Vet. Sci.* 13, 287–292. doi:10.4142/jvs.2012.13.3.287

Lin, X., O'Reilly Beringhs, A., and Lu, X. (2021). Applications of nanoparticle-antibody conjugates in immunoassays and tumor imaging. *AAPS J.* 23, 43. doi:10.1208/s12248-021-00561-5

Lowry, O. H., Rosebrough, N. J., Farr, A. L., and Randall, R. J. (1951). Protein measurement with the folin phenol reagent. *J. Biol. Chem.* 193, 265–275. doi:10.1016/S0021-9258(19)52451-6

Lukambagire, A. S., Mendes, A. J., Bodenham, R. F., McGiven, J. A., Mkenda, N. A., Mathew, C., et al. (2021). Performance characteristics and costs of serological tests for brucellosis in a pastoralist community of Northern Tanzania. *Sci. Rep.* 11, 5480. doi:10.1038/s41598-021-82906-w

Madzharova, F., Heiner, Z., and Kneipp, J. (2020). Surface-enhanced hyper Raman spectra of aromatic thiols on gold and silver nanoparticles. *J. Phys. Chem. C Nanomater Interfaces* 124, 6233–6241. doi:10.1021/acs/jpcc.0c00294

Makula, P., Pacia, M., and Macyk, W. (2018). How to correctly determine the band gap energy of modified semiconductor photocatalysts based on UV–vis spectra. *J. Phys. Chem. Lett.* 9, 6814–6817. doi:10.1021/acs.jpclett.8b02892

Malaspina, D. C., Longo, G., and Szleifer, I. (2017). Behavior of ligand binding assays with crowded surfaces: Molecular model of antigen capture by antibody-conjugated nanoparticles. *PLoS One* 12, e0185518. doi:10.1371/journal.pone.0185518

Manat, Y., Shustov, A. V., Evtehova, E., and Eskendirova, S. Z. (2016). Expression, purification and immunochemical characterization of recombinant OMP28 protein of <i>Brucella</i> species. *Open Vet. J.* 6, 71–77. doi:10.4314/ovj.v6i2.1

Memish, Z. A., Almuneef, M., Mah, M. W., Qassem, L. A., and Osoba, A. O. (2002). Comparison of *Brucella* standard agglutination test with the ELISA IgG and IgM in patients with *Brucella* bacteremia. *Diagn. Microbiol. Infect. Dis.* 44, 129–132. doi:10.1016/s0732-8893(02)00426-1

Moreno, E., Blasco, J. M., and Moriyon, I. (2022). Facing the human and animal brucellosis conundrums: The forgotten lessons. *Microorganisms* 10, 942. doi:10.3390/microorganisms10050942

Muddapur, U. M., Alshehri, S., Ghoneim, M. M., Mahnashi, M. H., Alshahrani, M. A., Khan, A. A., et al. (2022). Plant-based synthesis of gold nanoparticles and theranostic applications: A review. *Molecules* 27, 1391. doi:10.3390/molecules27041391

MusallamII, Abo-Shehada, M. N., Hegazy, Y. M., Holt, H. R., and Guitian, F. J. (2016). Systematic review of brucellosis in the Middle East: Disease frequency in ruminants and humans and risk factors for human infection. *Epidemiol. Infect.* 144, 671–685. doi:10.1017/S0950268815002575

Ngo Thanh, V. K., Nguyen, G. D., Huynh, T. P., and Lam, Q. V. (2016). A low cost technique for synthesis of gold nanoparticles using microwave heating and its application in signal amplification for detecting *Escherichia coli* O157:H7 bacteria. *Adv. Nat. Sci. Nanosci. Nanotechnol.* 7, 035016. doi:10.1088/2043-6262/7/3/035016

Okyem, S., Awotunde, O., Ogunlusi, T., Riley, M. B., and Driskell, J. D. (2021). High-affinity points of interaction on antibody allow synthesis of stable and highly functional antibody-gold nanoparticle conjugates. *Bioconjug Chem.* 32, 1753–1762. doi:10.1021/acs.bioconjchem.1c00261

Olsen, S. C., Boggiatto, P., White, D. M., and McNunn, T. (2018). Biosafety concerns related to *Brucella* and its potential use as a bioweapon. *Appl. Biosaf.* 23, 77–90. doi:10.1177/1535676018771983

Olsen, S. C., and Tatum, F. M. (2016). Swine brucellosis: Current perspectives. *Vet. Med.* 8, 1–12. doi:10.2147/VMRR.S91360

Orduna, A., Almaraz, A., Prado, A., Gutierrez, M. P., Garcia-Pascual, A., Duenas, A., et al. (2000). Evaluation of an immunocapture-agglutination test (Brucellacapt) for serodiagnosis of human brucellosis. *J. Clin. Microbiol.* 38, 4000–4005. doi:10.1128/JCM.38.11.4000-4005.2000

Ozdemir, M., Feyzioglu, B., Kurtoglu, M. G., Dogan, M., Dagi, H. T., Yuksekkaya, S., et al. (2011). A comparison of immuncapture agglutination and ELISA methods in serological diagnosis of brucellosis. *Int. J. Med. Sci.* 8, 428–432. doi:10.7150/ijms.8.428

Pal, D., Boby, N., Kumar, S., Kaur, G., Ali, S. A., Reboud, J., et al. (2017). Visual detection of *Brucella* in bovine biological samples using DNA-activated gold nanoparticles. *PLoS ONE* 12, e0180919. doi:10.1371/journal.pone.0180919

Pappas, G., Panagopoulou, P., Christou, L., and Akritidis, N. (2006). Biological weapons. *Cell Mol. Life Sci.* 63, 2229–2236. doi:10.1007/s00018-006-6311-4

Pengo, P., Sologan, M., Pasquato, L., Guida, F., Pacor, S., Tossi, A., et al. (2017). Gold nanoparticles with patterned surface monolayers for nanomedicine: Current perspectives. *Eur. Biophys. J.* 46, 749–771. doi:10.1007/s00249-017-1250-6

Piella, J., Bastus Neus, G., and Puntes, V. (2016). Size-controlled synthesis of sub-10-nanometer citrate-stabilized gold nanoparticles and related optical properties. *Chem. Mater* 28, 1066–1075. doi:10.1021/acs.chemmater.5b04406

Piella, J., Bastus, N. G., and Puntes, V. (2017). Size-dependent protein-nanoparticle interactions in citrate-stabilized gold nanoparticles: The emergence of the protein corona. *Bioconjug Chem.* 28, 88–97. doi:10.1021/acs.bioconjchem.6b00575

Prakash, C., Kumar, B., Singh, R. P., Singh, P., Shrinet, G., Das, A., et al. (2021). Development and evaluation of a gold nanoparticle based lateral flow assay (LFA) strip test for detection of *Brucella* spp. *J. Microbiol. Methods* 184, 106185. doi:10.1016/j.mimet.2021.106185

Pramanik, A., Gao, Y., Patibandla, S., Mitra, D., McCandless, M. G., Fassero, L. A., et al. (2021). The rapid diagnosis and effective inhibition of coronavirus using spike antibody attached gold nanoparticles. *Nanoscale Adv.* 3, 1588–1596. doi:10.1039/d0na01007c

Purwar, S., Metgud, S. C., Mutnal, M. B., Nagamoti, M. B., and Patil, C. S. (2016). Utility of serological tests in the era of molecular testing for diagnosis of human brucellosis in endemic area with limited resources. *J. Clin. Diagn. Res.* 10, DC26–DC29. doi:10.7860/JCDR/2016/15525.7311

Roddu, A. K., Wahab, A. W., Ahmad, A., Taba, P., and Sutapa, I. W. (2020). Theoretical analysis properties of gold nanoparticles resulted by bioreduction process. *J. Phys. Conf. Ser.* 1463, 012008. doi:10.1088/1742-6596/1463/1/012008

Rubach, M. P., Halliday, J. E., Cleaveland, S., and Crump, J. A. (2013). Brucellosis in low-income and middle-income countries. *Curr. Opin. Infect. Dis.* 26, 404–412. doi:10.1097/QCO.0b013e3283638104

Sagi, M., Nesher, L., and Yagupsky, P. (2017). The Bactec FX blood culture system detects *Brucella melitensis* bacteremia in adult patients within the routine 1-week incubation period. *J. Clin. Microbiol.* 55, 942–946. doi:10.1128/JCM.02320-16

Santos, R. L., Souza, T. D., Mol, J. P. S., Eckstein, C., and Paixao, T. A. (2021). Canine brucellosis: An update. *Front. Vet. Sci.* 8, 594291. doi:10.3389/fvets.2021.594291

Saxena, H. M. (2012). *inventor*. Department of Biotechnology Guru Angad Dev Veterinary and Animal Sciences University Ludhiana. (IN), assignee. US patent 20120244552A1. September 27.

Saxena, H. M., and Kaur, P. (2013). A new superagglutination test to minimize false negative and false positive results common with plate/slide agglutination tests for the diagnosis of infectious diseases. *Int. J. Trop. Dis. Health* 3, 199–209. doi:10.9734/IJTDH/2013/3405

Sayer, K. (2016). Brucellosis in fact and fiction: The story of a zoonosis. *Vet. Hist.* 18, 165–183.

Seco-Mediavilla, P., Verger, J. M., Grayon, M., Cloeckaert, A., Marin, C. M., Zygmunt, M. S., et al. (2003). Epitope mapping of the Brucella melitensis BP26 immunogenic protein: Usefulness for diagnosis of sheep brucellosis. *Clin. Diagn Lab. Immunol.* 10, 647–651. doi:10.1128/cdli.10.4.647-651.2003

Shams, A., Rahimian Zarif, B., Salouti, M., Shapouri, R., and Mirzaii, S. (2019). Designing an immunosensor for detection of *Brucella abortus* based on coloured silica nanoparticles. *Artif. Cells. Nanomed Biotechnol.* 47, 2562–2568. doi:10.1080/21691401.2019.1626403

Shell, W. S., Saad, M. A., Abd El-Razik, K. A., Sayed, M. L., and Shaapan, R. M. (2012). *Brucella ovis* as a common antigen for rapid diagnosis of rough brucellosis in cattle and sheep. *Res. J. Microbiol.* 7, 68–74. doi:10.3923/jm.2012.68.74

Shi, J. F., Gong, Q. L., Zhao, B., Ma, B. Y., Chen, Z. Y., Yang, Y., et al. (2021). Seroprevalence of brucellosis in buffalo worldwide and associated risk factors: A systematic review and meta-analysis. *Front. Vet. Sci.* 8, 649252. doi:10.3389/fvets.2021.649252

Shikha, S., Thakur, G. K., and Bhattacharyya, M. S. (2017). Facile fabrication of lipase to amine functionalized gold nanoparticles to enhance stability and activity. *RSC Adv.* 7, 42845–42855. doi:10.1039/C7RA06075K

Sibai, A., Elamri, K., Barbier, D., Jaffrezic-Renault, N., and Souteyrand, E. (1996). Analysis of the polymer-antibody-antigen interaction in a capacitive immunosensor by FTIR difference spectroscopy. *Sens. Actuators B Chem.* 31, 125–130. doi:10.1016/0925-4005(96)80028-1

Song, D., Qu, X., Liu, Y., Li, L., Yin, D., Li, J., et al. (2017). A rapid detection method of *Brucella* with quantum dots and magnetic beads conjugated with different polyclonal antibodies. *Nanoscale Res. Lett.* 12, 179. doi:10.1186/s11671-017-1941-z

Sotnikov, D. V., Barshevskaya, L. V., Zherdev, A. V., Eskendirova, S. Z., Mukanov, K. K., Mukantayev, K. K., et al. (2020). Immunochromatographic system for serodiagnostics of cattle brucellosis using gold nanoparticles and signal amplification with quantum dots. *Appl. Sci.* 10, 738. doi:10.3390/app10030738

Suchomel, P., Kvitek, L., Prucek, R., Panacek, A., Halder, A., Vajda, S., et al. (2018). Simple size-controlled synthesis of Au nanoparticles and their size-dependent catalytic activity. *Sci. Rep.* 8, 4589. doi:10.1038/s41598-018-22976-5

Suo, B., He, J., Wu, C., and Wang, D. (2021). Comparison of different laboratory methods for clinical detection of *Brucella* infection. *Bull. Exp. Biol. Med.* 172, 223–227. doi:10.1007/s10517-021-05367-1

Taheri, H., Amini, B., Kamali, M., Asadi, M., and Naderlou, E. (2020). Functionalization of anti-*Brucella* antibody based on SNP and MNP nanoparticles

for visual and spectrophotometric detection of *Brucella*. *Spectrochim. Acta A Mol. Biomol. Spectrosc.* 229, 117891. doi:10.1016/j.saa.2019.117891

Techane, S., Baer, D. R., and Castner, D. G. (2011). Simulation and modeling of self-assembled monolayers of carboxylic acid thiols on flat and nanoparticle gold surfaces. *Anal. Chem.* 83 (17), 6704–6712. doi:10.1021/ac201175a

Thavaselvam, D., Kumar, A., Tiwari, S., Mishra, M., and Prakash, A. (2010). Cloning and expression of the immunoreactive *Brucella melitensis* 28kDa outer-membrane protein (Omp28) encoding gene and evaluation of the potential of Omp28 for clinical diagnosis of brucellosis. *J. Med. Microbiol.* 59, 421–428. doi:10.1099/jmm.0.017566-0

Tiwari, S., Kumar, A., Thavaselvam, D., Mangalgi, S., Rathod, V., Prakash, A., et al. (2013). Development and comparative evaluation of a plate enzyme-linked immunosorbent assay based on recombinant outer membrane antigens Omp28 and Omp31 for diagnosis of human brucellosis. *Clin. Vaccine Immunol.* 20, 1217–1222. doi:10.1128/CVI.00111-13

Totaro, K. A., Liao, X., Bhattacharya, K., Finneman, J. I., Sperry, J. B., Massa, M. A., et al. (2016). Systematic investigation of EDC/sNHS-mediated bioconjugation reactions for carboxylated peptide substrates. *Bioconjug Chem.* 27, 994–1004. doi:10.1021/acs.bioconjchem.6b00043

Tripathi, K., and Driskell, J. D. (2018). Quantifying bound and active antibodies conjugated to gold nanoparticles: A comprehensive and robust approach to evaluate immobilization chemistry. *ACS Omega* 3, 8253–8259. doi:10.1021/acsomega.8b00591

Turkevich, J., Stevenson, P. C., and Hillier, J. (1951). A study of the nucleation and growth processes in the synthesis of colloidal gold. *Discuss. Faraday Soc.* 11, 55–75. doi:10.1039/DF9511100055

Ukita, M., Hoze, N., Nemoto, T., Cauchemez, S., Asakura, S., Makingi, G., et al. (2021). Quantitative evaluation of the infection dynamics of bovine brucellosis in Tanzania. *Prev. Vet. Med.* 194, 105425. doi:10.1016/j.prevetmed.2021.105425

Watarai, M., Kim, S., Yamamoto, J., Miyahara, K., Kazama, M., Matsuoka, S., et al. (2007). A rapid agglutination assay for canine brucellosis using antigen coated beads. *J. Vet. Med. Sci.* 69, 477–480. doi:10.1292/jvms.69.477

Wei, H., Leng, W., Song, J., Liu, C., Willner, M. R., Huang, Q., et al. (2019). Real-time monitoring of ligand exchange kinetics on gold nanoparticle surfaces enabled by hot spot-normalized surface-enhanced Raman scattering. *Environ. Sci. Technol.* 53, 575–585. doi:10.1021/acs.est.8b03144

Welch, N. G., Scoble, J. A., Muir, B. W., and Pigram, P. J. (2017). Orientation and characterization of immobilized antibodies for improved immunoassays (Review). *Biointerphases* 12, 02D301. doi:10.1116/1.4978435

Willey, T. M., Vance, A. L., van Buuren, T., Bostedt, C., Nelson, A. J., Terminello, L. J., et al. (2004). Chemically transformable configurations of mercaptohexadecanoic acid self-assembled monolayers adsorbed on Au(111). *Langmuir* 20, 2746–2752. doi:10.1021/la036073o

Wu, H., Zuo, Y., Cui, C., Yang, W., Ma, H., and Wang, X. (2013). Rapid quantitative detection of *Brucella melitensis* by a label-free impedance immunosensor based on a gold nanoparticle-modified screen-printed carbon electrode. *Sensors (Basel)* 13, 8551–8563. doi:10.3390/s130708551

Wyatt, H. V. (2013). Lessons from the history of brucellosis. *Rev. Sci. Tech.* 32, 17–25. doi:10.20506/rst.32.1.2181

Xu, N., Wang, W., Chen, F., Li, W., and Wang, G. (2020). ELISA is superior to bacterial culture and agglutination test in the diagnosis of brucellosis in an endemic area in China. *BMC Infect. Dis.* 20, 11. doi:10.1186/s12879-019-4729-1

Yagupsky, P., Morata, P., and Colmenero, J. D. (2019). Laboratory diagnosis of human brucellosis. *Clin. Microbiol. Rev.* 33, 000733–e119. doi:10.1128/CMR.00073-19

Yagupsky, P. (2022). Preventing laboratory-acquired brucellosis in the era of MALDI-TOF technology and molecular tests: A narrative review. *Zoonotic Dis.* 2, 172–182. doi:10.3390/zoonoticdis2040016

Yohannes, M., Gill, J. P. S., Ghatak, S., Singh, D. K., and Tolosa, T. (2012). Comparative evaluation of the rose bengal plate test, standard tube agglutination test and complement fixation test for the diagnosis of human brucellosis. *Rev. Sci. Tech.* 31, 979–984. doi:10.20506/rst.31.3.2175

Zaman, M. B., Mir, R. A., and Poolla, R. (2019). Growth and properties of solvothermally derived highly crystalline Cu2ZnSnS4 nanoparticles for photocatalytic and electrocatalytic applications. *Int. J. Hydrogen Energy* 44, 23023–23033. doi:10.1016/j.ijhydene.2019.07.026

Zhang, Y., Bao, H., Miao, F., Peng, Y., Shen, Y., Gu, W., et al. (2015). Production and application of polyclonal and monoclonal antibodies against Spiroplasma eriocheiris. *Spiroplasma eriocheiris Sci. Rep*. 5, 17871. doi:10.1038/srep17871

Zhao, X., Hilliard, L. R., Mechery, S. J., Wang, Y., Bagwe, R. P., Jin, S., et al. (2004). A rapid bioassay for single bacterial cell quantitation using bioconjugated nanoparticles. *Proc. Natl. Acad. Sci. U. S. A.* 101, 15027–15032. doi:10.1073/pnas.0404806101

Zhu, L., He, J., Cao, X., Huang, K., Luo, Y., and Xu, W. (2016). Development of a double-antibody sandwich ELISA for rapid detection of *Bacillus cereus* in food. *Sci. Rep.* 6, 16092. doi:10.1038/srep16092

Zuber, A., Purdey, M., Schartner, E., Forbes, C., van der Hoek, B., Giles, D., et al. (2015). Detection of gold nanoparticles with different sizes using absorption and fluorescence based method. *Sens. Actuators B Chem.* 227, 117–127. doi:10.1016/j.snb.2015.12.044

Advantages of publishing in Frontiers

OPEN ACCESS
Articles are free to read for greatest visibility and readership

FAST PUBLICATION
Around 90 days from submission to decision

HIGH QUALITY PEER-REVIEW
Rigorous, collaborative, and constructive peer-review

TRANSPARENT PEER-REVIEW
Editors and reviewers acknowledged by name on published articles

Frontiers
Avenue du Tribunal-Fédéral 34
1005 Lausanne | Switzerland

Visit us: www.frontiersin.org
Contact us: frontiersin.org/about/contact

REPRODUCIBILITY OF RESEARCH
Support open data and methods to enhance research reproducibility

DIGITAL PUBLISHING
Articles designed for optimal readership across devices

FOLLOW US
@frontiersin

IMPACT METRICS
Advanced article metrics track visibility across digital media

EXTENSIVE PROMOTION
Marketing and promotion of impactful research

LOOP RESEARCH NETWORK
Our network increases your article's readership